The Dissertation Committee for Yifan Jiang Certifies that this is the approved version of the following dissertation:

Broadly tunable terahertz difference frequency generation in mid-infrared quantum cascade lasers

Committee:

Mikhail A. Belkin, Supervisor

Edward T. Yu

Seth R. Bank

Daniel M. Wasserman

Alexey Belyanin

Broadly tunable terahertz difference frequency generation in mid-infrared quantum cascade lasers

by

Yifan Jiang, B.E.; M.S.E

Dissertation

Presented to the Faculty of the Graduate School of

The University of Texas at Austin

in Partial Fulfillment

of the Requirements

for the Degree of

Doctor of Philosophy

The University of Texas at Austin

May 2017

Dedication

For my parents, my brother and my grandma.

Acknowledgements

I would like to thank my father Tanggen Jiang, mother Shunxiu Xiong, brother Zhiyang Jiang and grandma Renying Xiong, for their continuous support and encouragement during my life.

I am sincerely grateful to my supervisor, Prof. Mikhail Belkin, for his patient guidance, wisdom encouragement, and tremendous support. He opens a door for me to conduct experiment properly, write papers orderly, and present inspirationally. His wealth knowledge and excellent guidance give me endless enthusiasm and motivation during my research, making me a better engineer and researcher.

I would like to thank Prof. Edward Yu, Prof. Seth Bank, Prof. Daniel Wasserman and Prof. Alexey Belyanin for serving as my dissertation committee and providing constructive comments. Their instant help makes this work progress smoothly.

I also appreciate the help from our cooperators, Prof. Markus Amann group at the Technical University of Munich, Prof. Dan Botez at the University of Wisconsin-Madison, and Dr. Kazuue Fujita at Hamamatsu Photonics, for their effort and time in the challenge growth of QCLs.

I'd like to thank my group members, Min Jang, Karun Vijayraghavan, Feng Lu, Aiting Jiang, Seungyong Jung, Mingzhou Jin, Jae Hyun Kim, and Karthik Choutagunta, for their help in the cleanroom and our testing lab. Feng introduced me to the group and gave me lots of guidance in doing testing in the lab, I really appreciate his patient help for my first year in the group. Min also gave me lots of guidance in doing fabrication,

especially thanks for his wisdom help. Karun helped a lot in editing my papers. I am also grateful to my friend in MRC center, Jingsi Li, Xingyu Zhang, Xiaohan Li, Zeyu Pan, Hai Yan, Danlu Wang, who shared their facilities and experience with me.

Thankful to all the MRC facility staff for maintaining the cleanroom in good shape. Many thanks to William Ostler, William James, Ricardo Garcia, Johnny Johnson and Marylene Palard. Also, I would like to express my gratitude to our administrative staff Wood Christine, who is always kind and helpful.

I would also like to thank my friend Qinwu Xu, for his support and encouragement; my roomates Chang Sun, Xue Qian, who make my life colorful.

Finally, I would like to acknowledge my funding support from National Science Foundation, Hamamatsu Photonics and other agencies.

Broadly tunable terahertz difference frequency generation in mid-infrared quantum cascade lasers

Yifan Jiang, Ph.D.

The University of Texas at Austin, 2017

Supervisor: Mikhail A. Belkin

Abstract: Room-temperature terahertz (THz) sources analogous to diode lasers in the near-infrared/visible or quantum cascade lasers (QCL) in the mid-infrared (mid-IR), i.e., electrically pumped, compact, widely tunable, and suitable for low-cost production, are highly desired for feasible and inexpensive THz systems. This dissertation focuses on demonstrating broadly tunable, room-temperature THz systems based on intra-cavity difference frequency generation (DFG) in mid-IR QCLs with improved spectral capability for versatile applications.

Spectral control using an external cavity provides the widest tuning range and is favored for real-world applications. DFG-THz could be spectrally tuned by either tuning one mid-IR pump or by tuning both mid-IR pumps together. I built a Littrow-type, external cavity THz DFG-QCL system that generated spectral tunable THz radiation by fixing one mid-IR pump frequency with an integrated DFB grating on top of the QCL structure and tuning the other mid-IR pump frequency with an external grating, thus demonstrating record broadband narrow linewidth THz frequency tuning from 1.2 to 5.9 THz. A Cherenkov waveguide is used in this system to extract THz radiation through the semi-insulating InP substrate; however, InP has dispersion in 1–6 THz, resulting in steering far

field profiles for different THz frequencies. Replacing the InP substrate with high-resistance silicon through an adhesive bonding process solved the beam steering problem of this THz DFG-QCL system.

I also built a double-Littrow, external cavity DFG-THz system that tunes both mid-IR pump frequencies using two external diffraction gratings. Such a system allows performing a comprehensive spectroscopic study of the optical nonlinearity and its dependence on the mid-infrared pump frequencies. Our work shows that the terahertz generation efficiency can vary by a factor of two or more, depending on the spectral position of the mid-infrared pumps, even for a fixed THz difference frequency. Using this system, we investigated different active region designs: bound-to-continuum, continuum-to-continuum, three-phonon-resonance, and dual-upper-state active region design. Our studies show THz DFG-QCL based a bound-to-continuum active region with gain centered around 15 μm has an order of magnitude enhancement of mid-IR to THz conversion efficiency, which provides a trend for future improvement of the power performance of THz DFG-QCLs.

Table of Contents

List of Figures

Chapter 1: Introduction

1.1 Terahertz spectral range and its application

The terahertz (THz) spectral range from 300 GHz (λ=1 mm) to 10 THz (λ=30 μm), indicated in Figure 1.1, which connects the domains of radio frequency and microwave electronics and mid/near infrared and visible optoelectronics, is an underdeveloped electromagnetic spectral region, despite its proven potential for a variety of applications. This is primarily due to the difficulty of generating and detecting THz frequencies compared with more established electronic and optical technologies. Thus, this spectral region is often known as “THz gap”.

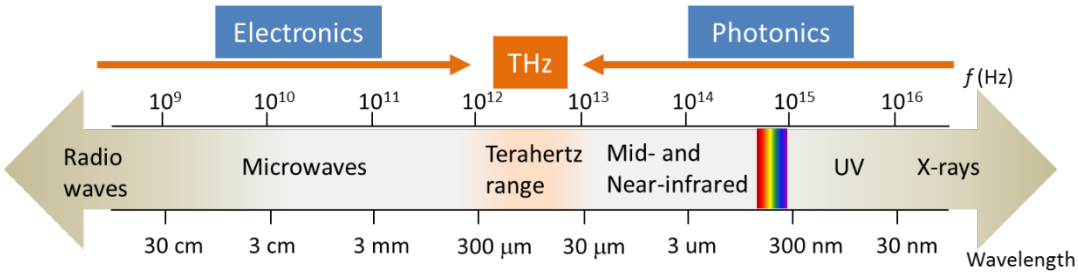

Figure 1.1: THz spectral range

Traditional research in the THz spectral range has largely been limited to the fields of astronomical and other space-based sciences because most photons emitted since the Big Bang and one-half of the total luminosity of the galaxy fall into the terahertz range [1]. With recent advance in photonics and nanotechnology, THz technology is finding use in an increasingly wide variety of applications, including THz spectroscopy, THz imaging, THz heterodyne detection, and even THz communication [2].

In the fields of atmospheric science and environmental monitoring, thermal emission from gasses in the atmosphere in the THz range provides information on ozone depletion and global warming [3]. Efficient gas spectroscopy is also promising since

absorption lines in the THz range are much stronger than those in the infrared and RF range. THz spectroscopy is also valuable for security applications since every explosive and drug has a distinct signature in its THz spectra [4]. These signatures allow for the identification of many chemicals through their transmission spectra.

Imaging and spectroscopic applications using THz radiation are of interest as well. In particular, due to the small energy separation of THz radiation (only 4 meV for 1 THz), many materials (i.e. plastics, fabrics, paper) that are opaque at visible frequency range are actually transmissive in the THz range. For example, in the fields of biology and medical sciences, non-invasive imaging of teeth and sub-dermal melanoma is of great interest. For applications in homeland security, THz radiation is used to detect concealed weapons during airport screening procedures. In the semiconductor industry, terahertz time-domain spectroscopy is already capable of evaluating various semiconductor wafer properties [5,6], such as mobility, conductivity, carrier density and plasma oscillations; for example, one can visualize the doping level of ion-implanted silicon wafers. Figure 1.2 shows varies examples of THz applications.

In information and communications technology, engineers want to increase the data rate of wireless communication by increasing the carrier frequency of the signal to the terahertz frequency range. Larger bandwidths, according to Shannon theorem, are supposed to allow transmission with data rates exceeding 100 Gbit/s [7], and the THz range is currently a non-allocated frequency range. For short-distance and satellite communication where atmospheric absorption is negligible, THz sources would be very promising [8]. For ground communications, different architectures can be put in place according to the transmission distance requirements. For frequencies above 2 THz,

atmospheric absorption limits signal transmission to local communications. However, THz communication can still be implemented for wireless hotspots in public places.

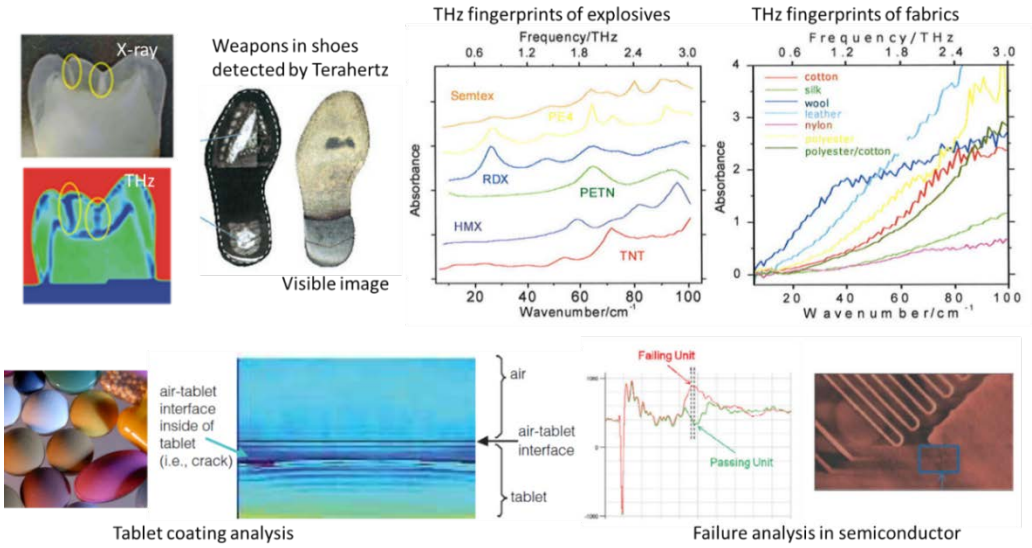

Figure 1.2: THz wave application examples. From dental diagnose, security imaging, explosive and drug detection, tablet coating analysis, to failure analysis in the semiconductor industry (Images from TeraView Ltd.).

1.2 Terahertz sources and their drawbacks

Many types of THz sources have been developed in the past 60 years. Aside from broadband, incoherent thermal blackbody sources for the THz generation, there are primarily two directions to generate coherent THz radiation: one direction is to extend solid-state electronic devices to a higher frequency, and the other is to extend photonic devices to a longer wavelength.

Electronic devices generating THz radiation include the Schottky diode multiplexer, Gunn diode oscillator, and tubes, but their power rolls off with frequency owing to transit-time and resistance-capacitance effects. Low frequency (below 2 THz),

radiation in Schottky diode multiplexer is achieved by nonlinear electronic multiplication of a lower frequency oscillator (30 GHz to 100 GHz) with a chain of Schottky diodes, which produces high order harmonics of the input signal. While these devices could provide continuous-wave operation up to 1.9 THz [9], the output power drops dramatically with increasing frequency due to the carrier velocity constraints and reduced multiplication efficiency.

Photonic devices generating THz radiation include free-electron lasers and gyrotrons, optically-pumped gas lasers, ultrashort pulsed lasers with photoconductive switches or nonlinear crystals, and photomixers using difference frequency generation. Free-electron lasers, gyrotrons, and optically-pumped gas lasers can provide milliwatts average power, but due to their bulky size and complexity, high power consumption, and expensive cost to build, their applications are limited mainly to space and fundamental sciences.

In recent years, THz sources using ultrashort pulsed lasers with photoconductive switches have achieved considerable progress in performance. In this scheme, a femtosecond laser is used to illuminate a photoconductive switch, which induces a sudden electric current across a biased antenna pattern on the switch. This changing current emits THz radiation with the bandwidth determined by the pulse length [10]. Materials of the switch substrate include low-temperature gallium arsenide (LT-GaAs), semi-insulating gallium arsenide (SI-GaAs), or other semiconductor (such as InP) substrates. While the generated THz radiation is broadband in frequency, these sources are widely used for terahertz time-domain spectroscopy nowadays, which is important for imaging applications as discussed previously despite the cost and size of the femtosecond pulsed laser. As an example, current commercial systems based on this scheme are offered from

companies such as TeraView Ltd., Picometrix, Z-omega Optics, and others. THz photomixers using difference frequency generation have achieved over 1mW of continuous-wave (CW) THz output at room temperature [11]. However, these sources are spectrally limited to operate with modest power at frequencies below 2 THz. Such table-top systems are based on externally-pumped nonlinear crystals, which is still not ideal for a compact semiconductor source.

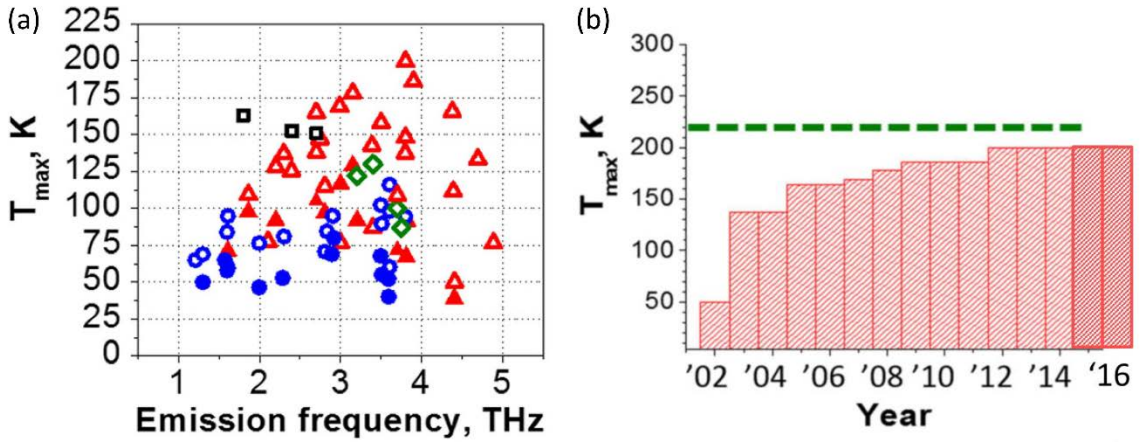

Figure 1.3: Summary of the maximum operating temperatures of THz QCLs reported to date. Solid and open symbols refer to CW and pulsed operation, respectively. Red triangles are resonant-phonon designs, black squares are scattering-assisted injection design, blue circles refer to bound-to-continuum designs, and green diamonds are THz QCLs based on material system other than GaAs/AlGaAs. (b) Timeline for the maximum operating temperatures in pulsed mode achieved by THz QCLs from the initial demonstration in 2002 until end-2016. Green dashed line at 220 K indicates operating temperatures that may be accessible with compact thermoelectric coolers. The data is taken from [30].

An ideal source for a broad range of applications would be a room-temperature semiconductor THz source analogous to a diode laser in the near-infrared and visible ranges. Such a source must be compact, inexpensive, and suitable for a production in large

quantities. More specifically, the source must be coherent, continuous wave, narrow linewidth, broadly tunable, room-temperature operable, and electrically pumped, while delivering at least a milliwatt level of power.

The THz quantum cascade laser (QCL) is one of the leading candidates that could satisfy most of these requirements. Since the demonstration of the first THz QCL emitting at 4.4 THz with a maximum working temperature of 50 K by Alessandro Tredicucci's group in 2002 [13], the spectral coverage and the maximum operating temperature of THz QCLs has improved dramatically. The emission frequency of THz QCLs can now span 1.2 to 5 THz with CW output power of 100 mW [14] and peak power exceeding 1 W [15]. THz QCLs also show promise as broadband THz frequency comb sources [16,18]. Comprehensive reviews of THz QCL design strategies and performance can be found in [17-19].

However, even the best THz QCLs demonstrated so far still operate below 200 K. A summary of the temperature performance of a number of THz QCLs (taken from literature and operating without an external magnetic field) as a function of emission frequency is shown in Figure 1.3(a), and the timeline of the maximum operating temperature achieved by these devices is shown in Figure 1.3(b). This fast deterioration of the performance of THz QCLs with temperature is primarily due to effects of the activated longitudinal optical phonons (LO-phonon). Currently, the best THz QCLs are based on a GaAs-AlGaAs material system, which exhibit LO-phonon energies of about 36 meV, which is very close to the THz band energy separation. The activated LO-phonon makes it hard to establish a population inversion condition at room temperature for THz QCLs. Moreover, it is also very difficult to make THz QCLs broadly tunable; the best tuning range achieved so far is still about several hundred GHz [20].

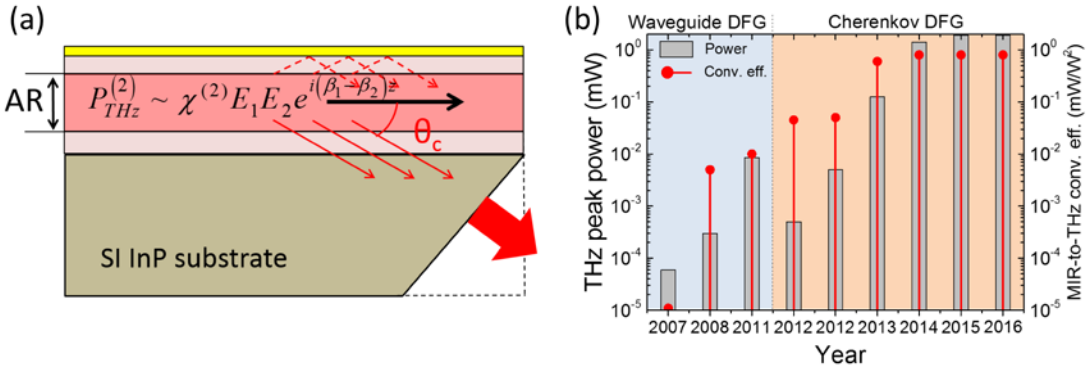

Figure 1.4: Timeline for the maximum peak power output in pulsed mode at room-temperature achieved by THz DFG–QCLs from the initial demonstration in 2007 until 2016. The data for 2007 is given at 80 K; all other data is at room temperature.

A promising approach to producing room temperature semiconductor THz sources is based on intra-cavity difference frequency generation (DFG) in dual-wavelength mid-IR QCLs [21-36]. One of the unique features for this THz source is that it could work at room temperature since it does not require a population inversion across the THz transition. Mid-IR QCLs are a rather mature technology, have favorable room temperature performance characteristics, and are able to deliver several hundred milliwatts power output in continuous-wave operation mode. Benefitting from the large level of optical nonlinearity of the quantum wells employed as their gain medium (several orders of magnitude larger than traditional nonlinear crystals), mid-IR QCLs can be designed to generate THz light via the nonlinear optical process of difference-frequency generation (DFG). Such THz sources based on this concept are called THz DFG-QCLs. Since their first demonstration in 2007, the performance characteristics of these devices have improved dramatically. THz DFG-QCL has demonstrated narrow linewidth tuning from 1.2 to 5.9 THz using an external cavity system [24,26], a variety of monolithic THz DFG-QCL sources have also been demonstrated using dual-period DFB or DBR gratings based on thermal tuning of the mid-

IR pumps [25,35,29]. The power output of these devices has experienced exponential growth as well, as shown in Figure 1.4. Recent advances include a demonstration of room-temperature 3.5 THz DFG–QCLs with THz peak power output of 1.9mW [34] and room-temperature CW devices with over 3 μW of THz power output at 3.6 THz [33, 34] by the Razeghi group. Other recent advances also include a new active region design for THz DFG QCLs based on a dual upper state design with 1.5–2 times higher optical nonlinearity for THz DFG compared to the typical bound-to-continuum active region design [36].

1.3 Dissertation overview

This dissertation describes my development of THz DFG-QCLs, focusing on expanding spectral tuning ability over the whole 1 to 6 THz range, understanding the design rules and experimentally measuring critical internal parameters of THz DFG-QCLs, and further improving device power performance and conversion efficiency. Chapter 2 provides a background introduction of THz DFG-QCLs, from their initial demonstration to the current status of the field. Basic device concepts will be included in this chapter, as well as the standard device fabrication techniques and characterization methods. Chapter 3 presents an overview of the technology and theory necessary for achieving wavelength tuning within QCLs. Chapter 4 discusses work done on demonstrating a broadly tunable THz DFG-QCL source with record tuning range from 1.2 to 5.9 THz by combining a monolithic DFG grating structure with an external diffraction grating. Chapter 5 presents the work on demonstrating a double-Littrow external cavity THz DFG-QCL system capable of determining the best THz performance position by spectrally scanning two mid-infrared pump positions continuously and individually. This technique also allows experimental measurement of critical internal device parameters for further improvement of THz DFG-QCLs. Chapters 4 and 5 focus more on wavelength tuning, while Chapter 6

discusses more details of the physical design of THz DFG-QCLs. This chapter talks about the origin of nonlinearity in THz DFG-QCLs and shows that an additional nonlinear mechanism termed ‘optical rectification’ will also contribute to the total nonlinearity and the final efficiency of THz DFG-QCLs. It also presents the experimental results of a new active region design for THz DFG-QCLs with one order of magnitude increase in the mid-IR-to-THz conversion efficiency. Finally, chapter 7 provides a summary and outlook of this dissertation.

Chapter2: THz DFG-QCL Technology

2.1 Introduction of intersubband transitions and quantum cascade lasers

Traditional bipolar semiconductor lasers working in near-infrared or visible depends on interband transitions. Laser transition in these devices happens between a conduction band and a valence band and the emitting wavelength of these lasers are determined by the bandgap of the material (Figure 2.1(a)). However, generating photons with longer wavelength (>5 μm) using interband transitions requires the bandgap of the material to be smaller. Such requirements are hard to achieve simply by adjusting the material composition due to the constraints of lattice match condition and other effects. Currently, lasers based on interband transition still hard to work at longer infrared wavelength (>5 μm).

In 1972, Kazarinov and Suris theoretically propose light amplification between discrete subband states [37], their work demonstrated that intersubband transitions in GaAs-AlGaAs quantum wells could be used to create gain. Due to the atomic-like joint density of states for intersubband transitions (Figure 2.1(b)), their gain linewidth is narrow compared with that of interband transitions. Another fundamental characteristic of intersubband transitions is their short lifetimes. For subbands separated by more than optical phonon energy, the dominant scattering process is the emission of such phonons, resulting in lifetimes of the order of one picosecond.

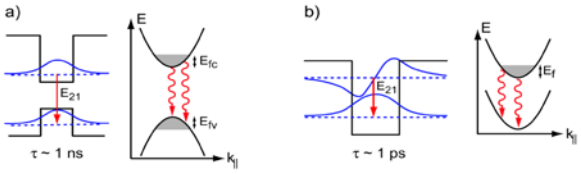

Figure 2.1: Principal characteristics of (a) an interband transition and (b) an intersubband transition in a quantum well.

With the development of molecular beam epitaxy (MBE) technology that can grow quantum structure with atomic precision, as well as the extensive understanding of quantum well structures, the first unipolar intersubband laser, i.e. Quantum cascade laser was demonstrated in Bell labs in 1994 [38]. This breakthrough was achieved by using a cascaded structure in which each period consists of an undoped active region and an n-doped relaxation/injection region (see Figure 2.2). The active region is a three-level system in which population inversion between levels 3 and 2 is achieved by engineering of the lifetimes. In Figure 2.2(b) electrons make radiative transitions from the upper laser state to the lower laser state and relax to the lowest state in the active regions. Then the electrons are extracted from the active region and injected into the following active region. The region, so-called injector, between two active regions has two important roles: depopulating electrons from the upstream active region and injecting electrons into the

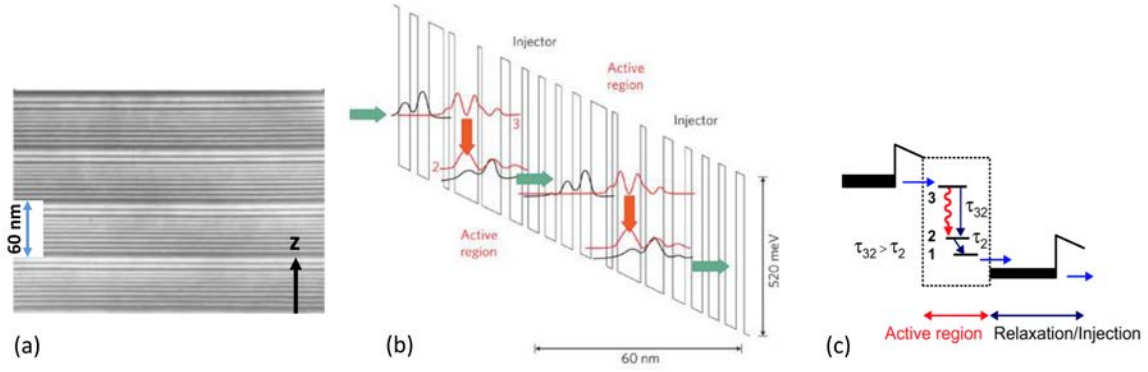

Figure 2.2: (a) Transmission electron microscopy micrograph of cross-section of part of the QCL active region. The well and barrier layers have white and black contrast, respectively. (b) Conduction band diagram of a quantum cascade laser. Each stage of the structure consists of an active region and a relaxation/injection region. (c) General philosophy of the design. The active region is a three-level system. The lifetime of the 3 → 2 transition has to be longer than the lifetime of level 2 to obtain population inversion.

upper laser state in the following active region. One active region and one injector can form one period in a QC structure. Figure 2.2(a) shows the transmission electron microscopy micrograph of a cross-section of four periods of such structure. Another fundamental aspect of QC lasers is the cascaded structure. One electron going through multiple stages and generating multiple photons.

Since the invention of quantum cascade lasers (QCL), significant efforts have been put to increase its temperature and power performance and expand its spectral range. Currently, QCL has established itself as the leading mid-infrared (mid-IR) source of coherent radiation due to the ability to tailor the emission wavelength across the entire mid-IR spectrum, from 3 to beyond 20 μm, its unprecedented tunability and high performance operation at room temperature in the two atmospheric windows with pulsed and continuous-wave (CW) powers up to 100 and 10W respectively [39,40]. QCL based spectroscopy and its applications to chemical sensing, trace gas analysis for applications such as pollution monitoring, industrial process control, combustion diagnostics, health care (medical diagnostics such as breath analysis, surgery) have seen an unprecedented growth scientifically, technologically and commercially with about thirty companies active [41]. It's unique ultra-fast carrier relaxation lifetime makes it ideally suited for high-speed operation, like high-speed digital modulation and optical wireless communication [42,43].

2.2 Intersubband nonlinear susceptibility in quantum wells

The response of a system to optical fields can be characterized by the electric susceptibility. For sufficiently weak fields, the macroscopic dipole moment density $\vec{P}$ induced by an applied field $\vec{E}$ is given by a linear constitutive relation $\vec{P}_{linear} = \varepsilon_0 \chi^{(1)} \vec{E}$; for strong fields, however, the linear equation describing dipole motion breaks down and

nonlinear effects must be considered. The dipole moment density that accounts for nonlinearities can be expressed as the following:

$$\vec{P} = \vec{P}_{linear} + \vec{P}_{NL} = \varepsilon_0\{\chi^{(1)} \cdot \vec{E} + \chi^{(2)} \cdot \vec{E}\vec{E} + \chi^{(3)} \cdot \vec{E}\vec{E}\vec{E} + ...\} \quad (2.1)$$

The coefficient of the quadratic term, $\chi^{(2)}$, is called the second order nonlinear susceptibility, while $\chi^{(3)}$ is the third order nonlinear susceptibility, and so on. Note that these coefficients are complex and frequency dependent tensor quantities. In QCLs, second order susceptibility $\chi^{(2)}$ can be designed to be 10^{-8} m/V, such large value of $\chi^{(2)}$ makes QCL good candidate for DFG nonlinear process. The third order susceptibility $\chi^{(3)}$ can be designed to be on the order of 10^{-15} m^2/V^2 [45], making QCL excellent for four-wave mixing process [45] and mid-IR frequency comb generation [65].

Follow the pioneering work of investigating nonlinear susceptibility in intersubband transitions in the 1980s, huge second-order or third-order nonlinearity in intersubband transitions have been deduced from second harmonic generation (SHG), optical rectification, third harmonic generation, difference frequency generation (DFG) in quantum wells [44,46]. These large nonlinearities, several orders of magnitude larger than bulk crystals, have mainly two origins. First, the dipole matrix elements associated with the intersubband transitions have the same order of magnitude as the quantum well width, in the few-nanometer range instead of the few picometers obtained in a usual molecular system. Second, asymmetry (which is essential for second-order nonlinearity) of quantum wells can be made by application of an electric field or bandgap engineering. Since nonlinear susceptibility is proportional to a product of transition dipole moments, strong nonlinear optical effects could be obtained in these quantum wells.

Some of these nonlinear experiments on intersubband transitions are used for far-infrared generation; one noticeable is the far-infrared generation by different-frequency

mixing in a coupled quantum well by Sirtori et. al in 1994 [46], where two external CO_2 lasers were used to pump a coupled quantum well, which was designed as shown in Figure 2.3(a), such that the external pump field and THz wave are in double resonance with the intersubband transitions.

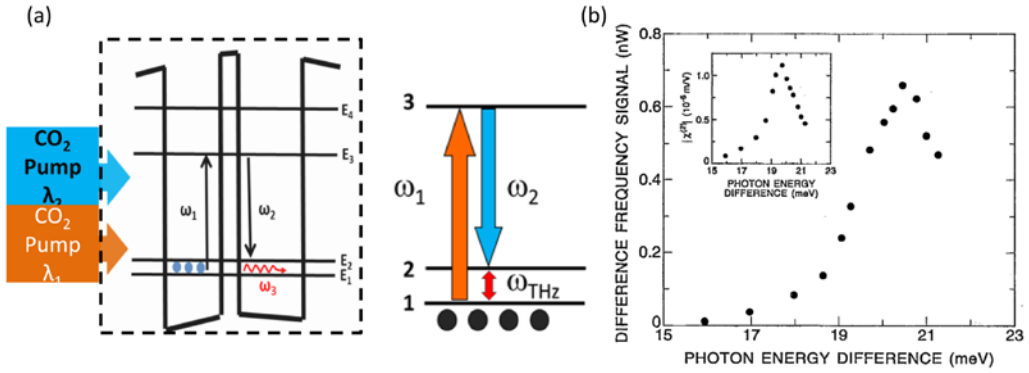

Figure 2.3: DFG generation in quantum wells [46]. (a) Energy band diagram of a single period of the GaAs/$Al_{0.33}Ga_{0.67}As$ coupled-well structure. (b) Far-IR power as a function of photon energy difference between the pump beams at 7 K temperature. The power of each pump beam is 100 mW. From these data the difference-frequency dependence of the susceptibility $\chi^{(2)}(\omega_3 = \omega_1 - \omega_2)$ is obtained (inset).

The resonant nonlinear susceptibility $\chi^{(2)}$ in this quantum well can be expressed as (including only resonant terms and neglect population on higher (n = 2 and 3) energy levels):

$$\chi^{(2)}(\omega_3 = \omega_1 - \omega_2) = N_e \frac{e^3}{\hbar^2 \varepsilon_0} \times \frac{z_{12} z_{23} z_{31}}{(\omega_3 - \omega_{23} + i\Gamma_{23})} \left(\frac{1}{\omega_1 - \omega_{13} + i\Gamma_{13}} + \frac{1}{\omega_{12} - \omega_2 + i\Gamma_{12}} \right) \qquad (2.2)$$

where ω_1 and ω_2 are the frequencies of mid-IR pumps, $\omega_{THz}=\omega_1-\omega_2$ is THz difference-frequency, ΔN_e is the population inversion density, ez_{ij}, ω_{ij}, and $2\Gamma_{ij}$ are the transition dipole moments, transition frequency, transition linewidth between states i and j. $\chi^{(2)}$ was calculated to be around 10^6 pm/V in this structure, it is four orders of magnitude higher than traditional bulk crystals. However, the resonant condition in passive structure will also

introduce strong absorption of the pump and the generated THz fields which limit its application for an efficient THz source. To avoid strong absorption, one way is to use an active nonlinear medium that could provide laser gain for two pumps, so that the nonlinear medium have both laser gain and giant $\chi^{(2)}$. The most promising active nonlinear medium would be mid-infrared quantum cascade lasers, which can provide large laser gain at room temperature, and can be engineered to have giant nonlinearity.

2.3 Intra-cavity difference frequency generation in mid-infrared quantum cascade lasers

Difference-frequency generation (DFG) has been traditionally employed to generate THz emission using nonlinear crystals, it is a nonlinear optical process in which two beams at frequencies ω_1 and ω_2 interact in a medium with second-order nonlinear susceptibility $\chi^{(2)}$, to produce radiation at frequency $\omega = \omega_1 - \omega_2$. The intensity of the generated wave at frequency $\omega = \omega_1 - \omega_2$ is given by the expression:

$$W(\omega = \omega_1 - \omega_2) = \frac{\omega^2}{8\varepsilon_0 c^3 n(\omega_1) n(\omega_2) n(\omega)} \left|\chi^{(2)}\right|^2 \times \frac{W(\omega_1) W(\omega_2)}{Seff} \times l_{coh}^2 \qquad (2.3)$$

where $l_{coh}^2 = \left((k_1 - k_2 - k_{THz})^2 + (\alpha_{THz}/2)^2 \right)^{-1}$ is the coherence length, $W(\omega_i)$, $n(\omega_i)$, k_i and α_i are the pump intensity, effective refractive index, wave vector and loss of the beam at ω_i, S_{eff} is the effective area of the interaction.

The first proof of principle intra-cavity difference frequency generation in mid-IR QCLs was demonstrated by Dr. Mikhail Belkin in 2007 and 2008 when he works as a postdoc in Cappasso's group [21,22]. Giant $\chi^{(2)}$ was implemented in one of the substacks of a dual wavelength QCL structure, depicted in the schematic in Figure 2.4(a). Compared to the previous demonstration of giant $\chi^{(2)}$ integration in a passive structure, $\chi^{(2)}$ in this structure now has population inversion from the laser gain, avoid strong pump absorption

issues. Figure 2.4(b) shows the device L-I and I-V information of mid-IR pumps as well as the mid-IR spectrum in the inset. Figure 2.4(c) shows the device THz spectra. Proof of principle device can provide 300 nW peak THz power and 5 $\mu W/W^2$ mid-infrared to THz conversion efficiency at room temperature.

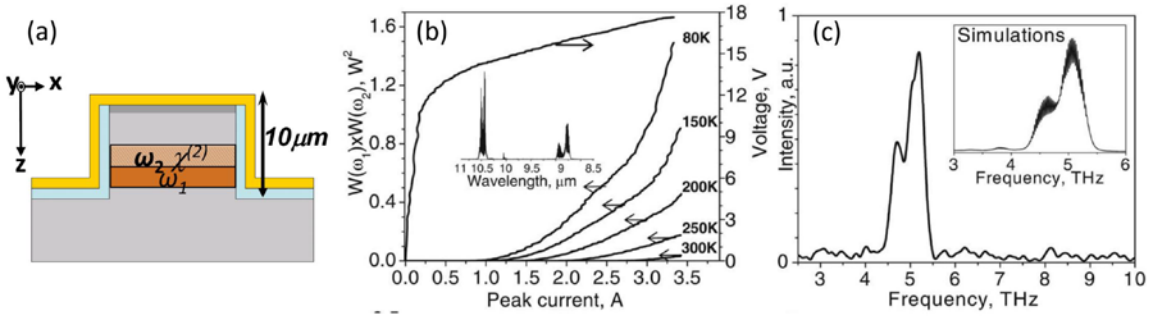

Figure 2.4: DFG in QCLs [22]. (a) Schematic of the waveguide structure of the device. The insulating Si_3N_4 layer is in green, and the semiconductor is in gray for low-doped InP layers and orange for two active region sections. (b) The product of mid-IR pump intensities vs current (left axis) and current-voltage (right axis) characteristics of a representative device. Inset: mid-IR emission spectrum of the device at 80 K. (c) THz spectra of the device in (b) at 80K. Inset: THz DFG spectrum simulated from mid-IR spectrum in (b).

2.3.1 Collinear modal phase matching for difference frequency generation

This first generation of DFG QCL design is based on a collinear modal phase matching scheme that both mid-IR pumps and THz signal propagate along the same x direction (see Figure 2.4(b)), and satisfy $k_{THz} = k_1 - k_2$. The phase matching condition can be satisfied by adjusting doping and thickness of the active region. However, certain design can only satisfy for certain THz frequencies because the material is dispersive, making it not suitable for demonstrating a broadly tunable device. Another detrimental factor of modal phase matching is the small coherence length (l_{coh}) of THz emission. Free carriers in the cladding layer and the active region of the QCL structure have strong absorption for

DFG THz emission, in the range of 10^2~10^4 cm^{-1}. For example, absorption coefficient α of a typical InP cladding layer (2e10^{16} cm^{-3} doping concentration) is around 100 cm^{-1} at 4 THz(shown in Figure 2.4(a)), under perfect phase matching condition when $k_{THz} = k_1 - k_2$, effective propagation length is only 200 μm. That means for a typical 2~4 mm-long device, only 5%~10% of the THz signal can reach the output facet, all the THz emission along the rest of the active region has been absorbed. For lower THz frequencies, the absorption is even stronger.

2.3.2 Cherenkov phase matching for difference frequency generation

Later in 2012, a Cherenkov phase matching scheme that allows THz extraction along the whole length of the waveguide was demonstrated by our group [23]. Cherenkov emission is characterized by a THz leaky mode that propagates out of the active region at a discrete angle. It occurs when the nonlinear polarization wave in the active region propagates faster than that of THz radiation in the substrate. In terms of wave vector, it means THz wave vector in the substrate $k_{sub}(\omega_{THz})$ is larger than the nonlinear polarization wave vector (β_1- β_2), where β_1 and β_2 are the propagation constant of two mid-IR pumps. The phase matching condition can be written related with Cherenkov angle θ_c so that the parallel component of the wave vector can be conserved:

$$k_{sub}^{(\omega_{THz})} \cos\theta_c = \beta_1 - \beta_2 = n_{group}\omega_{THz} / c \tag{2.4}$$

n_{group} is the group index of mid-IR pumps. Cherenkov angle at 4 THz is around 20 degrees and the substrate facet has to be polished at an angle to avoid total internal reflection for THz radiation, as shown in Figure 2.5(a). Semi-insulating InP substrate was used to extract THz radiation through the polished substrate facet, so a side-contact a side-contact current extraction pattern was employed, shown in Figure 2.5(b).

Figure 2.5(c) compares the measured far field profile of three different devices: a regular modal-phase matching device with doped substrate, 20˚ polished Cherenkov DFG device and 30˚ polished Cherenkov DFG device. It clearly shows a directional THz emission from the polished Cherenkov device, this is because the Cherenkov THz signal emits from a larger area of the substrate facet.

The benefit of this scheme not only lies in the directional THz emission and more efficient THz extraction along the whole length of the device, but also in the broadband phase matching condition that can work for any THz frequency. This allows us to demonstrate broadly tunable THz DFG-QCLs in Chapter 4 and Chapter 5.

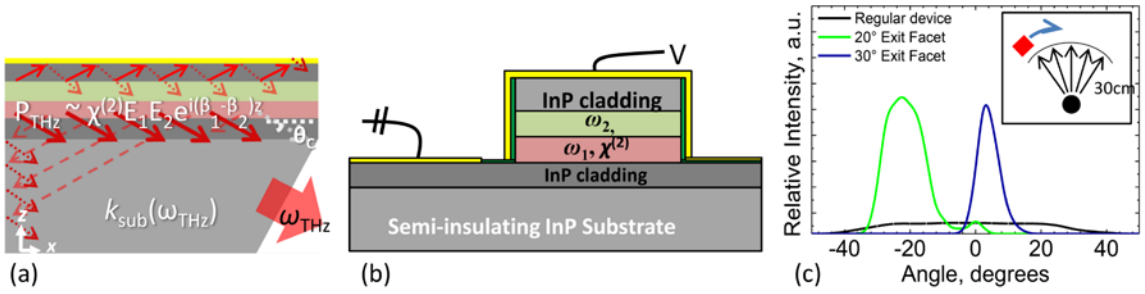

Figure 2.5: (a) Schematic diagram of leaky Cherenkov mode in the QCL waveguide, Cherenkov THz emission is represented by red arrows. (b) A side-contact current extraction pattern was employed in Cherenkov DFG-QCLs. (c) Far-field measurement of three devices, regular modal-phase matching device (black line), 20˚ polished Cherenkov DFG device (green line) and 30˚ polished Cherenkov DFG device (blue line) [23].

2.4 Device fabrication

All the THz DFG-QCL designs discussed in this thesis were grown with molecular beam epitaxy (MBE) by Prof. Amann's group at the Technical University of Munich or with metalorganic vapor phase epitaxy (MOCVD) by Prof. Dan's group at the University of Wisconsin-Madison, and Hamamatsu Photonics, a Japanese company.

The devices discussed in this thesis include Fabry-Perot devices, single-period DFB/DBR devices, dual-period DFB devices, and III-V device transfer/bonding on silicon. The fabrication of all these devices includes steps like ridge define, open window, metallization, and packaging, while for DFB devices, additional steps to define gratings on the ridge using electron beam lithography needs to be done as the first step. For III-V transfer on silicon devices, the bonding step is the last step after ridge define and metallization. One substrate transfer method is to cleave the device after standard QCL fabrication and form the facet mirror first, thin down the InP substrate to ~100 nm and adhesively bond the III-V device to silicon using a thin SU8 layer. In terms of mass production, this process is not favorable because polishing and bonding can only be applied to a single laser bar each time. Another substrate transfer method is to epi-transfer a large piece of processed III-V device to silicon using selective wet-etching and adhesive SU8 bonding first and then dice device into laser bars. Since it is hard to cleave silicon with good facets, dicing silicon will be a better choice, with the right choice of the dicing blade, both facets of the III-V material and the silicon substrate can remain in a relatively good condition.

To include all the fabrication steps, I will discuss a DFB device bonding on silicon substrate as an example. All the devices discussed in this dissertation use surface DFB gratings, where DFB gratings are defined on top of the cladding layer and in contact with the top metal. First, the DFB grating pattern is defined by electron beam lithography because it is flexible for different designs and provides high-resolution features, in comparison to the conventional UV 400 photolithography system available in our center. The grating writing time is considerably higher.

The second step is defining a laser ridge in the DFB grating position, followed by formation of a silicon nitride open window on top of the ridge, finished with metal deposition and electroplating. Then a device bar is cleaved, followed by an InP substrate

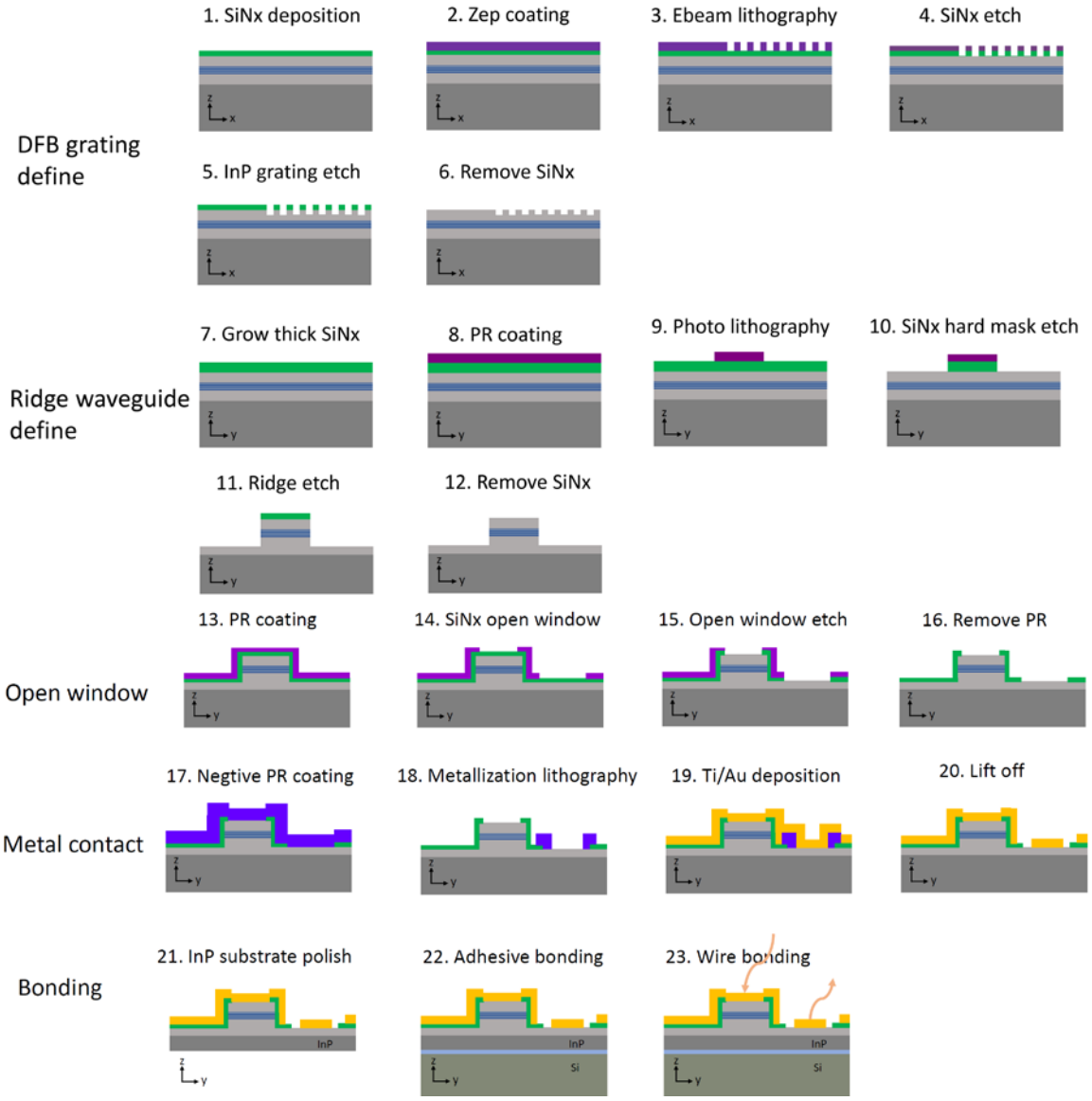

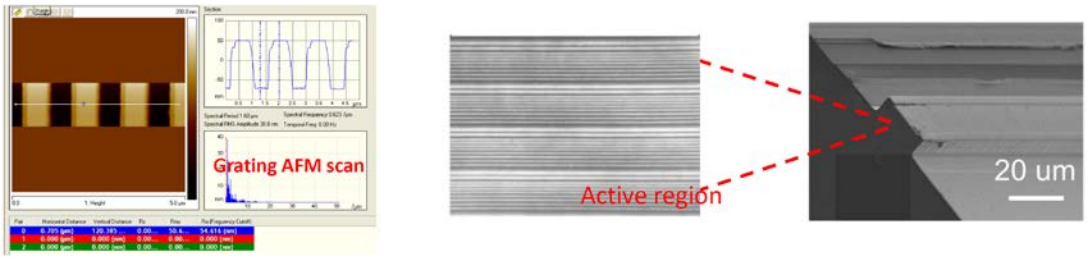

Figure 2.6: Schematics of device fabrication steps. The last three pictures are the AFM scan profile of the DFB grating in the first step, the TEM scan of the active region of the device, and the SEM picture of the final ridge device respectively.

thinned down to 100 nm. The polished device is then adhesive bond to a high resistivity silicon substrate. The whole fabrication process is summarized in Figure 2.6.

2.4.1 DFB grating define

We start the fabrication by depositing 150–300 nm SiNx layer on top of the semiconductor wafer using plasma enhanced chemical vapor deposition (PECVD). The purpose of this layer is to use it as a highly selective hard mask to transfer the DFB grating structure into the semiconductor top cladding layer using dry etching. Then a ~200-nm-thick E-beam resist (Zep 520) is spun on the wafer, followed by baking at 180° C for two minutes. The resist is exposed in a JEOL E-beam writer at an accelerating voltage of 50 kV and a beam current of 300 pA. Exposure conditions are optimized by careful control of the exposure dose.

After developing grating patterns, the grating depth and shape are examined with atomic force microscopy (AFM). Once a good grating pattern is achieved, the E-beam resist grating pattern is used to etch SiNx hard mask using reactive ion etching (RIE). The etch selectivity and etch rate should be careful controlled by controlling the gas (CHF_3/O_2) power and pressure. The residual E-beam resist is removed by dry etching with O_2 plasma followed by PR remover as well. The SiNx hard mask is then used to etch top cladding

layer (InP) of the semiconductor surface using inductive coupled plasma (ICP)-RIE (Cl_2/N_2), the key of this etching recipe is to balance the chemical etching and the physical etching so as to obtain a smooth surface and a straight sidewall (shown in Figure 2.6). Extra SiNx is removed with RIE or wet etching chemicals (dilute HCl).

2.4.2 Ridge waveguide define

After DFB gratings are etched into the wafer surface, the next step will be to define the laser ridge waveguide. The width of the waveguide is usually 12–32 μm, and there is no limitation on the length of the waveguide. This large feature size could be easily achieved with the conventional UV 400 photolithography system that our center provides. It should be noted that the ridge position should be defined right overlapped with the surface DFB grating position as this manual alignment is kind of critical. Typically, the width of the DFB gratings is designed to be 2 μm larger than the waveguide ridge width to include some alignment tolerance. The ridge waveguide define also starts with SiNx growth as the hard mask, ~1 μm thick. The surface of the SiNx is treated with O_2 plasma to improve adhesion with photo resist (PR), 2-μm-thick PR is then spun on the SiNx surface, soft baked, and exposed. Then PR pattern is transferred to SiNx hard mask with RIE, before removing extra PR with Acetone, O_2 plasma is used to remove some of the etch residual on the surface. Then III-V cladding layer and the active region are etched with ICP RIE with gas $Cl_2/CH_4/H_2$ using ~1 μm thick SiNx as a hard mask. Selectivity between SiNx and III-V material (InGaAs/InAlAs/InP) is about 1:7. Extra SiNx is removed with RIE or ICP RIE.

2.4.3 SiNx insulating and open window define

A ~600-nm-thick SiNx layer is grown again on the ridge waveguide. The purpose of this layer is to confine the mode in the active region and to reduce optical loss, as well as to isolate current injection into the sidewall of the ridge waveguide. To allow current injection from the top to the bottom of the waveguide, a SiNx window is opened on top of the waveguide using a photolithography scheme again. A relatively thick PR should be chosen due to the high step structure of the waveguide, which results in much thinner PR on top of the ridge waveguide than on the bottom of the ridge waveguide. As this thesis focus on Cherenkov-type THz DFG-QCLs with THz emission coupled out from the substrate, semi-insulating or high-resistance substrate is usually used, and the typical top to bottom current injection scheme does not work. Instead, a current injection layer is grown before the bottom cladding layer during the wafer growth, which allows side current injection/extraction from the top of the waveguide to the side of the waveguide, which will be coated with gold as the ground contact.

2.4.4 Metal contact

After the SiNx window is etched, the next step is to make metal contact. We use a lithography, metal deposition, and liftoff process. A 7–8-μm-thick negative PR (NLOF 2070) is used, the undercut depth of the PR could be carefully controlled with exposure time. After thorough developing the exposed PR, a descum process is used to remove any undeveloped photoresist residual. Right before the deposition of metal, acid treatment of the wafer surface is important to remove any oxide formation on the semiconductor surface. Dip the wafer in dilute HCl (HCl : H_2O = 1:10) for 1 min is usually used by us as the acid treatment before metallization. Then a 20-nm-thick titanium and 200-nm-thick gold is deposited on the wafer surface at a 45-degree angle and another deposition of 20-

nm-thick Ti and 200-nm-thick Au is deposited at the opposite 45-degree angle. The device is then soaked in acetone to remove the gold on the PR, and sometimes a light sonication will be used to facilitate the lift-off process. For high-duty cycle operation of our devices, 400-nm-thick gold is not enough. In this case, a layer of electroplated gold will be added. The electroplating process starts with the same lithography step as for metal contact. A positive PR with no undercut should be ideal, but a negative PR with little or no undercut by controlling the exposure time could also be used in our case. Then a thin layer of silver paste is added on the edges of the wafer to connect every ridge as well as to stick to a copper strip. Devices are then seated in gold solution for several hours.

2.4.5 Substrate transfer and device packaging

After electroplating, the device is cleaved into laser bars, the substrate is thinned down to 100 nm thick, and a high resistance silicon wafer is cleaved into 3–4-mm-long pieces with one facet polished at a 30-degree angle. A thin layer of SU8 is spun on the silicon piece, then the polished laser bars are transferred onto this prepared silicon piece under vacuum conditions with some pressure. Then the laser bars are ready to mount on a copper sink (with indium paste) with laser bars on top and substrate in contact with copper sink, and wire bonded for testing. Other techniques like epi-down mounting with laser bars facing the copper sink can give better thermal conductance for the package, which is really important for CW operation of the device. But since this thesis focus on the fundamental understanding of THz DFG-QCL core design, epi-up mounting is used for all the devices I discussed.

2.5 Experimental set-up and device characterization

A variety of measurements have been performed to fully characterize laser devices. The primary measurements include spectrum radiation from spontaneous and stimulated emission in mid-infrared and terahertz range, light output versus current (L-I), and current versus voltage (I-V), far-field pattern of the lasing mode. Dynamic performance of the lasing mode in a short time window is measured for some devices as well.

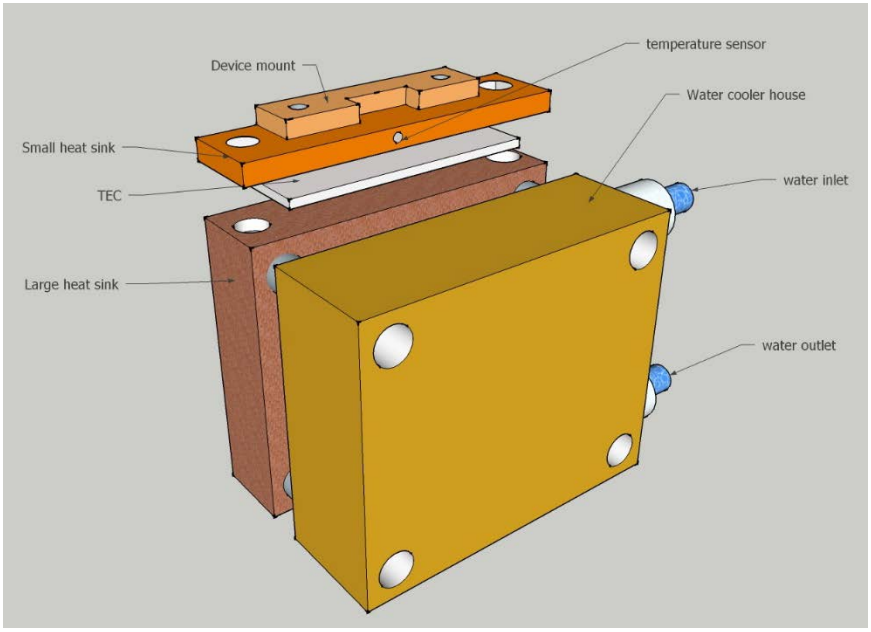

Figure 2.7: QCL house. Devices seated in the device position on the top copper sink, the top heat sink and the bottom larger copper heat sink are connected with a Peltier module controlled by a temperature controller. The bottom heat sink is attached to a water cooling house.

2.5.1 Device mounting techniques

After device fabrication, devices are cleaved into laser bars and soldered on the copper mount using indium, and then device mount is placed on top of a QCL house for testing, as shown in Figure 2.7. The QCL house contains a TEC cooler as well as a water cooler. The TEC cooler includes both a small and a large copper heat sink, with a

thermoelectric/Peltier module connected in between. A temperature sensor used to measure the device temperature is buried in the small heat sink, close to the device position. For low threshold and low duty-cycle operation, TEC cooler is enough to maintain a room-temperature operation condition, while for high-duty cycle and CW operation, the water cooler is necessary to extract heat from the large copper heat sink.

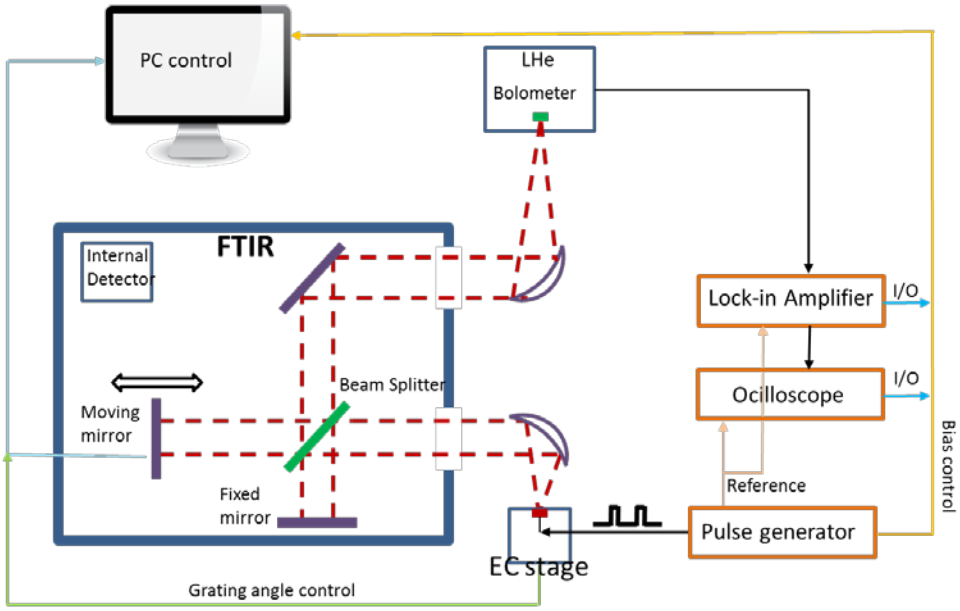

Figure 2.8: Schematic of experimental set-up of spectral measurement

2.5.1 Spectral measurements

The laser emission spectra are measured with either a Nicolet or a Bruker FTIR, and the schematic experimental set-up is shown in Figure 2.8. Devices are placed on a TEC controllable or water cooling stage for testing, and laser emission is collected with a parabolic mirror (2-inch focal length) and sent to FTIR. An internal deuterated L-alanine doped triglycine sulphate detector (DTGS) is used to detect mid-infrared lasing emission while an external helium-cooled bolometer is used to detect THz emission. The THz

emission is collected and focused to the external bolometer by another parabolic mirror (4- or 6-inch focal length).

The working principle of FTIR is to use a Michelson interferometer to trace out an interferogram, which is then Fourier transformed to yield the power spectrum of the input laser emission. For large-lasing signals, such as the mid-infrared pump emission, FTIR is performed in a linear-scan mode, where the moving mirror in the FTIR translates smoothly while tracing the interferogram, data collection time is usually less than 1 minute. However, for small signal emission, such as mid-infrared QCL spontaneous emission, and some of the DFG-QCL THz emission, a step-scan mode needs to be performed, where the moving mirror pauses at each step to allow processing of a small signal from lock-in amplifier. The step time of the FTIR is usually set to be three times or higher of the lock-in integration time, which allow full integration at each step.

Spectral measurement in the mid-infrared range is relatively easy to obtain since the laser signal is much larger, and the atmospheric absorption is relatively small. But spectral measurement in the THz range is complicated by the presence of strong water absorption, even when the system is operated under dry nitrogen-purged condition. The strong water absorption can be reduced, but it cannot be fully resolved.

2.5.2 Dynamic measurement

In some situations, the dynamic performance of the generated modes at different delay time windows of the applied current pulses needs to be measured. As we will mention in Chapter 4, such measurements are essential to understanding mode competitions when there are multiple modes with different round-trip times in the cavity. The measurement set-up for spectra during short-time windows at various instants during the pulse is shown in Figure 2.9. Our QCL is biased with a pulse generator with repetition frequency of 20 kHz (the

repetition frequency should be set in the range below the maximum operation frequency of the boxcar). The laser signal is sent to the FTIR (Bruker 70), and collected with a fast room-temperature MCT detector as the external detector of the FTIR. The collected signal is then amplified and sent to a gated boxcar integrator, which is triggered by the pulse generator. Tuning the boxcar at variable gate delay with width of 2~5 ns, we measured the output spectra at various parts of the applied pulses.

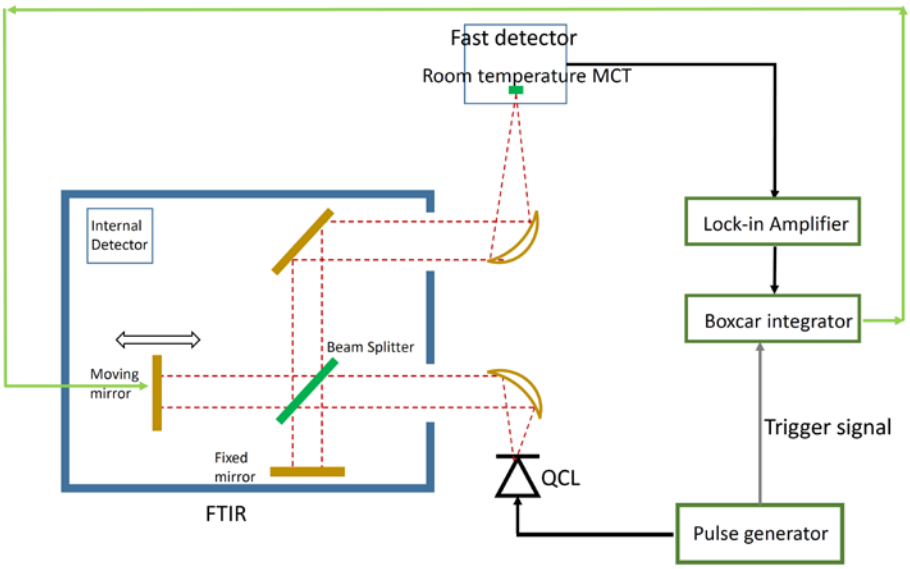

Figure 2.9: Schematic of the experimental set-up for dynamic spectra measurements at various parts of the applied pulse.

2.5.3 L-I-V curve characterization

Due to large optical loss induced by internal mirrors or beam splitter inside FTIR, power spectra shown on FTIR is only a relevant power. It is hard to measure the collection efficiency of FTIR. A more accurate way to measure power is to send laser emissions directly to a detector. The power measurement set-up is shown in Figure 2.10. A 2-inch focal length parabolic mirror is used to collect either mid-infrared emission or THz

emission from the laser facet, and then the collimated beam is focused onto a thermopile for mid-infrared emission with a ZnSe window in front or onto a calibrated bolometer or a Golay cell for THz emission with a quartz window in front. To be more accurate, we usually put the set-up in a dry N_2 purged environment to reduce the H_2O absorption feature in the THz range, without pumping the system though.

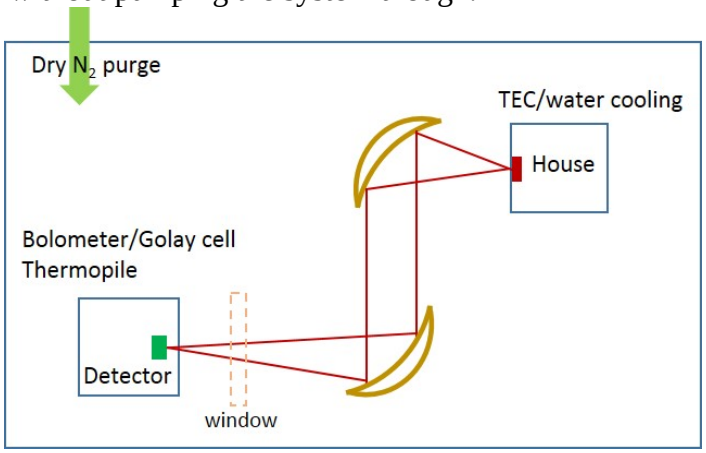

Figure 2.10: Schematic of experimental set-up for power characterization. A 70% collection efficiency is corrected for mid-IR power, and no correction for the collection efficiency is applied to THz power for all the reported THz power in this dissertation.

2.6 Summary

To summarize, I briefly introduce the background and development history of QCLs, which laid the foundation of THz DFG-QCLs. Then I introduce the early investigation and pioneering work of THz DFG-QCLs by Prof. Mikhail Belkin and former group members.

In the second part of the chapter, I discuss the fabrication procedures I adopt to make Fabry-Perot devices, single period/dual period DFB grating devices and substrate transfer devices shown in later chapters. Moreover, I show a QCL testing house I developed and other characterization set-ups used for most of the devices I present in this dissertation.

Chapter3: Wavelength control of quantum cascade lasers

3.1 Mode control of mid-infrared quantum cascade lasers

For many applications in spectroscopy, sensing, heterodyne detection, communication, and imaging, single-mode narrow-linewidth tunable lasers are desirable. Distributed feedback cavity and external feedback cavity are usually used in semiconductor lasers to achieve narrow linewidth laser emission. This section will take an overview of different feedback mechanisms that could be used to achieve narrow linewidth as well as wavelength tuning.

3.1.1 Fabry-Perot cavity

Fabry-Perot cavity is the most common cavity in semiconductor lasers. A Fabry-Perot cavity is naturally formed at the cleaved facet after cleaving the ridge of the quantum cascade laser into 1-4 mm. A stationary mode is created in the cavity when the field close on itself after a round-trip in the cavity, $\exp(i2\beta L) = 1$ ($\beta = 2\pi n_{eff}/\lambda$ is the wave vector), from where the mode spacing between adjacent cavity modes can be deduced as (in terms of wavenumber):

$$\Delta(\frac{1}{\lambda}) = \frac{1}{2L(n_{eff} + \frac{1}{\lambda}\frac{\partial n_{eff}}{\partial(1/\lambda)})} = \frac{1}{2L \times n_{group}} \tag{3.1}$$

where L is the length of the cavity, n_{eff} is the effective index at wavelength λ and n_{group} is the group index of the lasing modes.

For a typical Fabry-Perot cavity of QCL, the mode spacing is in the order of 1 cm^{-1}, which is much narrower than the gain bandwidth of 100~200 cm^{-1}. This results in multi-modes lasing in a broad location without possibility to predict an exact location.

3.1.2 Distributed feedback cavity

One way to select single mode at an expect frequency location is to incorporate a distributed feedback grating (DFB) inside the active region or in between the upper cladding layer and the top metal layer. The former one is called buried DFB grating, as shown in Figure 3.1(a), which requires regrowth of the upper cladding layer after grating fabrication. The latter one is called surface DFB grating, as shown in Figure 3.1(b), which is easier to fabricate and provide both index and loss coupling between the dielectric waveguide mode and surface plasmonic mode.

Repeated scattering from a Bragg grating favors a single wavelength — the Bragg wavelength $m\lambda_B = 2n_g\Lambda$— which is determined by the grating period Λ, group refractive index n_g, m represents the order of the grating. The fundamental spectral selection mechanism of DFB structure can be explained by a model of two counter running wave coupled by backward Bragg scattering, a coupled-wave model [47]. For buried DFB gratings, only dielectric gratings in the gain medium or close to the gain medium need to be considered. In this case, the periodic variation of the index caused by DFB gratings will create a photonic gap, also called stop band around the Bragg frequency; the DFB gratings support lasing on either side of this stop band, these two modes have the lowest lasing threshold for all the possible supported modes by DFB gratings. One mode concentrate on the high index part of the grating with a complex effective index of $n_1 = c/2f_1\Lambda$, and the other mode concentrate on the low index part of the grating with a complex effective index of $n_2 = c/2f_2\Lambda$. Where f_1 and υ_2 are the complex frequencies of the two modes, the imaginary part of the index determines the loss of the mode. The coupling strength coefficient between these two modes can be expressed as:

$$\kappa = \frac{\pi\Delta n}{\lambda_B} = \frac{\pi}{\lambda_B}(n_1 - n_2) = \frac{\pi}{2\lambda_B}\left(\frac{c}{f_1\Lambda} - \frac{c}{f_2\Lambda}\right) \tag{3.2}$$

The coupling strength κL becomes a dimensionless quantity after considering grating length L. The value of the coupling strength will affect the lasing threshold, intensity distribution in the laser cavity and the power output from the device facet. Based on the approximation by Kogelnik and Shank [47], it could not provide effective feedback when coupling strength is too small ($\kappa L \ll 1$). However, when coupling strength is too large ($\kappa L \gg 1$), light tends to confine in the center part along the length of the cavity and decays towards the end of the cavity. In the critical coupling condition ($\kappa L \approx 1$), the mode intensity distributed more or less evenly along the cavity.

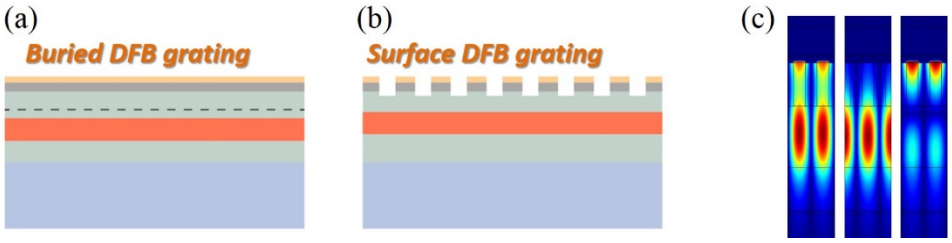

Figure 3.1: (a) Schematic of buried DFB grating in the QCLs. (b) Schematic of surface DFB grating on top of the QCL waveguide. (c) Three types of modes coupled by the surface DFB grating on QCL, simulation done with Comsol.

$$\Delta n = \min\{(n_1 - n_2), (n_2 - n_3)\} \tag{3.3}$$

The coupling strength equation may not be right for surface grating since the refractive index difference is determined by the smaller one between two modes (see Eq. 3.3). For surface DFB gratings, however, the additional surface metal grating will introduce a third surface-plasmon mode [48,49] (left picture in Figure 3.1(c)), resulting in a coupling between three modes, as shown in Figure 3.1(c). The coupling strength κL strongly depends on the grating etching depth. Figure 3.2 shows the index change of three modes as the grating etching depth changes from 50 nm to 250 nm. For shallow grating depth (<160

nm), coupling between mode 1 and mode 2 dominates, as grating depth increases, the coupling between mode 3 and mode 2 takes place.

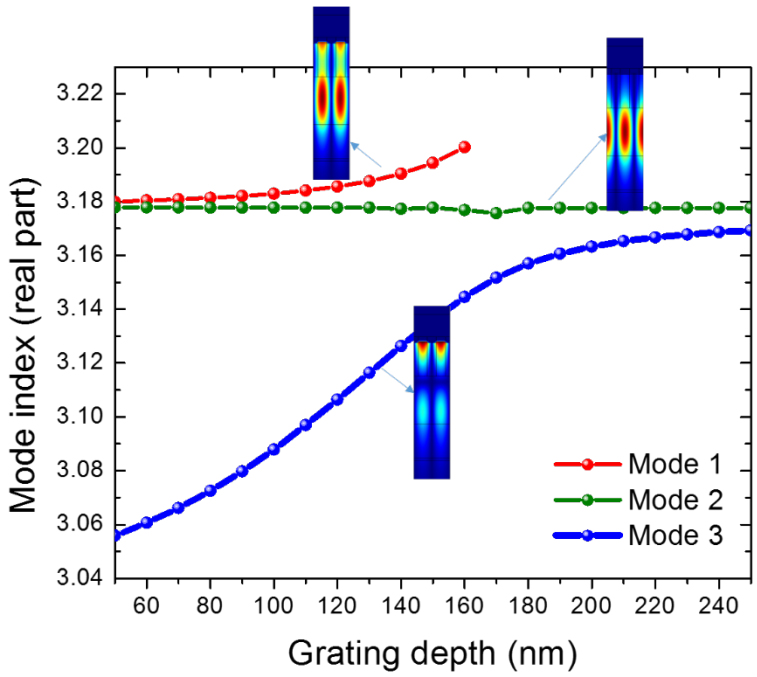

Figure 3.2: Refractive index (real part) of three modes as a function of grating etch depth. Bragg frequency is set to 10.2 μm and grating period is 1.6113 μm.

Another important feature of the DFB QCLs is that the emission wavelength can be tuned continuously by changing the heat sink temperature or injection current. In either case, the effective refractive index of the laser waveguide will be changed, thus shifted the resonance wavelength of the Bragg gratings with a running rate around 0.1-0.2 $cm^{-1}K^{-1}$. The maximum tuning range of a single DFB QCL is limited by the maximum temperature QCL could tolerate, to cover the whole gain bandwidth of a QCL chip, an array of DFB lasers could be fabricated with difference grating periods [50]. These DFB QCLs have demonstrated CW operation with watt-level power output [51].

3.1.3 External feedback cavity

Although DFB QCLs provide compact, reliable single-mode tunable laser emission, external cavity (EC) QCLs, which applies a tunable wavelength filter outside the laser cavity, are the most commonly used widely tunable single-mode sources across numerous successful applications [52-55]. Owning to their rapid progress in tunability, output power and CW operation at room temperature [55]. The most common configurations for EC QCLs are the Littrow and Littman-Metcalf configurations as shown in Figure 3.3. Wavelength tuning is achieved by the rotation of the diffraction grating for the Littrow, and the rotation of a mirror for the Littman-Metcalf configuration. The Littman configuration provides better wavelength selectivity while the Littrow provides higher back-coupling into the laser chip. Figure 3.3(c) also shows a modified double Littrow external cavity system which has been used in a diode laser system [56]. This modified one could tune two different wavelengths independently with two external diffraction gratings.

In the Littrow configuration, feedback occurs when the incident angle and the reflect angle of the diffraction grating overlap with each other, the feedback wavelength for the m-th diffraction order is:

$$m\lambda = 2\Lambda sin\theta \tag{3.4}$$

where Λ is the grating period, and θ is the incident angle. Usually, first order is used to achieve high power. The linewidth of the external cavity is very attractive if Fabry-Perot modes are suppressed, it is proportional to the inverse square of the external cavity length. It is necessary to deposit anti-reflection coating to the laser facet facing the cavity to suppress Fabry-Perot modes and ensure stable operation of the external cavity laser. Such a coating prevents the laser from operating in a mode determined purely by the facets and forces it to operate in a mode determined by the external reflector, details of the anti-reflection coating design will be given in Part 2.3.

A major advantage of EC QCLs is their potential to cover a wavelength range as wide as that allowed by the gain medium using a single QC laser chip. The key to a wide tuning range, besides an optimized, well-aligned EC set-up, is a broad gain bandwidth of the QCL. So far, bound-to-continuum [57,58], continuum-to-continuum [59] and dual-upper [60] laser state active region designs have demonstrated homogeneously broad gain bandwidth. With the introduction of heterogeneous design by integrating many sub-stacks with different wavelengths, a maximum tuning range of more than 430 cm^{-1} — over 39% of the center frequency — in an EC configuration has been achieved [54].

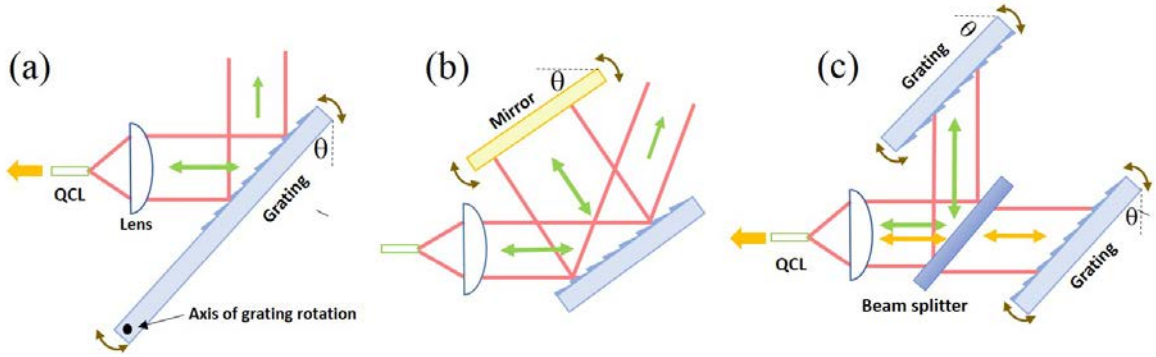

Figure 3.3: (a) Littrow external cavity configuration. (b) Littman-Metcalf external cavity configuration. (c) Modified double Littrow external cavity configuration. The green and yellow arrows indicate directions of propagation of light, and the black arrows indicate how tuning is achieved by rotating optical parts.

Although the tuning properties of the external cavity are very impressive, but even with perfect anti-reflection coating, it is not easy to achieve continuous tuning (tuning without mode hopping), continuous tuning requires the cavity length to vary in proportion to the wavelength. One way to provide simultaneous translation and rotation tuning of the diffraction grating is to move the axis of the grating rotation outside of the grating center, as shown in Figure 3.3(a). A piezo-activated cavity mode-tracking system that provides independent control of the external cavity length and diffraction grating angle for mode-

hop-free tuning was employed by Wysocki [53], that achieved a mode-hop-free fine tuning range of ~ 1.2 cm^{-1} for a 5.2 μm QCL.

3.2 Anti-reflection coating

Anti-reflection coating is a key element for both DFB QCLs and EC QCLs. Defining Bragg gratings in the laser waveguide or using external gratings to select wavelength could create desired cavities for lasing modes, note that in both cases, two cleaved facets of a laser ridge will naturally form a Fabry-Perot cavity that supports longitudinal modes in the laser cavity, thus form multiple cavities for multiples modes. These modes tend to compete with each other and the one with lower loss will dominate. The application of AR coating in either DFB or EC QCLs is expected to create high losses for Fabry-Perot modes in the cavity, so as to suppress the undesired Fabry-Perot modes and select only the desired modes support by Bragg or external gratings. QCLs without AR coating could still achieve coarse tuning, the tuning range is determined by the threshold current density of the grating selected mode and that of the Fabry-Perot modes of the chip [61]:

$$J_{th}^{FP} = \frac{\alpha_{FP}}{g_{max}}, \qquad J_{th}^{EC}(\lambda) = \frac{\alpha_{EC}(\lambda)}{g(\lambda)} \tag{3.5}$$

where α_{FP} and α_{EC} are losses of the Fabry-Perot modes and external cavity modes respectively, g_{max} is the maximum of the differential gain g(λ). Tuning is possible in the range, $J_{th}^{EC}(\lambda) \leq J_{th}^{FP}$. Though in this case, only the external cavity modes that are close to the Fabry-Perot modes of the chip can be selected.

In order to suppress Fabry-Perot modes and expand tuning bandwidth, we need to deposit high-quality AR coating on one facet of the device. A straightforward way to make an Anti-reflection coating on the facet of a QCL is to deposit a quarter-wave layer of a material with a refractive index equal to $n_c = \sqrt{n_s} \approx 1.8$, where $n_s \approx 3.2$ is the refractive

index of the QCL core region. So the problem becomes to find such a material with an expected index 1.8 that adhere well to the QCL facet and has low absorption loss in the desired wavelength. Since it is hard to find a material with an index of 1.8 for all the desired wavelength, multilayer coatings are usually used. We can use a transfer matrix model to calculate the reflectivity of a multilayer coating.

Consider a plane wave traveling in infinite, isotropic, linear, nonmagnetic media without surface charges along the z-axis and polarized along x-axis, as shown in Figure 3.4. Then Maxwell's equation in each layer can be written as:

$$\begin{aligned} \nabla \cdot E = 0 \qquad & \nabla \times E + \frac{\partial B}{\partial t} = 0 \\ \nabla \cdot \mathrm{B} = 0 \qquad & \nabla \times \mathrm{B} - \frac{n^2}{c^2}\frac{\partial E}{\partial t} = 0 \end{aligned} \tag{3.6}$$

In medium 0, the electric and magnetic field take the form:

$$\begin{aligned} E_0(x,t) &= (E_{f,0}e^{ik_0 z} + E_{b,0}e^{-ik_0 z})e^{i\omega t} \\ B_0(x,t) &= (\tfrac{n_0}{c}E_{f,0}e^{ik_0 z} - \tfrac{n_0}{c}E_{b,0}e^{-ik_0 z})e^{i\omega t} \end{aligned} \tag{3.7}$$

Based on the boundary conditions, tangential part of E is equal across the interface and normal component of B is equal across the interface, we can write the transfer matrix format of the boundary condition:

$$\begin{pmatrix} 1 & 1 \\ n_0 & -n_0 \end{pmatrix}\begin{pmatrix} E_{f,0} \\ E_{b,0} \end{pmatrix} = \begin{pmatrix} 1 & 1 \\ n_1 & -n_1 \end{pmatrix}\begin{pmatrix} E_{f,1} \\ E_{b,1} \end{pmatrix}$$
$$\begin{pmatrix} E_{f,0} \\ E_{b,0} \end{pmatrix} = \frac{1}{2}\begin{pmatrix} \frac{n_0+n_1}{n_0} & \frac{n_0-n_1}{n_0} \\ \frac{n_0-n_1}{n_0} & \frac{n_0+n_1}{n_0} \end{pmatrix}\begin{pmatrix} E_{f,1} \\ E_{b,1} \end{pmatrix} = P_{01}\begin{pmatrix} E_{f,1} \\ E_{b,1} \end{pmatrix} \tag{3.8}$$

where P_{01} is the interface matrix, $E_{f,i}$ and $E_{b,i}$ are the forward and backward propagating waves at the interface, as shown in Figure 3.4. We can also write the wave propagation phase change and loss in medium 1 in the matrix format:

$$\begin{pmatrix} E_{f,1} \\ E_{b,1} \end{pmatrix} = \begin{pmatrix} e^{-ik_1 d_1} & 0 \\ 0 & e^{+ik_1 d_1} \end{pmatrix}\begin{pmatrix} E'_{f,1} \\ E'_{b,1} \end{pmatrix} = D_1\begin{pmatrix} E'_{f,1} \\ E'_{b,1} \end{pmatrix} \tag{3.9}$$

where D_1 is the dephasing matrix. Following similar approach in other layers, the whole transfer matrix describing the wave propagation in the structure of Figure 3.4 is:

$$\begin{pmatrix} E_{f,0} \\ E_{b,0} \end{pmatrix} = P_{01}D_1P_{12}D_2P_{23}D_3 \dots D_nP_{n,n+1}\begin{pmatrix} E_{f,n+1} \\ E_{b,n+1} \end{pmatrix} = s\begin{pmatrix} E_{f,n+1} \\ E_{b,n+1} \end{pmatrix} \quad (3.10)$$

The reflectivity of the whole system is given as:

$$R = \left|\frac{E_r}{E_i}\right|^2 = \left|\frac{E_{b,0}}{E_{f,0}}\right|^2 = \left|\frac{S_{21}}{S_{11}}\right|^2 \quad (3.11)$$

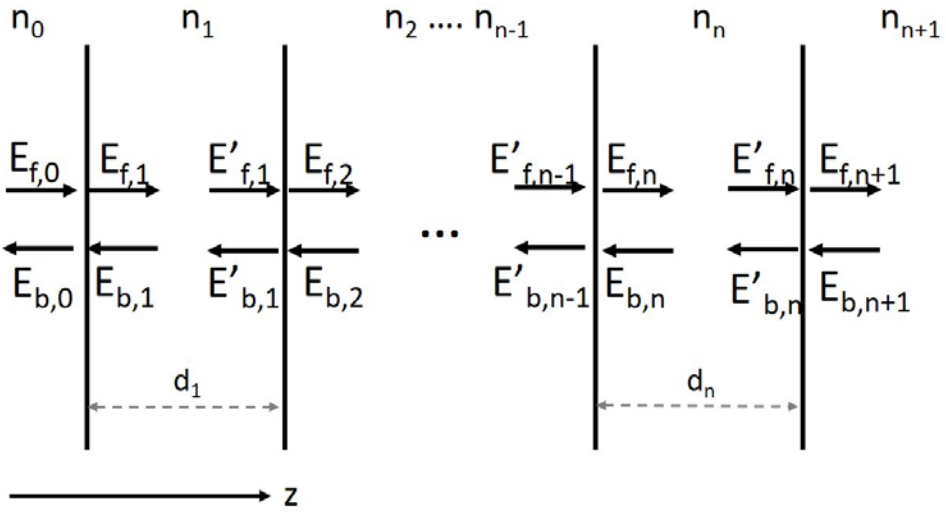

Figure 3.4: Plane wave model of light travelling in multilayer anti-reflection coating.

For mid-IR wavelength at 5~7 μm range, Aluminum oxide (Al_2O_3) is a good candidate as it is transparent in this region and has index approximate to 1.8, but it starts absorbing above 7 μm. In 10~12 μm wavelength range, one layer of Yttrium oxide (Y_2O_3) is one option but is not good enough to achieve low reflectivity. A two layer AR coating with the index of one material larger than 1.8 and the index of the other material smaller than 1.8 can be a good choice. The thickness of each layer can be determined based on the transfer matrix approach discussed above. In this thesis, we used a combination of Yttrium fluoride (YF_3) and Zinc selenide (ZnSe). Figure 3.5(a) shows first layer YF_3 thickness and second layer ZnSe thickness as a function of different wavelength when the reflectivity is

zero. Figure 3.5(b) depicts reflectivity percentage contour plot as a function of two layers' thickness, to reach 0.1% reflectivity, a precise thickness control of ±30 nm is required.

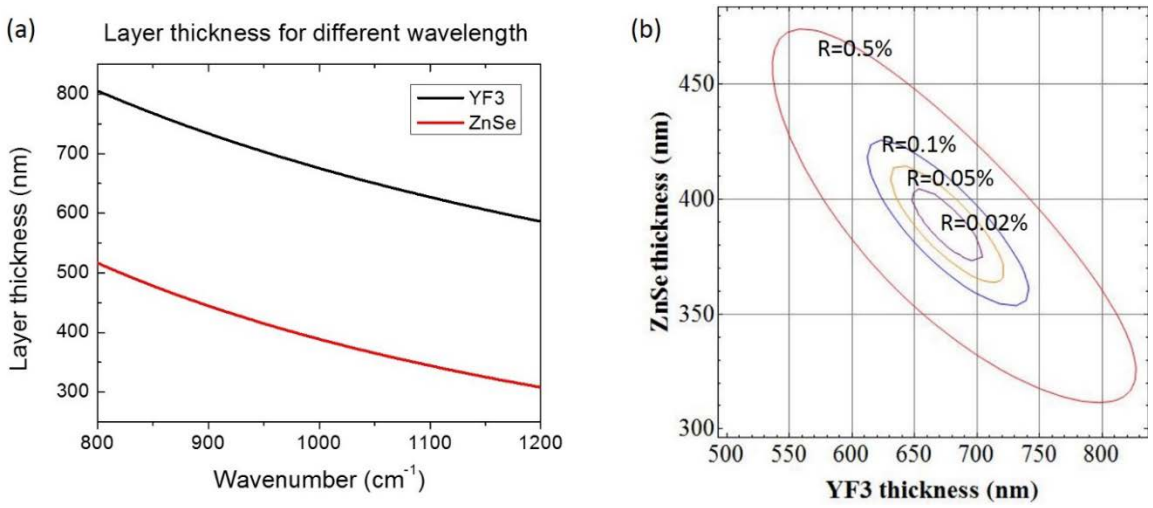

Figure 3.5: (a) YF_3 and ZnSe layer thickness for different wavelength in the range of 800 cm^{-1} to 1200 cm^{-1} for zero reflectivity. (b) Reflectivity of the two layer AR coating as a function of ZnSe and YF_3 thickness at 10 μm. The red, blue, orange, and purple contour lines represent reflectivity of 0.5%, 0.1%, 0.05%, and 0.02% respectively. A precise control of the thickness need to be ±30 nm for YF_3 and ±14 nm for ZnSe to reach 0.1% reflectivity.

For a two-layer AR coating in the mid-infrared range, the smaller index material could be YF_3, BaF_2, CaF_2 and so on, and the higher index material could be ZnSe, ZnS, Ge, Si and so on. The rule is to choose the materials that are transparent in the desired wavelength range and have good adhesion with device facet. Also, it is better to choose two materials with a close index for a two-layer coating. Take the combination of CaF_2 and Ge as an example, since index of Ge is around 4, much higher than 1.8, thickness control of Ge will be very critical. More advanced design of AR coating with multiple layers could be implemented if broader bandwidth is desired.

Chapter 4: Broadly tunable external cavity terahertz source

4.1 How to develop a broadly tunable room temperature terahertz

Broadly tunable sources are highly desired for spectroscopy, imaging, and many other applications. Currently broadly tunable sources in mid-infrared wavelength range are commercially available and widely used. This chapter focus on demonstrating a broadly tunable source in 1 to 6 THz frequency range. With all the pioneers' efforts in DFG THz generation and my previous introduction of the history and device concept of THz DFG-QCLs, we are ready to build a broadly tunable narrow linewidth THz source. THz DFG-QCL sources can principally be widely tunable since a relatively small change in the mid-IR pump frequency (ω_1 and ω_2) will translate into a large change in the THz output ($\omega_{THz} = \omega_1 - \omega_{2)}$. Then the target of tuning THz frequency becomes to tune two mid-IR pump frequencies (ω_1 and ω_2). Principally, one can tune the emitted THz frequency by fixing one mid-IR pump frequency and tune the other mid-IR pump frequency, or one can tune both mid-IR pump frequencies. One way is to fabricate dual-period DFB gratings in the waveguide to select two mid-IR frequencies, by changing the temperature of the device so as to change the effective index of two DFB gratings separately, the separation of two mid-IR frequencies corresponding to the THz frequency could be tuned. The THz tuning range for a single device based on this approach is limited to 0.6~1.5 THz [27,28]. An array of these dual-period DFB QCLs with different grating periods can achieve broader THz

A portion of this work has been published in Y. Jiang, K. Vijayraghavan, S. Jung, F. Demmerle, G. Boehm, M. C. Amann, and M. A. Belkin, "External cavity terahertz quantum cascade laser sources based on intra-cavity frequency mixing with 1.2–5.9 THz tuning range," *J. Opt.* **16** (9), 094002 (2014). Y. J. performed external cavity system design, device processing, all measurements and data analysis. K.V designed the wafer growth. S. Jung helped with device processing. F. D., G. B. performed wafer growth, M.C.A supervised the wafer growth group, M.A.B supervised the whole project.

tuning range [29].

The approach I discuss in this chapter is based on an external cavity (EC) system, it is operated by fixing one mid-IR pump frequency (ω_1) with a monolithic DFB grating etched in the QCL waveguide while tuning the other mid-IR pump frequency (ω_2) with an external diffraction grating in a Littrow-type external cavity configuration as shown schematically in Figure 4.1. Terahertz radiation at frequency $\omega_{THz} = \omega_1 - \omega_2$ is emitted into the substrate based on a Cherenkov phase matching scheme. In the first demonstration of EC THz DFG-QCL system, record tuning range from 1.7 THz to 5.25 THz with a peak power output varying between 5-40 μW for different THz frequencies was achieved at room temperature in a single device, such extreme wide tuning range can span multiple octaves in THz. After applying AR coating on the back facet of DFG-QCL, even larger THz tuning from 1.2 to 5.9 THz was demonstrated.

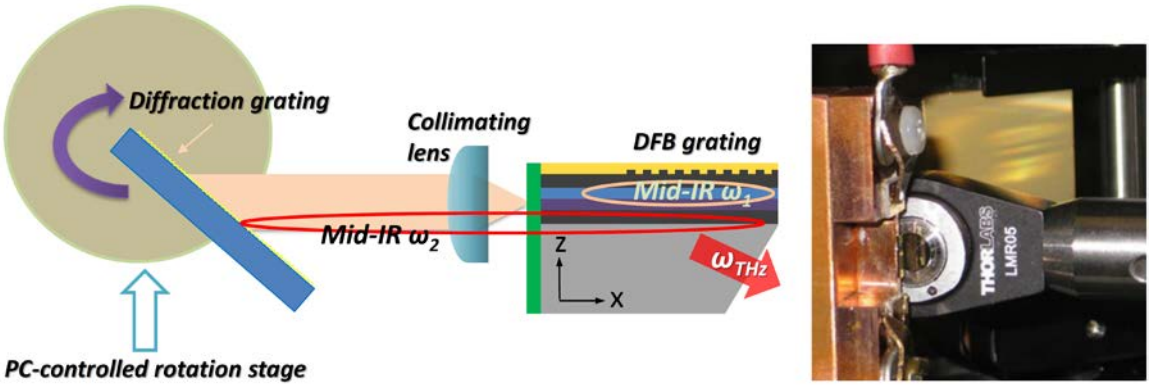

Figure 4.1: Schematics of the external cavity (EC) system setup (left) used in the experiments and the actual system set-up (right).

4.2 Laser chip and external cavity system design

Optical components used in the EC system (shown in Figure 4.1) include an aspheric AR coated collimating lens with focal length of 1.87 mm and a numerical aperture

of 0.85 (LightPath Technologies), a 150 grooves/mm gold diffraction grating (Optometrics Corporation model ML-303), and a computer-controlled Newport rotation stage. Both mid-IR and THz emission were collected from the front facets of QCL chips.

The waveguide core of the devices contains two stacks of bound-to-continuum heterogeneous active regions designed to have giant intersubband nonlinearity $\chi^{(2)}$ for THz DFG. Devices were grown by the molecular beam epitaxy on a 350-μm-thick semi-insulating (SI) InP substrate. Wafers were fabricated into deep-etched 22-μm-wide Fabry-Perot and DFB ridge waveguide devices using dry etching process, followed by a 400-nm-thick silicon nitride film deposition for sidewall insulation and the formation of metal contacts with a layer of Ti/Au (10nm/600nm). A side contact current extraction scheme was used due to the non-conductive nature of the semi-insulating substrate. First-order 140-nm-deep surface Bragg gratings with a 50% duty cycle and uniform grating period were fabricated into the top most waveguide layer using electron beam lithography, followed by reactive ion etching and overlaying it with the top-contact metal. Devices were then mounted epi-side up on copper blocks. A two-layer mid-IR AR coating made of a 650-nm-thick layer of YF_3 followed by 360-nm-thick layer of ZnSe was deposited by electron beam evaporation on the laser back facet.

The grating coupling coefficient was calculated to be $\kappa \approx 35+7i$ cm^{-1} using COMSOL Multiphysics simulations. Due to gain competition in our lasers, carefully selection of DFB grating coupling strength (κL) need to be stressed to balance two mid-IR pump modes. To control the coupling strength κL, either we can control the etching depth of the DFB grating to control κ, or we can control the length L of the DFB grating. For our external cavity system with the above choices of lens and diffraction grating, the DFB

grating coupling strength need to be around κL~4 to get the optimal balancing performance.

In order to check the performance of AR coating and have an estimation of the reflectivity of the external cavity system, we put a Fabry-Perot device with the back facet AR coated in the external cavity system for tuning. Figure 4.2(a) shows the light output-current (L-I) and current-voltage (I-V) characteristics of a 2.1-mm-long Fabry-Perot device before and after AR coating was applied to the back facet. Given the calculated waveguide loss 10 cm^{-1} and mirror loss of 6 cm^{-1} for the device with uncoated facets and assuming the

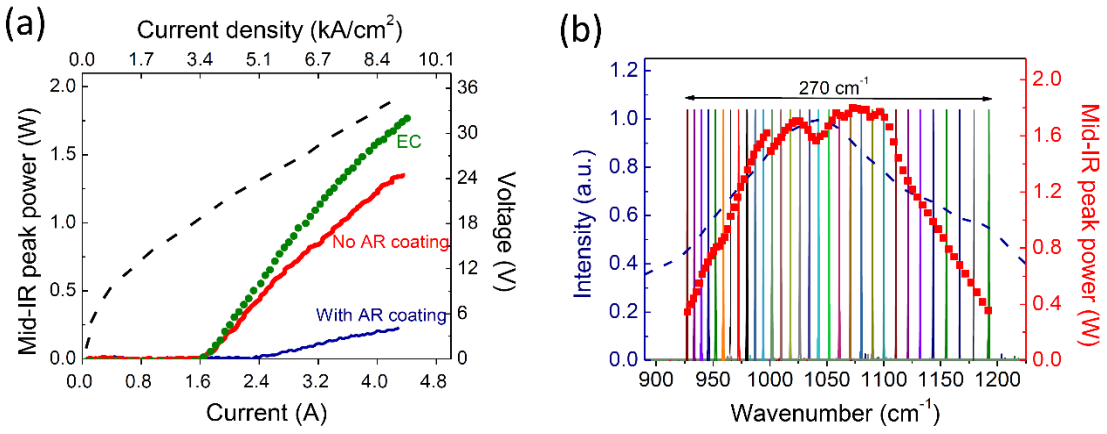

Figure 4.2: (a) Light output-current characteristic of the Fabry-Perot ridge-waveguide device before (thick red line) and after (thin blue line) back facet AR coating. Also shown is the Light output-current characteristic (circles) of the same AR-coated device placed into the EC setup with external grating tuned to operate at 1080 cm^{-1}, close to the laser gain peak. The current-voltage characteristic (dashed line) of the device is also shown. (b) Electroluminescence spectrum (dashed line) of the laser material at current density of 7.5 kA/cm^2 and emission spectra of the device at different EC grating position (peaks of different colors). Also shown is the peak mid-IR power output of the device for different EC grating positions (red squares). The laser was operated in pulsed mode at room temperature with a pump current density of 8.0 kA/cm^2.

laser gain scales linearly with current density, we calculate the AR-coated facet in our device has approximately 1.5% facet reflectivity around the gain peak at approximately 1080 cm^{-1}. Figure 4.2(c) also provides the L-I for the same AR-coated device integrated into the EC setup with external grating tuned to lase at the gain peak 1080 cm^{-1}. The threshold current density in this case is nearly the same as that for the Fabry-Perot device with uncoated facets, indicating that the optical feedback of the EC system results in an effective reflectivity of approximately 30%.

The mid-IR gain spectrum of our DFG-QCL chips was initially determined by electroluminescence measurements and then by EC mid-IR tuning of Fabry-Perot devices with AR-coated back facets. Figure 4.2(b) shows the electroluminescence spectrum from a structure fabricated into a wet etched cylindrical mesa, as well as the mid-IR tuning performance of a 2.1-mm-long, back facet AR coated Fabry-Perot laser in the external cavity system. Mid-IR tuning from 927 cm^{-1} to 1197 cm^{-1} has been achieved, indicates a gain bandwidth of 8.1 THz, corresponding to 25% of the center frequency.

4.3 EC THz DFG-QCL system performance

In QCLs the gain recovery process is faster than carrier diffusion and spatial hole burning of the laser gain is significant, favoring multimode operation for both longitudinal and transverse modes [62]. The requirement of strong modal overlap for efficient THz DFG dictates that the two mid-IR pumps need to operate in TM_{00} waveguide modes which have nearly identical intensity profiles for both ω_1 and ω_2 frequencies. The tunable THz DFG-QCL system is created by placing a DFB DFG-QCL device in the EC system, so that two mid-IR pumps – one at frequency ω_1, determined by the DFB grating, and the other at frequency ω_2, determined by the position of the external diffraction grating – can achieve lasing at similar threshold current densities. The transverse TM_{00} pump mode is enforced

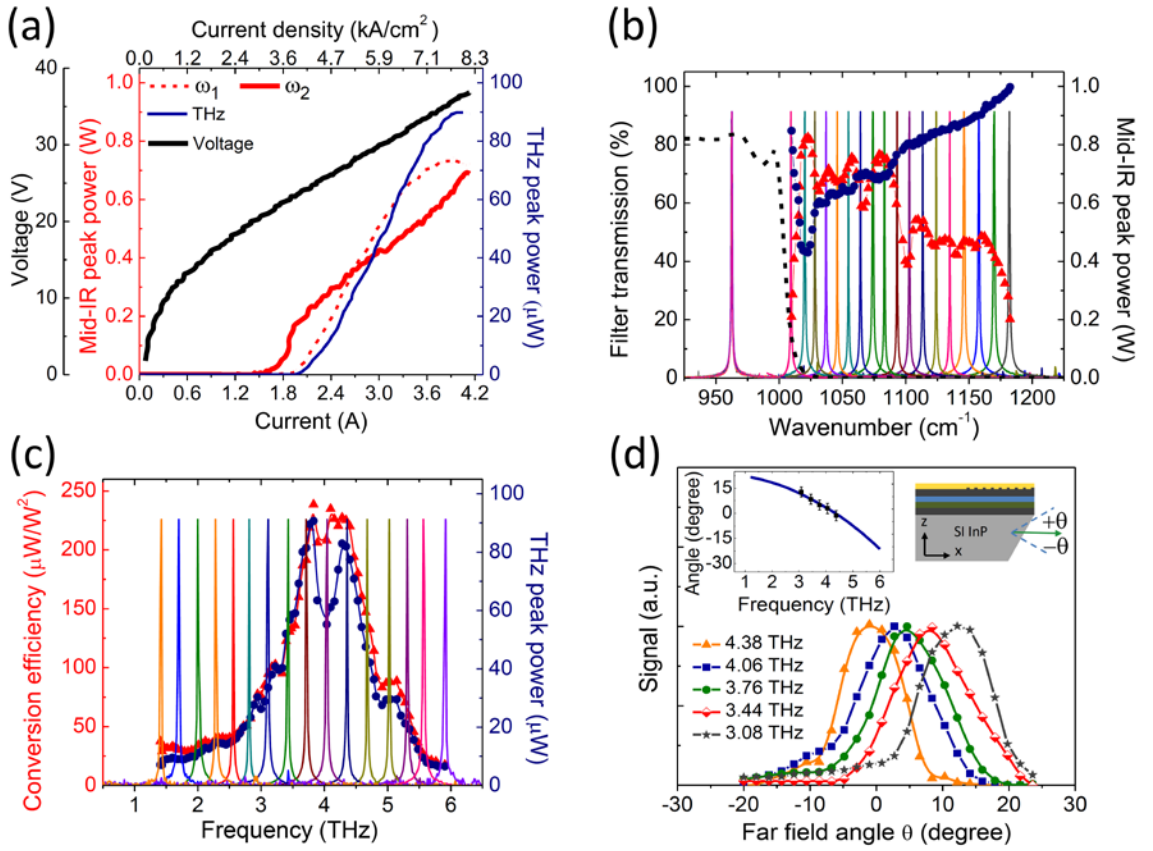

Figure 4.3: (a) Light output-current characteristics of the mid-IR and THz emission (see key) of the THz EC system with a Cherenkov DFG-QCL on semi-insulating InP substrate as described in the text. Data is shown for operation at 3.8 THz. Also shown is the current-voltage characteristic of the device. (b) Mid-IR emission spectra and power output of the two mid-IR pumps for the EC THz DFG-QCL system described in (a) at different EC diffraction grating positions taken at a current density of 8.0 kA/cm^2. Also shown is the mid-IR power for ω_1 (blue) and ω_2 (red) pumps as a function of ω_2 pump wavenumber. The dashed line shows the transmission spectrum of the mid-IR long-pass filter used for power measurements. (c) THz emission spectra of the EC THz DFG-QCL system taken at a current density of 8.0 kA/cm^2. Also plotted are the THz peak power (blue and right axis) and mid-IR-to-THz conversion efficiency (red and left axis) as a function of THz frequency. (d) Vertical far-field THz emission profile of the EC THz DFG-QCL system described in (a-c) at

3.08 THz, 3.44 THz, 3.76 THz, 4.06 THz, and 4.38 THz. Vertical angle θ is defined relative to the direction normal to the laser facet as shown in the top-right inset. Top-left inset shows calculated dependence of the Cherenkov emission angle in a SI InP substrate as a function of THz frequency (solid line) and the Cherenkov emission angles in the substrate deduced from experimental measurements of the far field at different THz frequencies (circles).

by using the DFB grating designed for TM_{00} mode at ω_1 and by natural feedback discrimination between TM_{00} and higher-order modes in the EC setup for ω_2 pump.

Experimental results for an EC THz DFG-QCL system with a 2.3-mm-long, back facet AR-coated ridge waveguide THz DFG-QCL that contains a 1.6-mm-long DFB grating section is shown in Figure 4.3. The DFB grating was designed to fix ω_1 pump at 963 cm^{-1}, away from the gain peak. The substrate front facet of the device was polished at a 30˚ angle to avoid total internal reflection of the Cherenkov THz emission and allow for THz extraction in the forward direction. Figure 4.3(a) displays the L-I characteristics for the ω_1 and ω_2 pumps for the case when the EC grating is positioned to select ω_2 pump frequency at approximately 1090 cm^{-1} (corresponding to a difference-frequency of approximately 127 cm^{-1} or 3.8 THz) close to device gain peak. Also shown is the L-I characteristic of the THz emission for the same EC grating configuration. Figure 4.3(b) shows the emission spectra and power output of the two mid-IR pumps at different EC grating positions at a current density of 8.0 kA/cm^2 through the device. A long pass interference filter was used to spectrally separate the two mid-IR pumps for the measurements. The mid-IR power was corrected for the filter transmission shown in Figure 4.3(b). The spectral data shows that, as expected, the DFB pump frequency ω_1 stays fixed at 963 cm^{-1} while the EC pump frequency ω_2 is tuned continuously from 1009 cm^{-1} to 1182 cm^{-1}, resulting in the available difference-frequency tuning from 1.4 THz to 5.9 THz. Due

to gain competition, the mid-IR emission switches from dual-frequency (ω_1 and ω_2) to single-frequency (ω_1) output as the EC feedback frequency ω_2 is tuned towards the DFB frequency ω_1 as shown in Figure 4.3(b), and the ω_1 pump power increases somewhat as the ω_2 pump power drops. Gain competition between the two mid-IR pumps, not fully suppressed by spatial hole burning [62], is likely to be the mechanism behind this effect.

To check whether there is mode competition or not, we investigated the dynamic performance of this two mode system. we took the time resolved spectra during short time windows at various instants during the 50 ns pulse, the optical signal was measured with a room temperature fast MCT detector with a sub-nanosecond time constant was fed into a boxcar integrator to select a specific time window during the laser pulse [61]. Spectra were taken with 2 ns intervals with a 2 ns long gate. Figure 4.4 is the dynamic performance, we found that away from the center of the gain, EC mode lased after DFB mode, and the

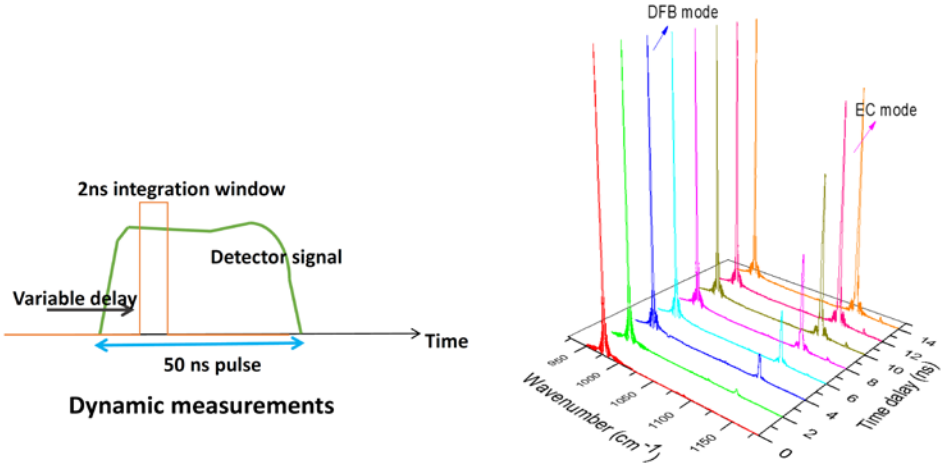

Figure 4.4: Dynamic performance of two mid-IR pumps. (a) Integration scan over a single pulse, measurement method. (b) Lasing spectra of two modes in different delay times.

intensity of EC modes gradually increased. After 10 ns, the EC mode became stable. This is caused by different round trip times between the DFB mode and EC modes, for DFB

mode, it took 20 ps to recycle in a 2.3-mm long device, for EC mode, it took 300ps for a 4-cm long EC system.

The THz emission spectra and peak power for different EC grating positions taken at a current density of 8.0 kA/cm^2 through the device are displayed in Figure 4.3(c). Also shown is mid-IR-to-THz nonlinear conversion efficiency, defined as the ratio of the measured THz peak power to the product of the two mid-IR pump powers, at a current density of 8.0 kA/cm^2. A THz peak power of 90 μW and mid-IR-to-THz conversion efficiency of nearly 250 μW/W^2 were observed at 3.8 THz. The conversion efficiency in Figure 4.3(c) maximizes in the 3.7-4.5 THz range of frequencies and falls off at both high- and low-frequency ends of the tuning curves. On the high-frequency end, efficiency of THz generation is limited by the onset of high optical losses in InGaAs/AlInAs/InP materials due to tails of LO-phonon absorption bands (Reststrahlen band). On the low-frequency end, THz generation efficiency is principally limited by high free carrier absorption in the QCL waveguide and the $(\omega_{THz})^2$ dependence of the DFG efficiency [62]. Additional factors include spectral dependence of intersubband optical nonlinearity and residual absorption in SI InP substrate through which THz radiation is extracted. Detailed theoretical analysis of spectral dependence of mid-IR-to-THz conversion efficiency in THz DFG-QCLs will be presented in Chapter 5.

The far field THz emission profile of a typical device on a SI InP substrate is shown in Figure 4.3(d). The data was obtained at selected THz emission frequencies by placing the bolometer 15 cm away from the laser facet and monitoring the received THz power while sweeping the bolometer in the x-z plane, see Figure 4.1 for the coordinate system. Significant beam steering in the vertical direction is observed.

To explain the origin of beam steering, we need to consider the angle of Cherenkov DFG emission into the substrate which is given as,

$$\theta_C = \cos^{-1}\left(\beta_{nl}/k_{THz}\right) \tag{4.1}$$

Here $k_{THz} = n_{THz}^{sub}\omega_{THz}/c$ is the propagation constant of the THz wave in the substrate, with n_{THz}^{sub} being the refractive index of the substrate, and β_{nl} is the propagation constant of the nonlinear polarization wave at the terahertz frequency in the laser waveguide. The right-going nonlinear polarization wave (cf. Figure 4.1) can be written as

$$P_{\omega_{THz}}^{(2)}(\mathrm{z},\mathrm{t}) \approx \varepsilon_0 \chi_{zzz}^{(2)} E_{2z} E_{1z}^{*} e^{j\left((\omega_2-\omega_1)t-(\beta_2-\beta_1)x\right)} \tag{4.2}$$

where $\chi_{zzz}^{(2)}$ is the intersubband nonlinear susceptibility for THz DFG in the laser active region, E_{1z} and E_{2z} are the z-components of the electric fields of TM-polarized mid-IR pumps, β_1 and β_2 are the propagation constants of the mid-IR pumps, and we assume the z-axis to be normal to the heterostructures layers and x-axis to be directed along the waveguide as shown in Figure 4.1. From Eq. (4.2) we see that $\beta_{nl}=\beta_2-\beta_1$ and its value can be written as [63]:

$$\beta_{nl} = \beta_2 - \beta_1 \approx \frac{n_g \omega_{THz}}{c} \tag{4.3}$$

where $\omega_{THz} = \omega_2 - \omega_1$ and $n_g(\omega) = n_{eff}(\omega) - \lambda \cdot dn_{eff}/d\lambda$ is the group effective refractive index for mid-IR pumps. The expression for the Cherenkov emission angle in Eq. (4.1) then becomes

$$\theta_C = \cos^{-1}\left(n_g / n_{THz}^{sub}\right) \tag{4.4}$$

For mid-IR QCLs with a broad gain spectrum, similar to the devices reported here, the value of n_g is nearly constant over the gain bandwidth [64,65], and for our devices $n_g \approx 3.37$. The value of n_{THz}^{sub} for InP substrate, on the other hand, change significantly from n_{THz}^{sub} = 3.5 at 1 THz to 3.8 at 6 THz [66] as shown in Figure 4.5(a). According to Eq. (4.4) such a change leads to over a 10 degree change in θ_C in the substrate and translates into nearly

a 40 degree change in THz far field emission direction in 1-6 THz range for a device with a 30-degree-polished substrate. The inset in Figure 4.3(d) compares Cherenkov emission calculated with Eq. (4) using InP THz refractive index values from Ref. [66] with the values of θ_C deduced from experimentally-measured far-field emission profiles. The experimental data is in excellent agreement with theory.

4.4 EC THz DFG-QCL system with suppressed beam steering

As we see in section 4.3, THz beam steering is significant for EC THz DFG-QCL system based on SI-InP substrate. To suppress THz beam steering in our system, the InP substrate of devices could be replaced with a high-resistivity silicon substrate. Due to the lack of strong optical phonon absorption, silicon has significantly smaller refractive index dispersion in the 1-6 THz range compared to InP, see Figure 4.5.

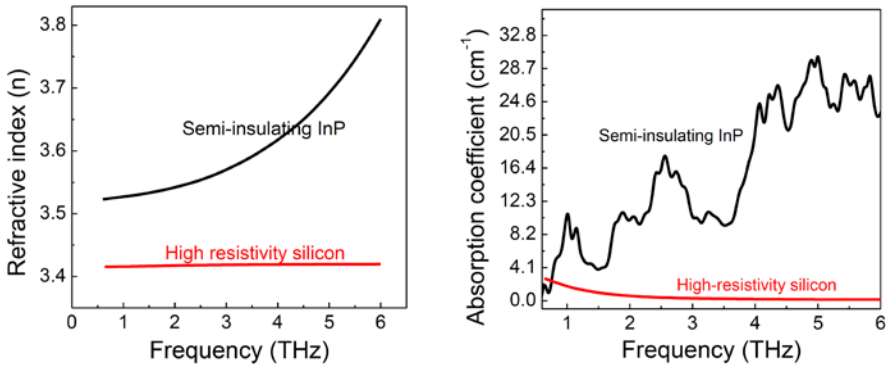

Figure 4.5: (a) Refractive index (dashed red line and right axis) and absorption coefficient (solid black line and left axis) of SI InP as a function of THz frequency; the absorption coefficient was measured experimentally using SI InP device substrates. (b) Refractive index (dashed red line and right axis) and absorption coefficient (solid black line and left axis) of high-resistivity silicon as a function of THz frequency. The data is taken from Ref. 66.

To replace SI InP substate, the 350-μm-thick SI InP substrate in some devices was thinned down to 100~120 μm thickness and the devices were bonded, substrate-down, to

a 1-mm-thick high-resistivity silicon substrate using a 500-nm-thick adhesion layer of SU-8 photoresist. The assembly was then cured at 65 ˚C for 30 minutes, then at 95 ˚C for 30 minutes and finally at 140 ˚C for 10 minutes under the pressure of 4 MPa. The back facet of the silicon substrate was aligned with the laser back facet and the front side was polished to allow for THz Cherenkov wave emission in forward direction. The schematic of our design structure is shown in Figure 4.6(a) and the scanning electron microscope images of the devices and the InP/SU-8/silicon bond interface are shown in Figure 4.6(b).

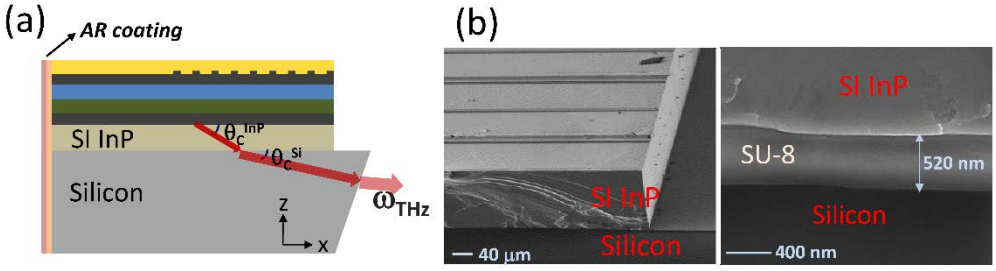

Figure 4.6: (a) Schematic of the device bonded to a high-resistivity silicon substrate. (b) Scanning electron microscope images of the laser bar bonded to a high-resistivity silicon substrate (left panel) and the InP/SU-8/silicon interface. SU-8 bonding layer was measured to be 520-nm-thick.

The angle of THz emission in the silicon substrate can be calculated as:

$$n_g = n_{THz}^{InP} \cos\theta_C^{InP} = n_{THz}^{Si} \cos\theta_C^{Si} \tag{3.5}$$

where n_{THz}^{InP} and θ_C^{InP} (n_{THz}^{Si} and θ_C^{Si}) are the refractive index of and the Cherenkov THz emission angle in InP (silicon), respectively. This small refractive index dispersion ensures a constant Cherenkov emission angle of approximately 10 degrees into the silicon substrate over the entire 1 - 6 THz range. A 14º silicon substrate polishing angle will then produce THz out-coupling in forward direction.

Ideally, one would like to use thinner SU8 bonding layer as well as thinner remaining SI InP part, both of which are critical parameters in determining the out-coupled THz power. However, devices bonded on silicon substrates with ~200-300-nm-thick layer

of SU-8 showed numerous bonding imperfections and polishing InP substrate with thickness thinner than 100 μm is mechanically challenging. We plot the effect of these parameters in Figure 4.7assuming that the mid-IR pump powers stays unchanged as devices are bonded to silicon. For the case of our devices, bonded with 500-nm-thick SU-8 layer and having 120-μm-thick SI InP substrate remaining, the mid-IR-to-THz conversion efficiency is expected to improve by approximately a factor of 1.3 at 3.8 THz.

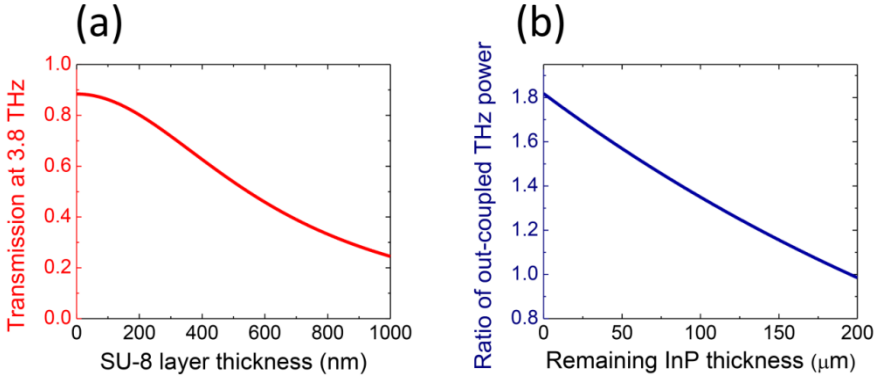

Figure 4.7: (a) Power transmission coefficient of TM polarized Cherenkov THz wave from SI InP substrate to silicon substrate as a function of SU-8 bonding layer thickness. The data is shown for the case of 3.8 THz emission. (b) Expected THz power improvement factor for a device bonded to a 1-mm-thick silicon substrate compared to an identical device on 350-μm-thick SI InP substrate. Here we assume a 2.3-mm-long device bonded with 500-nm-thick SU-8 layer and plot the improvement factor as a function of remaining InP substrate thickness of the silicon-bonded device.

The performance of a 2.3-mm-long, back facet AR coated ridge waveguide device is detailed in Figure 4.8. The device has a 1.5-mm-long surface grating section fabricated on top of the waveguide and was bonded to a 2.8-mm-long, 1-mm-thick silicon substrate with 120-μm-thick remaining InP substrate. Similar to the devices on SI InP substrates described in the previous section, the DFB grating for this device was designed to fix ω_1 at 963 cm^{-1}. The device provided smaller mid-IR and THz power output, compared to the

device on SI InP substrate reported in Figure 4.3, possibly due to excessive heating. The heating problem may, in principle, be solved by mounting devices epi-side down on copper blocks. External cavity mode ω_2 could be tuned from 1004 cm^{-1} to 1185 cm^{-1}. THz performance of the device at a current density of 7.5 kA/cm^2 is shown in Figure 4.8(a). The THz emission could be tuned from 1.2 THz to 5.9 THz. We note that, while we could tune ω_2 pump so as to produce difference frequency as high as 6.7 THz (222 cm^{-1}), we observed no detectable THz emission from his device at frequencies above approximately 5.9 THz. This is likely due to strong THz radiation absorption at the active region and the substrate by the tails of optical phonon absorption bands in InP, InGaAs and AlInAs materials.

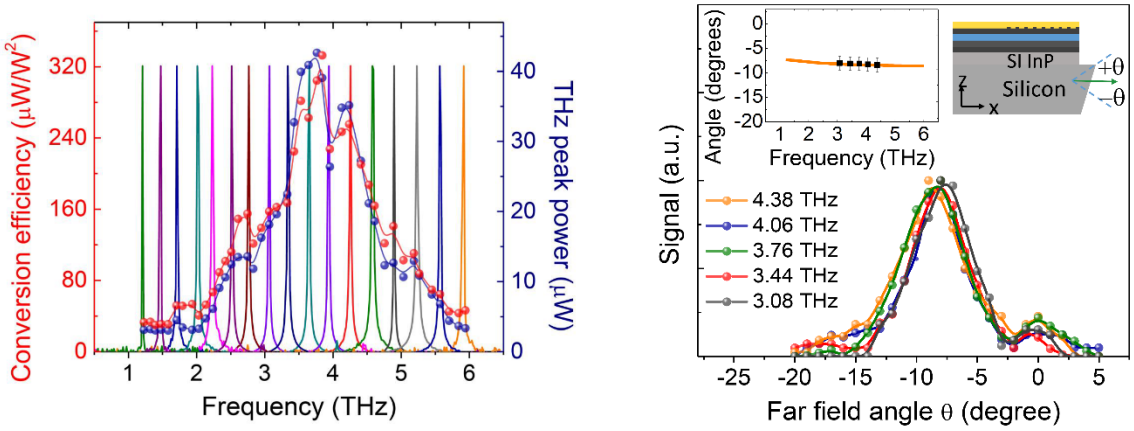

Figure 4.8: (a) THz emission spectra of the EC THz DFG-QCL system in taken at a current density of 7.5 kA/cm^2. Also plotted are the THz peak power (blue and right axis) and mid-IR-to-THz conversion efficiency (red and left axis) as a function of THz frequency. (b) Vertical far-field THz emission profile of the EC THz DFG-QCL system described in (a-c) at 3.08 THz, 3.44 THz, 3.76 THz, 4.06 THz, and 4.38 THz. Vertical angle θ is defined relative to the direction normal to the laser facet as shown in the top-right inset. Top-left inset shows calculated dependence of the Cherenkov emission angle in a silicon substrate as a function of THz frequency (solid line) and the Cherenkov emission angles in the substrate deduced from experimental measurements of the far field at different THz frequencies (circles)

Figure 4.8(a) also shows terahertz power output and mid-IR-to-THz conversion efficiency at different THz frequencies. A maximum mid-IR-to-THz conversion efficiency of 0.35 mW/W^2 was achieved at 3.8 THz, which represent a factor of 1.4 times improvement over the reference device on SI InP substrate, see Figure 4.7(c). The experimental improvement factor is close to that predicted in Figure 4.7(b). Far field profiles in the vertical direction plane (cf. Figure 4.8(b)) for this device at selected THz frequencies are shown in Figure 4.8(b). Virtually no beam steering is observed in close agreement with theoretical prediction shown in the inset to Figure 4.8(b). Overall, theoretical analysis predicts only a 1.2˚ change in the far field profile peak for the devices bounded to high-resistivity silicon as the emission is tuned from 1 THz to 6 THz.

This substrate transfer scheme still have 100 μm thick InP remaining, which still have quite strong THz absorption. Ideally, we could replace the entire InP substrate by etching it away [32], similar to heterogeneous integration of III-V active material to pre-patterned silicon-on-insulator waveguides for telecommunication wavelength range [67]. Figure 4.9 shows a device transfer and print process. After device fabrication, the processed wafer was first coated with SU-8 epoxy resin (MicroChem Corp.) and 50-μm-wide 8-μm-tall supporting elements next to each ridge were defined lithographically in order to prevent epi-layer damage during the bonding process. The wafer was then attached to a glass slide with laser ridges facing the glass using crystal glue (Crystalbond 509). The InP substrate was then selectively removed using an HClbased wet etchant with the InGaAs current injection layer used as an etch stop. The exposed surface of the current injection layer was then bonded to a 1-mm-thick FZ HR Si wafer coated with a 100-nm-thick SU-8 layer. The bonding was performed in the AML wafer bonding machine at a pressure of 1 MPa and a temperature of 180°C for 15 min. Under these conditions, the SU-8 layer was cured,

leaving a strong permanent bond. Finally, the glass slide was removed by dissolving the crystal glue with acetone, and the hybrid QCL-on-Si wafer was diced into laser bars using a dicing saw. Devices based on this scheme have demonstrated 6 to 7 times higher THz power output compared to identical devices on InP substrates, as listed in the table in Figure 4.9.

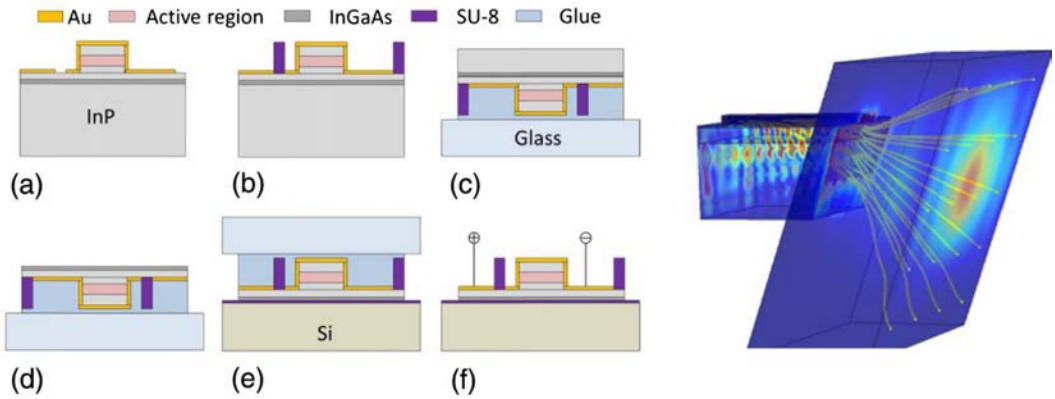

Device	$\eta_{slope\text{-}THz}$ (μW/A)	THz Power (μW)	η_{conv} (mW/W²)
InP 1	6.9	35.2	0.13
InP 2	7.8	26.5	0.05
Si 1	54.3	123.3	0.79
Si 2	44.4	113.8	0.37

Figure 4.9: Epi structure transfer and print process [32]. (a) Fully processed QCL on InP. (b) SU-8 supporting elements are formed. (c) Devices with the SU-8 supporting elements are bonded on a piece of a glass slide with crystal glue. (d) The InP substrate is removed. (e) The QCL is bonded to a Si substrate with SU-8 adhesive. (f) The glass slide and crystal glue are removed. The table shows performance comparison between several devices.

4.5 Summary

We discussed the design and performance of a widely tunable, beam steering free, EC THz DFG-QCL system. We build a Littrow type external cavity DFG-THz system that generate spectral tunable THz frequency by fixing one mid-IR pump with an integrated DFB grating on top of the QCL structure and tuning the other mid-IR pump with an external grating. We demonstrated record THz frequency tuning bandwidth from 1.2 to 5.9 THz with an AR coated DFG-QCL device. Tunable THz sources based on Cherenkov DFG extraction through a semi-insulating InP substrate shows significant beam steering. We demonstrated that the beam steering can be suppressed and the mid-IR-to-THz conversion efficiency can be improved by bonding devices to high-resistivity silicon substrates that have virtually no refractive index dispersion and vanishingly-small THz loss in the entire 1-6 THz range.

Chapter 5: Spectroscopic study of terahertz generation in mid-infrared quantum cascade lasers

5.1 Introduction

In chapter 4, we demonstrated a broadly tunable EC THz DFG-QCL system by fixing one mid-IR pump with integrated DFB grating and tuning the other mid-IR pump with an external diffraction grating, terahertz generation in this system is produced via the nonlinear mixing of the two mid-IR pump fields generated in the QCL active region. The active region is designed to have resonant optical nonlinearity $\chi^{(2)}$ associated with transitions between the upper laser states and the manifold of the lower laser states as shown in Figure 5.1(a,b). Terahertz power output (W_{THz}) scales with the product of mid-IR pump powers (W_1 and W_2) and the square of the magnitude of $\chi^{(2)}$:

$$W_{THz} \propto \left|\chi^{(2)}\right|^2 W_1 W_2 \tag{5.1}$$

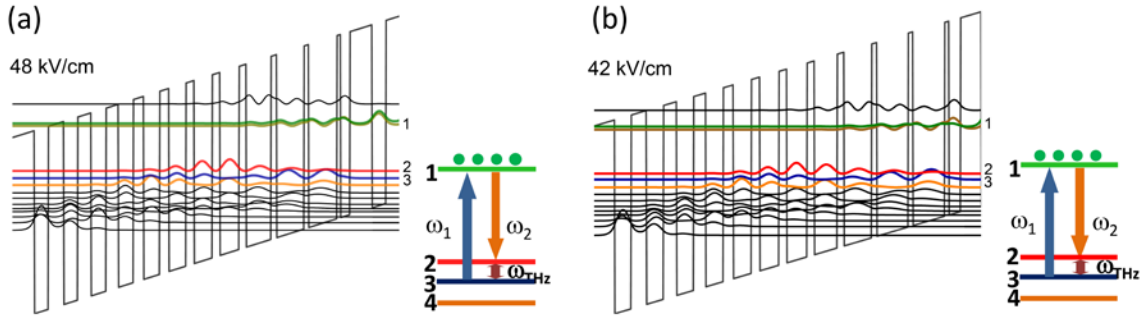

Figure 5.1: (a) Conduction band diagram of one period of λ=8.5 μm active region at 48 kV cm^{-1} bias field, close to the rollover point. Inset: schematic diagram showing the DFG process between the electron states in this structure. Transition dipole matrix elements and energy spacing between states 1, 2, and 3 are computed

A portion of this work has been published in Y. Jiang, K. Vijayraghavan, S. Jung, A. Jiang, J. H. Kim, F. Demmerle, G. Boehm, M. C. Amann, and M. A. Belkin, "Spectroscopic Study of Terahertz Generation in Mid-Infrared Quantum Cascade Lasers," *Sci. Rep.* **6**, 21169 (2016). Y. J. performed external cavity system design, device processing, all measurements and data analysis. K.V designed the wafer growth. K.V., S. J., A. J., J. H.K. helped with device processing. F. D., G. B. performed wafer growth, M.C.A supervised the wafer growth group, M.A.B supervised the whole project.

to be z_{12}=2.2 nm, z_{13}=1.9 nm, z_{23}=8.0 nm, E_{12}=135 meV, E_{13}=154 meV. (b) Conduction band diagram of one period of λ=9.5 μm active region at 42 kV cm^{-1} bias field, close to the rollover point. Inset: schematic diagram showing the DFG process between the electron states in this structure. Transition dipole matrix elements and energy spacing between states 1, 2, and 3 are computed to be: z_{12}=2.3 nm, z_{13}=2.2 nm, z_{23}=9.0 nm, E_{12}=121 meV, E_{13}=137 meV.

Referring to the energy state labelling shown in Figure 5.1 and keeping only resonant terms, the quantum mechanical expression for $\chi^{(2)}$ for THz DFG is given as:

$$\chi^{(2)}(\omega_1,\omega_2) \approx \Delta N_e \frac{e^3}{\hbar^2 \varepsilon_0} \frac{z_{12} z_{23} z_{31}}{(\omega_{THz} - \omega_{23} + i\Gamma_{23})} \times \left(\frac{1}{\omega_1 - \omega_{13} + i\Gamma_{31}} + \frac{1}{-\omega_2 + \omega_{12} + i\Gamma_{21}} \right) \qquad (5.2)$$

where ω_1 and ω_2 are the frequencies of mid-IR pumps, $\omega_{THz}=\omega_1-\omega_2$ is THz difference-frequency, ΔN_e is the population inversion density, n and n′ are the lower state levels (levels 2,3, and other lower laser levels shown in Figure 5.1), ez_{ij}, ω_{ij}, and Γ_{ij} are the transition dipole moments, transition frequency, and transition linewidth factor between states i and j. Equation (5.2) shows that $\chi^{(2)}$ has a strong 2-dimensional (2D) dependence on the mid-IR pump frequencies. However, no work has been performed so far to experimentally measure the dependence of $\chi^{(2)}$ on ω_1 and ω_2 in THz DFG-QCLs. The linewidth factor Γ_{23} for THz transitions between the lower laser states has also not been experimentally quantified. Determining the linewidth factor Γ_{23} is critical for improving the modeling accuracy of $\chi^{(2)}$ and optical loss in the lower laser levels structure of QCLs. We note that it is nearly impossible to measure Γ_{23} using linear absorption techniques because both states 2 and 3 are designed to be quickly depopulated under QCL operating bias.

In this chapter, I will discuss how to accurately predict and maximize $\chi^{(2)}$ in the active region, which is critical for further advancement of THz DFG-QCL technology.

5.2 Two dimensional external cavity THz DFG-QCL system

As we can see from Eq. (5.2), nonlinearity $\chi^{(2)}$ depends on both ω_1 and ω_2, we use a dual-diffraction-grating external cavity (EC) setup that could tune both mid-IR pump frequency ω_1 and ω_2 instead of using the system in chapter 4 that fix ω_1 and only tune ω_2. We performed independent tuning of the two mid-IR pumps using a dual-diffraction-grating external cavity (EC) setup. The positions of the diffraction gratings were computer controlled. Our setup may be viewed as an extension of Littrow-type external cavity setup used for mid-IR QCLs. It is also similar to a dual-grating EC setup used previously for dual-color tuning of near-infrared diode lasers [56].

The dual-grating experimental setup is shown in Figure 5.2(a). Cherenkov THz DFG-QCL chips used in this chapter were identical to devices in chapter 4, except that no DFB gratings need to be defined in the waveguide. The back facets of the Cherenkov THz DFG-QCL chips are coated with a two-layer anti-reflection (AR) coating using YF_3 and ZnSe designed to have a minimum reflection around the middle of the gain bandwidth of the device. An AR-coated aspheric lens with focal length of 1.87 mm and numerical aperture of 0.85 is used to collimate the mid-IR emission from the back facet of the laser. The collimated mid-IR beam is then split by a 50/50 ZnSe beam splitter and directed to two diffraction gratings (gold coated, 150 grooves mm^{-1}) placed on two computer-controlled rotation stages. The gratings are used to provide frequency-tunable feedback for two mid-IR pump frequencies (ω_1 and ω_2) independently. Cherenkov THz DFG emission from the device was collected through a 30-degree polished device substrate facet. Selected mid-IR tuning spectra from the THz DFG-QCL in our EC setup are shown in Figure 5.2(b) for different grating positions. Corresponding selected THz emission spectra of the device are shown in Figure 5.2(c). For the 2D spectroscopy results presented below, the frequency

of mid-IR pump 1 (ω_1) was varied between 1091 cm^{-1} to 1151 cm^{-1} and the frequency of pump 2 (ω_2) was varied, independently, between 981 cm^{-1} to 1052 cm^{-1}. THz DFG frequency corresponds to the frequency separation between the two mid-IR pumps ($\omega_{THz}=\omega_1-\omega_2$) thus could be tuned from 1.17 THz (39 cm^{-1}) to 5.10 THz (170 cm^{-1}).

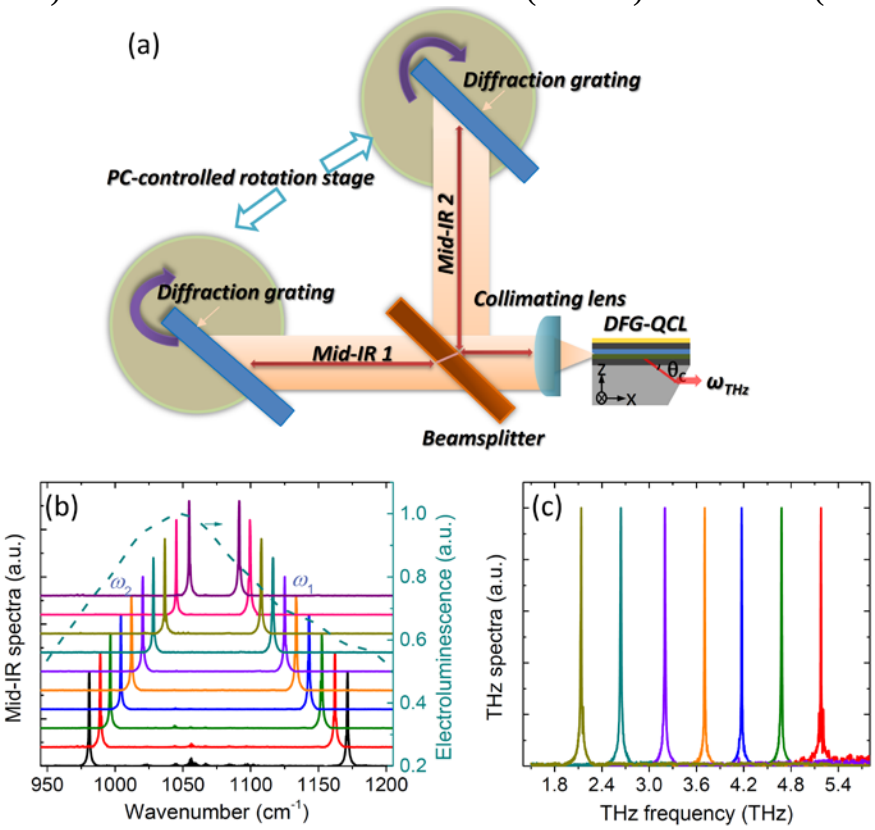

Figure 5.2: Details of the laser tuning setup. (a) Schematic of the dual-grating Littrow-type external cavity. (b) Mid-IR emission spectra of a THz DFG-QCL in the setup depicted in (a) for several different grating positions. In this example one diffraction grating tunes mid-IR pump frequency ω_1 from 980 cm^{-1} to 1054 cm^{-1} and the other diffraction grating tunes mid-IR pump frequency ω_2 from 1091 cm^{-1} to 1170 cm^{-1}. The electroluminescence spectrum of the laser material is shown with a dashed line. (c) Selected THz emission spectra of the device recorded for the same diffraction grating positions as in (b).

5.3 Investigation of internal nonlinearity of dual-stack bound-to-continuum active region design

The peak powers of mid-IR pump 1 and pump 2 as a function of ω_1 and ω_2 are shown in Figure 5.3(a-c) and 3(d-f), respectively. Measurements were performed at three different pump currents of 2.3 A, 2.8 A and 3.3 A (current density 6.2 kA/cm^2, 7.5 kA/cm^2, 8.8 kA/cm^2) – near threshold, in the middle of dynamic range, and near the rollover point, respectively. The effect of gain competition between the two mid-IR pumps can be observed: in Figure 5.3(a), the intensity of pump 1 decreases as the frequency of pump 2 is tuned towards ω_1, and in Figure 5.3(d), the intensity of pump 2 decreases as the frequency

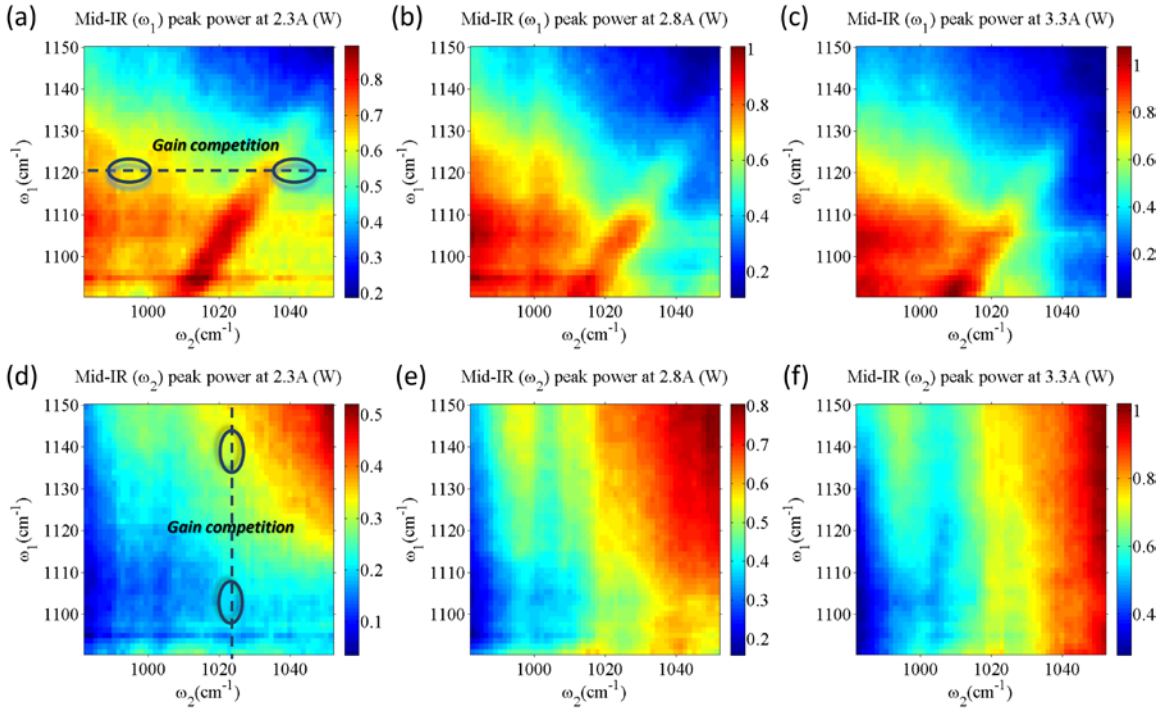

Figure 5.3: Mid-IR peak power output as a function of mid-IR pump frequencies ω1 and ω2. Panels (a), (b), and (c) show the peak power output of ω1 pump at pump currents of 2.3 A, 2.8 A and 3.3 A, respectively. Panels (d), (e), and (f) show the peak power output of ω2 pump at pump currents of 2.3 A, 2.8 A and 3.3 A, respectively.

of pump 1 is tuned towards ω_2. The similar gain competition effects are also seen for higher bias current in Fig. Figure 5.3(b-c) and Figure 5.3 (e-f). Gain competition is an intrinsic effect in all dual-color semiconductor lasers and it had been reported in previous chapters for THz DFG-QCLs. It can be seen in Figure 5.3(a) and Figure 5.3(d) that, despite gain competition, dual-color mid-IR pump operation is possible in a wide range of ω_1 and ω_2 frequencies. The balance of mid-IR pump powers can be managed by controlling the individual round-trip gain and/or loss for the two pumps. We further note that, despite gain competition, due to spatial filtering of EC feedback at device aperture, both mid-IR pumps in our lasers operate in TM_{00} mode as confirmed by far field measurements.

The dependence of THz peak power on the two mid-IR pump frequencies is shown in Figure 5.4(a-c). Similar to data in Figure 5.3(a-f), measurements for the data in Figure 5.4(a-c) were performed at three different pump current of 2.3 A, 2.8A and 3.3 A (current density 6.2 kA/cm^2, 7.5 kA/cm^2, 8.8 kA/cm^2). Figure 5.4(d-f) shows the mid-IR-to-THz conversion efficiency $\eta(\omega_1,\omega_2)$ for the three different bias currents, defined as the ratio of THz power output from a device to the product of mid-IR pump powers,

$$\eta(\omega_1,\omega_2)=\frac{W_{THz}(\omega_1,\omega_2)}{W_1(\omega_1,\omega_2)W_2(\omega_1,\omega_2)} \tag{5.3}$$

where $W_1(\omega_1,\omega_2)$ is the power of mid-IR pump 1 shown in Figure 5.3(a-c), $W_2(\omega_1,\omega_2)$ is the power of mid-IR pump 2 shown in Figure 5.3(d-f), and $W_{THz}(\omega_1,\omega_2)$ is the power of THz output shown in Figure 5.4(a-c). The dashed lines in Figure 5.4(a-c) represent positions of the same THz difference frequency of 2.8 THz, 3.2 THz, 3.6 THz and 4.0 THz. It can be seen in Figure 5.4(d-f) that the mid-IR-to-THz conversion efficiency profile as a function of ω_1 and ω_2 does not stay constant and the maximum of mid-IR-to-THz conversion efficiency is achieved for different combinations of mid-IR pump frequencies

as current through the device changes. This is true even if THz difference-frequency stays the same.

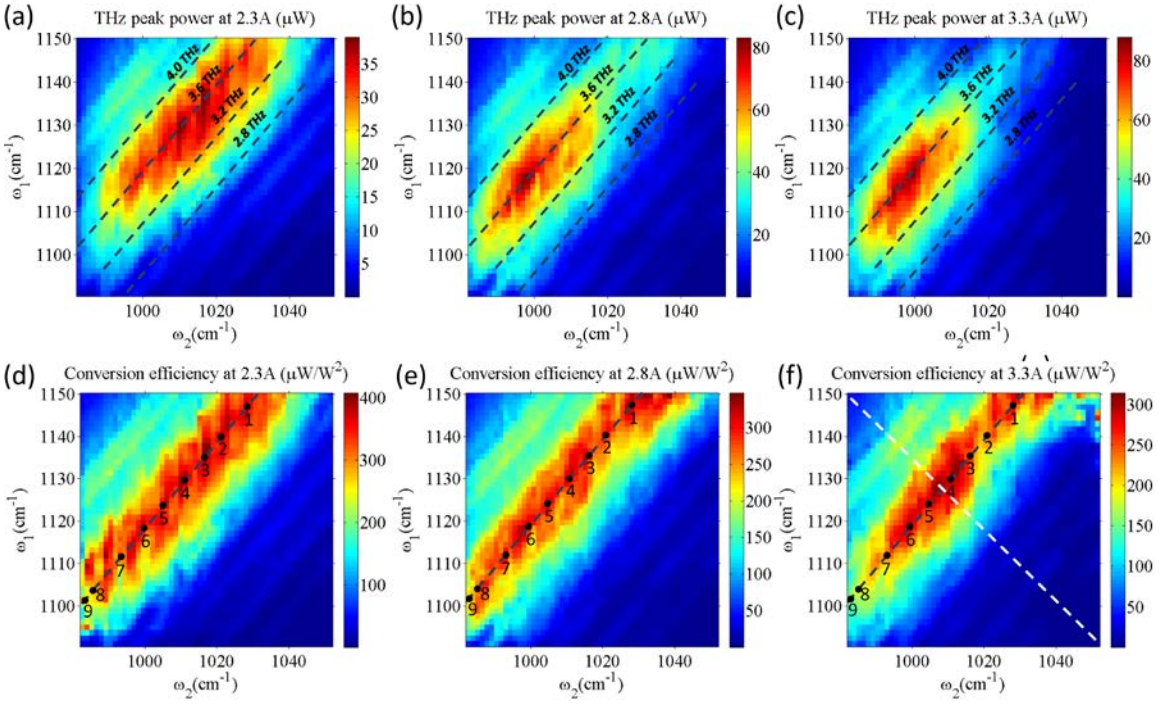

Figure 5.4: THz DFG performance of the device. Panels (a), (b), and (c) show the THz peak power output of the device at pump currents of 2.3 A, 2.8 A and 3.3 A, respectively, as a function of mid-IR pump frequencies ω_1 and ω_2. Panels (d), (e) and (f) show mid-IR-to-THz conversion efficiency of the device at pump currents of 2.3 A, 2.8 A and 3.3 A, respectively, as a function of mid-IR pump frequencies ω_1 and ω_2. Black dashed lines in all panels correspond to the sets of data points with the constant values of THz DFG frequency of 2.8, 3.2, 3.6 and 4.0 THz. Points labelled with numbers indicate frequencies of the two mid-IR pumps for which we performed more detailed measurements of THz power output as a function of mid-IR pump powers as shown in **Figure 5.5**. White dashed line in (f) indicates the set of data points used to determine Γ_{23} linewidth broadening factor as shown in **Figure 5.6**.

To illustrate this point further, we performed light-output-current characterization of our device in mid-IR and THz for 9 different combinations of ω_1 and ω_2 chosen to

produce THz difference-frequency at 3.57 THz. These ω_1 and ω_2 combinations are indicated with black dots in Figure 5.4(d-f). Figure 5.5(a) and Figure 5.5(b) show the power of mid-IR pump 1 and pump 2 as a function of current through the device for 9 different combinations of ω_1 and ω_2; the emission spectra at pump current of 3.3A for the same 9 combinations of ω_1 and ω_2 are shown in the inset of Figure 5.5 (b). Figure 5.5(c) shows THz light-output-current characteristics of the device producing 3.57 THz difference-

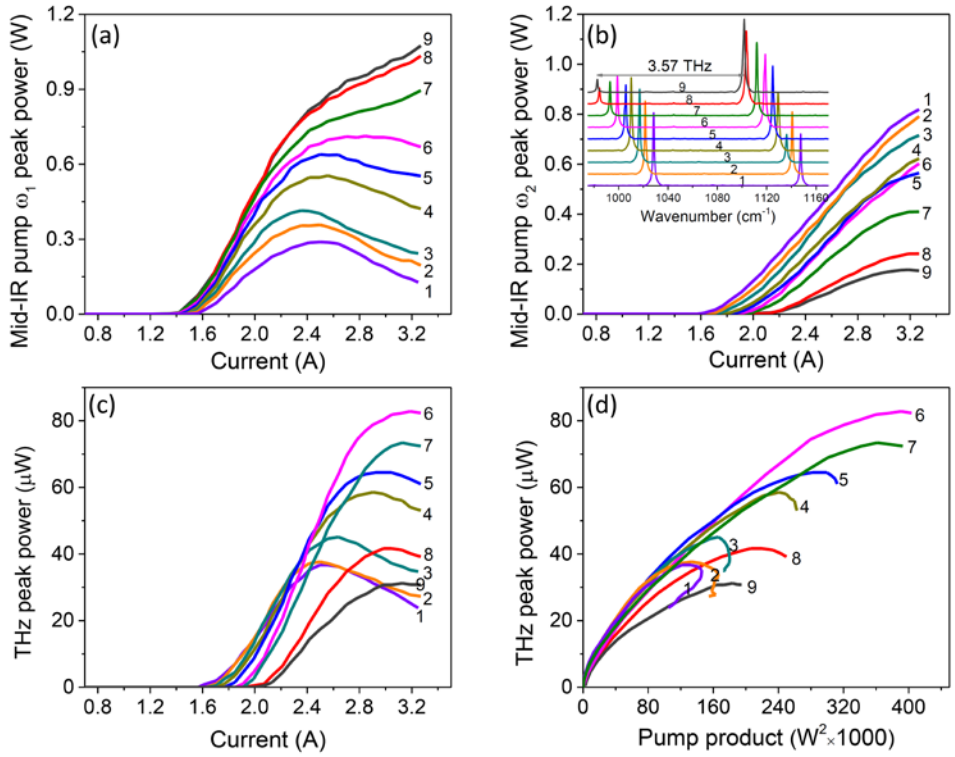

Figure 5.5: Device performance at fixed difference-frequency of 3.57 THz with 9 different combinations of ω_1 and ω_2 (indicated with 9 black dots in **Figure 5.4**(d)-(f)). Panels (a) and (b) show the power of mid-IR pump ω_1 and pump ω_2, respectively, as a function of current through the device. Inset in (b) shows the mid-IR emission spectra at pump current of 3.3A. Panel (c) shows THz light-output-current characteristics of the device and (d) shows THz power output as a function of the product of the mid-IR pump powers, for 9 different combinations of ω_1 and ω_2.

frequency and Figure 5.5 (d) plots THz power output as a function of the product of two mid-IR pump powers, obtained from the data shown in Figure 5.5(a,b), for the same combinations of ω_1 and ω_2. From Eq. (5.1), assuming constant magnitude of $\chi^{(2)}$, one expects linear dependence of THz power output from our devices on the product of mid-IR pump powers. However, Figure 5.5(d) shows that this is not the case experimentally. To explain the results, we need to consider the dependence of $\chi^{(2)}$ on the bias voltage. Indeed, Eq. (5.2) shows that, as transition energies between subbands 1, 2 and 3 change with applied bias, the value of $\chi^{(2)}$ and its dependence on ω_1 and ω_2 may vary significantly.

5.4 Measurement of transition linewidth in the active region

To provide qualitative explanation of the results in Figure 5.5, we computed the bandstructures of the two stacks (shown in Figure 5.1) that comprise the active region for different bias voltages: near the alignment point, in the middle of dynamic range, and near the rollover point (specifically, at 41 kV cm^{-1}, 44 kV cm^{-1}, and 47 kV cm^{-1}, respectively, for stack 1 and 46 kV cm^{-1}, 49 kV cm^{-1}, and 52 kV cm^{-1}, respectively, for stack 2). Transition energies and transition dipole moments between states 1, 2, and 3 were then computed from the bandstructures and Eq. (5.2) was used to calculate $\chi^{(2)}(\omega_1,\omega_2)$ in each of the two stacks. In this calculations, the linewidths for transitions between upper and lower laser states Γ_{21} and Γ_{31} were assumed to be 15 meV for both stacks based on electroluminescence measurements [24], while the linewidth Γ_{23} for the transition between lower laser states was varied from 2 meV to 8 meV. We have also assumed constant ΔN_e = 8.5×10^{14} cm^{-3} in accordance to the value used for similar devices in Ref. [24]. We note that the data in Figure 5.5(a,b) shows that threshold current density (and, correspondingly, ΔN_e) in our device may change by up to ~20% depending on the positions of ω_1 and ω_2 pumps. However, considering the qualitative nature of our theoretical model, we have

neglected the variation in ΔN_e to simplify calculations. More detailed analysis of the dependence of $\chi^{(2)}(\omega_1,\omega_2)$ on pump frequencies and threshold gain should also include electron transport and resultant non-uniform electric field distribution (band bending) across the active region and such analysis be performed using Monte-Carlo simulations [68,69] in the future.

We then used the slab-waveguide analysis that treats Cherenkov THz emission as a leaky waveguide mode to simulate mid-IR-to-THz conversion efficiency in our devices for different values of ω_1 and ω_2 at three different bias points. The procedure is described in details in Ref. [70] for Cherenkov second harmonic generation and is applied to THz DFG-QCL modelling in Ref. [24]. The results are shown in Figure 5.6 (a-c) for the case when we assume Γ_{23}=4 meV. Theoretical dependence of conversion efficiency on ω_1 and ω_2 is in good qualitative agreement with the experimental measurements in Figure 5.4(d-f), although, experimental values of conversion efficiencies are approximately 3 times lower than theory. This is likely due to limitations of the slab-waveguide model and uncertainties in materials parameters. Both theory and experiment show conversion efficiency for THz DFG at 3.57 THz drop by approximately 1.5 times as bias field increases. Also, at low-to-moderate bias field, both experimental data and theory shows nearly constant conversion efficiency for different combinations of mid-IR pump frequencies, as long as THz difference-frequency stays the same. At higher bias, both experimental data and theory shows that THz DFG conversion efficiency is maximized at specific combinations of ω_1 and ω_2, around 1130-1150 cm^{-1} and 1010-1030 cm^{-1}, respectively. Given the simplicity of our model, the agreement is remarkable. The experimental and theoretical results demonstrate that careful selection of the spectral

position of mid-IR pumps is critically important for optimization of THz DFG-QCL performance.

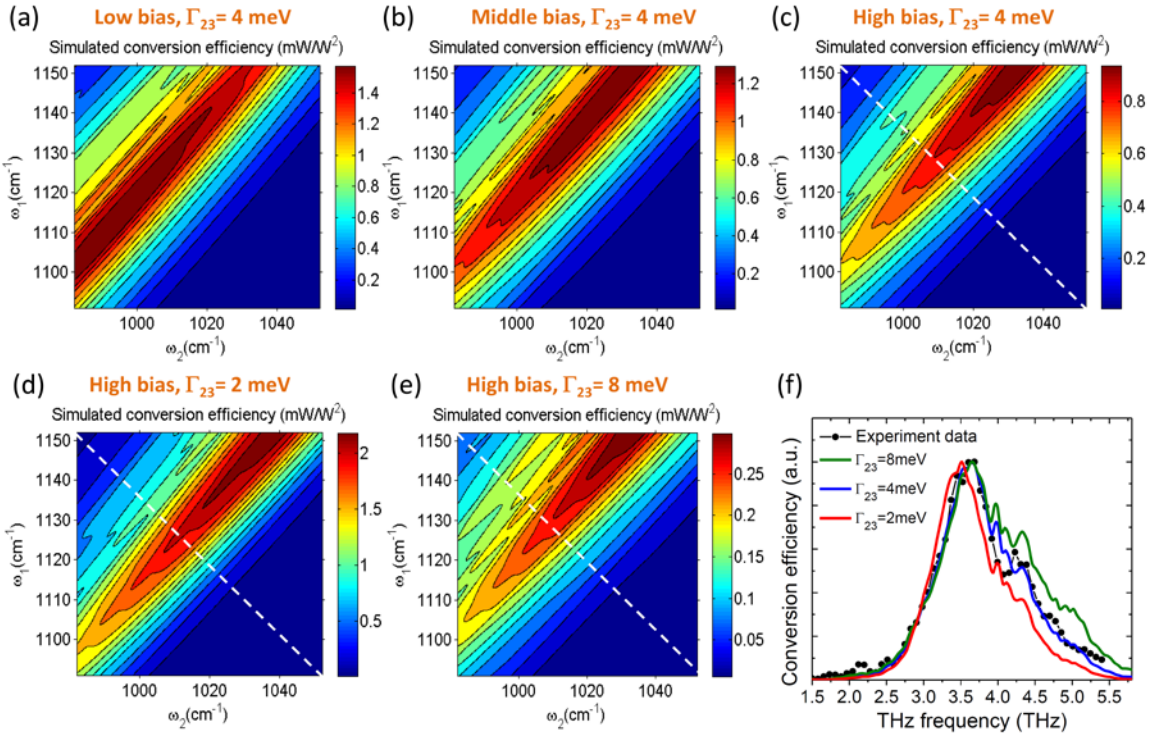

Figure 5.6: Calculated mid-IR-to-THz conversion efficiency for the tested devices as a function of mid-IR pump frequencies ω_1 and ω_2 assuming Γ_{23} = 4 meV near threshold (a), in the middle of dynamic range (b) and near the rollover point (c). (d,e) Calculated mid-IR-to-THz conversion efficiency for test devices as a function of mid-IR pump frequencies close to the rollover point and assuming Γ_{23} = 2 meV (d) and Γ_{23} = 8 meV (e). (f) Cross section data comparison between theory and experiment. Black circles are experimental data taken along white dashed line in **Figure 5.4**(f); red, blue and green lines are the theoretical values taken along white dashed line in panels (d), (c), and (e). Theoretical data with the linewidth broadening factor Γ_{23} = 4 meV provides the best match to the experimental data.

Finally, our 2D DFG spectroscopic analysis allows, for the first time, to deduce an approximate value of the intersubband transition linewidth Γ_{23} between lower laser states

of the bound-to-continuum QCL active region. We note that, since electron population difference between these lower laser states is very small, it is virtually impossible to measure Γ_{23} by linear absorption spectroscopy. In Figure 5.6(c), 6(d), and 6(e), we show simulated conversion efficiency at bias fields near the rollover point as a function of ω_1 and ω_2 assuming $\Gamma_{23}\approx$4 meV, 2 meV, and 8 meV for both QCL stacks, respectively. The best agreement between simulations and experimental measurements shown in Figure 5.4(f) is achieved for $\Gamma_{23}\approx$4 meV. To clarify this point further, we compare the experimental and theoretical data points taken along the white dashed lines in Figure 5.4(f) and Figure 5.6(c-e). The results are shown in Figure 5.6(f). Theoretical curve with Γ_{23}=4 meV clearly provides the best fit with the experimental data.

5.5 Summary

In summary, we demonstrated a dual-external cavity THz DFG-QCL system which is useful for initial characterization of THz DFG-QCL. This system allows to determine the best THz performance position with respect to the choices of two mid-IR pump frequencies. Our results demonstrate that mid-IR-to-THz conversion efficiency in Cherenkov THz DFG-QCLs may vary by a factor of 2 or more even for the same THz DFG frequency, depending on the spectral position of the mid-IR pumps. We have also experimentally deduced the linewidth of THz transitions between the lower laser states, which is critical for the accurate modeling of $\chi^{(2)}$ and understanding the optical loss in the lower laser level structure of mid-IR QCLs. The 2D spectroscopic technique presented here is expected to play a crucial role in the analysis and future optimization in the performance of THz DFG-QCLs. In chapter 6, we will use this system for characterizing different active regions designs since it provides a convenient way to characterize devices without fabrication of DFB gratings.

Appendix A: THz 2D mapping for dual-upper-state active region QCL

This 2D scan technology is useful for initial characterization of THz DFG-QCLs, in cooperation with Hamamatsu Photonics, we performed 2D mapping for DFG-THz generation for their buried heterostructure THz DFG-QCLs based on dual-upper-state active region design grown by Hamamatsu's MOCVD system. Band structure is shown in Figure 5.7, it contains two upper states, one injector state injects electrons to both states. Details of the active region sequence can be found in Ref. [36].

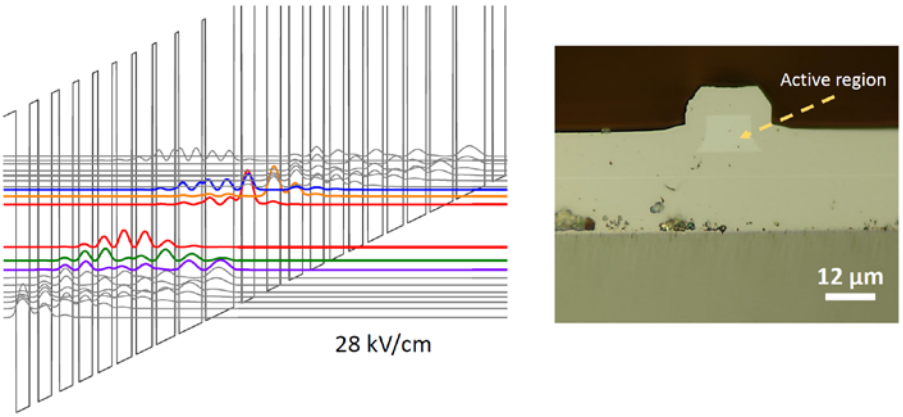

Figure 5.7: (a) Conduction band structure of the dual-upper-state active region design [36]. (b) Optical image of the facet condition of the buried heterostructure device, active region is buried in regrown InP cladding layer.

2D mapping results tested in the double external cavity system discussed in previous sections are shown in Figure 5.8 for a 3-mm-long, 12-um-wide device with back facet AR coated and the substrate of the front facet polished at a 25-degree angle. From Figure 5.8(c), we can see, THz power and conversion efficiency peaks around 3 THz to 3.5 THz, choosing one mid-IR pump around 950 cm^{-1} ~ 970 cm^{-1} and the other mid-IR pump around 850 cm^{-1} ~ 860 cm^{-1} will give us the best THz performance. In this particular design, the best THz power position and best conversion efficiency position matches well with

each other. Detailed light-current measurements for both mid-IR pumps and THz generation are performed at seven different combinations of frequency ω_1 and ω_2 in Figure 5.9. Frequency separation ω_1- ω_2 for these seven positons is kept the same at 2.95 THz, indicated as the black dots in Figure 5.8(d). Mid-IR-to-THz conversion efficiency can change by two to three times in this case, further supporting our previous findings. Both THz power and mid-IR pump power of this device are not very high though, which is mainly due to the imperfection of the top cladding overgrowth step for buried heterostrucure devices.

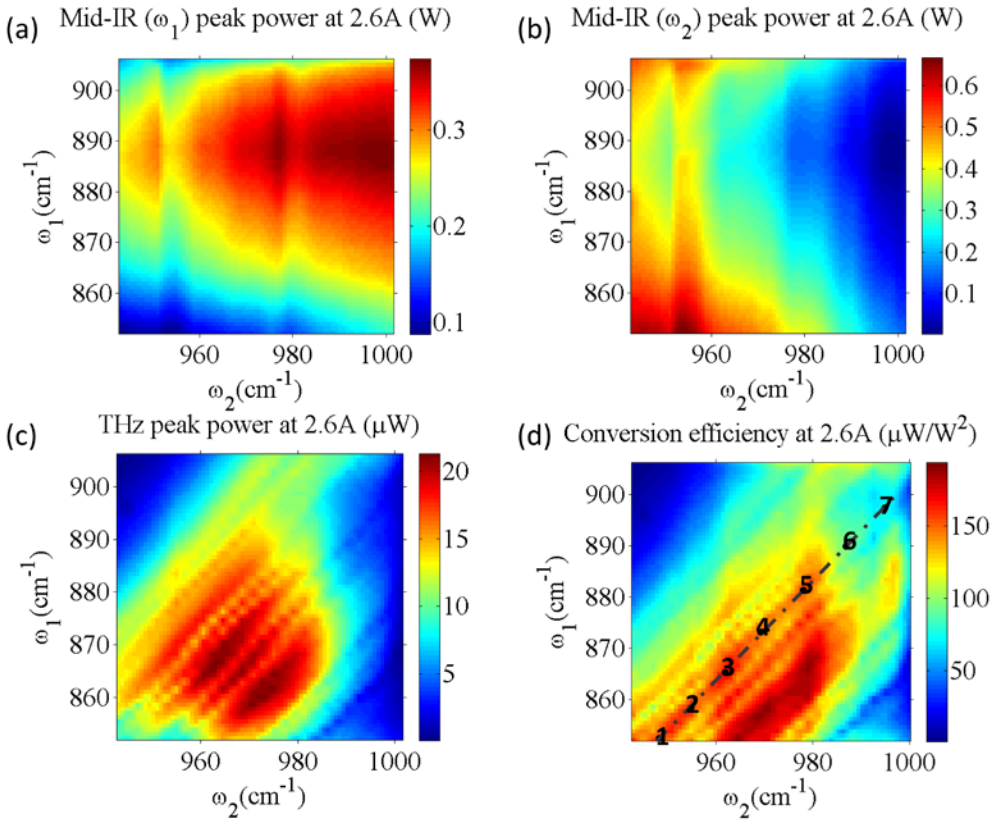

Figure 5.8: 2D mapping spectra of the Fabry-Perot device measured with double Littrow external cavity set-up. Panel (a) and (b) are mid-IR pump power for ω_1 and ω_2, respectively, as a function of pump frequency

ω_1 and ω_2. (c) THz peak power as a function of ω_1 and ω_2. (d) Device conversion efficiency as a function of ω_1 and ω_2. All measurements are performed at the same applied bias.

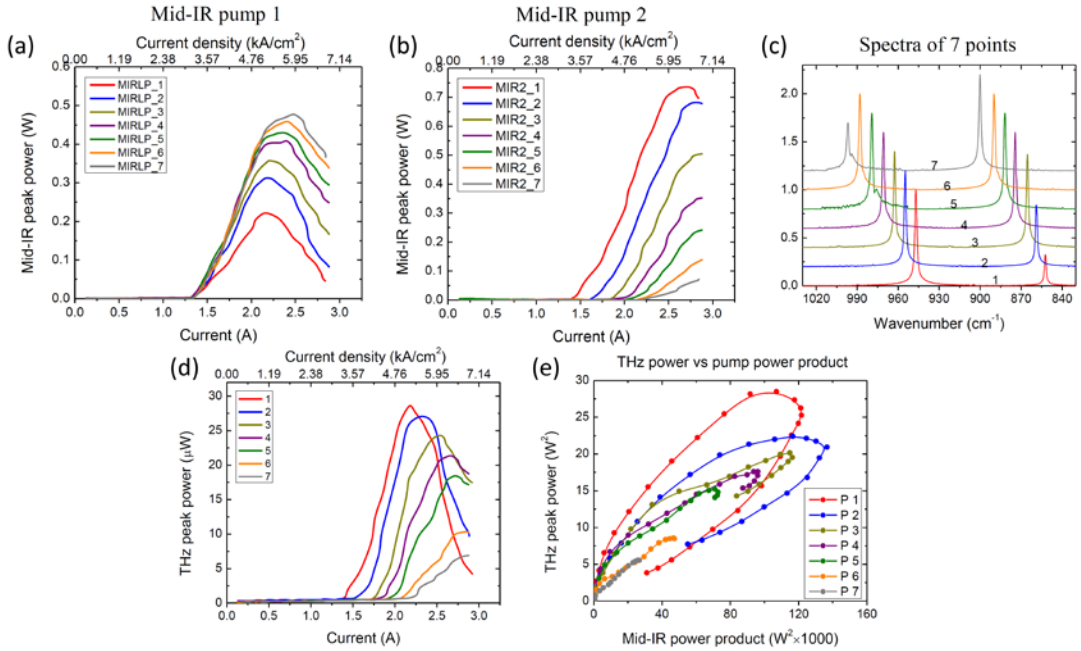

Figure 5.9: (a) L-I curves for mid-IR pump 1, (b) L-I curves for mid-IR pump 2, (c) Mid-IR spectra, (d) L-I curves for THz generation, (e) THz peak power as a function of pump power product at 7 point positions indicated as the black dots in **Figure 5.8**(d). All these 7 points represent the same pump frequency separation of 2.95 THz.

Chapter 6: THz DFG-QCLs with improved conversion efficiency

6.1 Introduction

Previous chapters listed the current research status of widely tunable THz DFG-QCLs, that used either a single Littrow external cavity laser system with integrated DFB gratings or a double-Littrow external cavity laser system. Although these results demonstrated that THz DFG-QCLs could provide record THz frequency tuning in the 1-6 THz range, the best power performance of THz DFG-QCLs is always in the 3-5 THz range. On the high-frequency end, the onset of high optical losses in InGaAs/AlInAs/InP materials because of tails of LO-phonon absorption bands (Reststrahlen band) limits the efficiency of THz generation. On the low-frequency end, THz generation efficiency is limited principally by high free carrier absorption in the QCL waveguide and the $(\omega_{THz})^2$ dependence of the DFG efficiency. Another important factor is the spectral dependence of intersubband optical nonlinearity $\chi^{(2)}$.

In all the room temperature THz DFG-QCL devices reported [21-36], the intersubband nonlinearity $\chi^{(2)}$ has been attributed to the double resonance (DR) regime in a three-level system, where THz emission resonates with the doublet of two lower laser states. While this is true for high THz frequencies (3~6 THz), it may not be true for those from 0.5~3 THz. When we wrote the complete quantum mechanical expression for $\chi^{(2)}$, we found that as the THz frequency detuned more and more from the double-resonance regime and approached less than 1 THz, another second-order nonlinear effect, the optical rectification (OR) process, dominated the DR process. Taking both DR and OR processes for nonlinearity $\chi^{(2)}$ into account, we predicted theoretically much higher nonlinearity $\chi^{(2)}$ in the 1~3 THz range and below. To verify our theory experimentally, we needed to measure the spectral dependence of $\chi^{(2)}$.

The conversion efficiency $\eta(\omega_{THz})$ of Cherenkov THz DFG-QCLs has the following relation:

$$\eta(\omega_{THz}) \propto \left|\chi^{(2)}(\omega_{THz})\right|^2 |H_{THz}(\omega_{THz})|^2 \tag{6.1}$$

where $H_{THz}(\omega_{THz})$ is the out-coupled THz field through the substrate when one assumes that $\chi^{(2)}$ for all the THz frequencies is 1. To improve the final conversion efficiency of THz DFG-QCL, it is important to model the Cherenkov waveguide accurately to obtain $H_{THz}(\omega_{THz})$ and understand $\chi^{(2)}(\omega_{THz})$. This chapter discusses first the origin of nonlinearity in mid-infrared QCLs, introduces the modeling method of the Cherenkov THz waveguide, and finally, discusses the theoretical and experimental results of high-efficiency THz generation based on optimized long-wavelength (~15 μm) infrared QCLs.

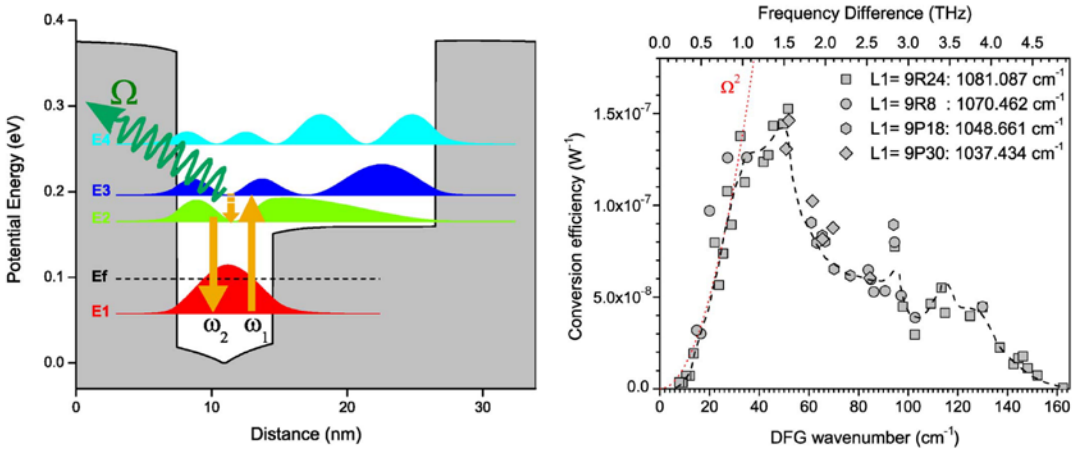

Figure 6.1: (a) Conduction band diagram of the structure and moduli squared of the first four wave functions. The period of the MQW consists of a 7.4 nm $Al_{0.43}Ga_{0.57}As$ barrier, a 7.1 nm GaAs well, and a 12 nm $Al_{0.16}Ga_{0.84}As$ step barrier; (b) The spectrum of the conversion efficiency of difference frequency mixing at room temperature [72].

6.2 Origins of DFG nonlinearity in mid-infrared quantum cascade lasers

Sirtori *et al.* reported the first demonstration of difference frequency generation in MQW in 1994 [46], in which two external pumps illuminated a coupled quantum well to generate far-infrared radiation as mentioned in Chapter 1. In this demonstration, they observed only a doubly resonant difference frequency. Dupont *et al*. reported the first consideration of optical rectification nonlinearity for intersubband difference frequency mixing for THz generation in 2006 [72]. In their report, two tunable CW CO_2 lasers, L1 and L2, were used to pump a step MQW, as shown in Figure 6.1(a)**.** They observed an increase in the conversion efficiency approaching the low THz frequency side as shown in the DFG conversion efficiency spectrum in Figure 6.1(b), which cannot be explained by considering only DR regime. They indicated that this DFG nonlinear interaction is the sum of two contributions: the optical rectification (OR) regime, which involves two states, and the double resonance (DR) regime, with three states. Because a large OR coefficient has been observed previously in passive optically pumped MQWs in the THz DFG process, we believe that OR process also should play a significant role for DFG in mid-infrared quantum cascade lasers. We can obtain more detailed information about the origin of the

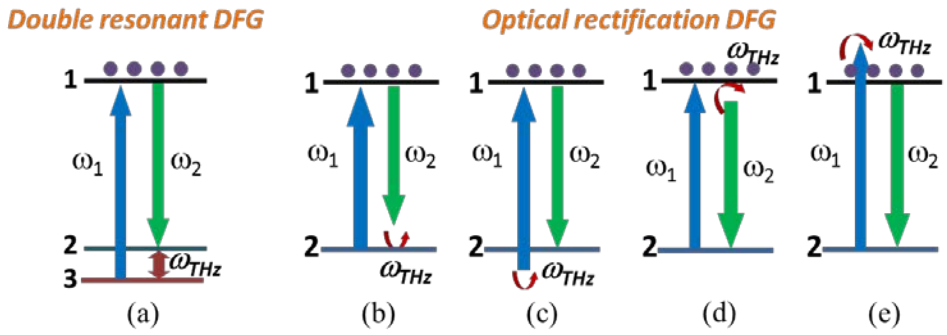

Figure 6.2: (a) Quantum path of double resonant DFG; (b-e) quantum path of OR DFG associated with state |1> and state |2>.

difference frequency nonlinear susceptibility in mid-infrared QCLs using the double Littrow external-cavity laser system demonstrated in Chapter 5.

The active region of the QCL usually contains an upper state and several lower states, which is considered a three-level system between levels 1, 2, and 3 in QCL. We can write the full quantum mechanical expression for $\chi^{(2)}$ [63] for this three-level system (assuming electron population in the ground state is the same, and is much smaller than in the upper states), as Eq. (6.1).

$$\chi^{(2)}(\omega_{THz}=\omega_1-\omega_2,-\omega_2,\omega_1)=\Delta N_e\frac{e^3}{\hbar^2\varepsilon_0}\sum_{lmn}\rho_{ll}^{(0)}\times\left(\begin{array}{l}\frac{z_{ln}z_{nm}z_{ml}}{(\omega_{nl}-\omega_{THz}-i\Gamma_{nl})(\omega_{ml}-\omega_1-i\Gamma_{ml})}\\+\frac{z_{ln}z_{nm}z_{ml}}{(\omega_{nl}-\omega_{THz}-i\Gamma_{nl})(\omega_{ml}+\omega_2-i\Gamma_{ml})}\\+\frac{z_{ln}z_{nm}z_{ml}}{(\omega_{mn}-\omega_{THz}-i\Gamma_{mn})(\omega_{nl}+\omega_1+i\Gamma_{nl})}\\+\frac{z_{ln}z_{nm}z_{ml}}{(\omega_{mn}-\omega_{THz}-i\Gamma_{mn})(\omega_{nl}-\omega_2+i\Gamma_{nl})}\\+\frac{z_{ln}z_{nm}z_{ml}}{(\omega_{nm}+\omega_{THz}+i\Gamma_{nm})(\omega_{ml}-\omega_1-i\Gamma_{ml})}\\+\frac{z_{ln}z_{nm}z_{ml}}{(\omega_{nm}+\omega_{THz}+i\Gamma_{nm})(\omega_{ml}+\omega_2-i\Gamma_{ml})}\\+\frac{z_{ln}z_{nm}z_{ml}}{(\omega_{ml}+\omega_{THz}+i\Gamma_{ml})(\omega_{nl}+\omega_1+i\Gamma_{nl})}\\+\frac{z_{ln}z_{nm}z_{ml}}{(\omega_{ml}+\omega_{THz}+i\Gamma_{ml})(\omega_{nl}-\omega_2+i\Gamma_{nl})}\end{array}\right) \tag{6.2}$$

where ω_1, ω_2 are the two pump frequencies, ω_{THz} is the THz frequency generated, and ω_{ij} ($i,j=m,n,l$) is the transition frequency between subbands. When l=1, m=2, and n=3, the third and sixth term in Eq. (6.2) meets the resonance condition in which the real part of both denominators reaches zero; the dominant two resonant terms can be simplified as:

$$\chi_{DR}^{(2)}(\omega_1,\omega_2)\approx\Delta N_e\frac{e^3}{\hbar^2\varepsilon_0}\times\left(\frac{-z_{12}z_{23}z_{31}}{(\omega_{THz}-\omega_{23}+i\Gamma_{23})(\omega_1-\omega_{13}+i\Gamma_{31})}+\frac{-z_{12}z_{23}z_{31}}{(\omega_{THz}-\omega_{23}+i\Gamma_{23})(-\omega_2+\omega_{12}+i\Gamma_{21})}\right) \tag{6.3}$$

We call this the double resonance (DR) condition, and the two related terms are called “DR terms”; Figure 6.2(a) shows the resonant quantum path.

Now, when the pump frequencies, ω_1, ω_2, are similar, and the difference frequency is detuned far from the energy spacing between the doublet states |2> and |3>, the DR condition can no longer be satisfied, and another nonlinear effect, the OR process, takes over. Consider l=1, m=n=2, and the third and sixth terms in Eq. (6.2) dominate; these two terms are called “OR terms,” and Figure 6.2 (b) and (c) show the related quantum path.

$$\chi_{OR}^{(2)}(\omega_1,\omega_2)(l=1,m=n=2)=\Delta N_e\frac{e^3}{\hbar^2\varepsilon_0}\times\left(\frac{-z_{12}{}^2z_{22}}{(\omega_{THz}+i\Gamma_{22})(-\omega_{12}+\omega_1+i\Gamma_{21})}+\frac{z_{12}{}^2z_{22}}{(\omega_{THz}+i\Gamma_{22})(-\omega_{12}+\omega_2-i\Gamma_{21})}\right) \tag{6.4}$$

Consider when l=1, m=1, n=2, and the seventh term in Eq. (6.2) meets the resonance condition; Figure 6.2(d) shows the related quantum path.

$$\chi_{OR}^{(2)}(\omega_1,\omega_2)(l=1,m=1,n=2)=\Delta N_e\frac{e^3}{\hbar^2\varepsilon_0}\times\left(\frac{z_{12}{}^2z_{11}}{(\omega_{THz}+i\Gamma_{11})(-\omega_{12}+\omega_1+i\Gamma_{21})}\right) \tag{6.5}$$

Consider when l=1, m=2, n=1, and the second term in Eq. (6.2) meets the resonance condition; Figure 6.2(e) shows the related quantum path.

$$\chi_{OR}^{(2)}(\omega_1,\omega_2)(l=1,m=2,n=1)=\Delta N_e\frac{e^3}{\hbar^2\varepsilon_0}\times\left(\frac{-z_{12}{}^2z_{11}}{(\omega_{THz}+i\Gamma_{11})(-\omega_{12}+\omega_2-i\Gamma_{21})}\right) \tag{6.6}$$

The nonlinear coefficient associated with the OR process is dominated by 4 OR terms in a two-level system within state |1> and state |2>. Summing all four terms, we obtain the expression for the “OR term” associated with state |1> and state |2>:

$$\chi_{OR}^{(2)}(\omega_1,\omega_2)=\begin{pmatrix}\chi_{OR}^{(2)}(\omega_1,\omega_2)(l=1,m=n=2)\\+\chi_{OR}^{(2)}(\omega_1,\omega_2)(l=1,m=1,n=2)\\+\chi_{OR}^{(2)}(\omega_1,\omega_2)(l=1,m=2,n=1)\end{pmatrix}$$

$$=\Delta N_e\frac{e^3}{\hbar^2\varepsilon_0}\times\left(\begin{array}{l}\dfrac{-z_{12}{}^2z_{22}}{(\omega_{THz}+i\Gamma_{22})(-\omega_{12}+\omega_1+i\Gamma_{21})}+\dfrac{z_{12}{}^2z_{11}}{(\omega_{THz}+i\Gamma_{11})(-\omega_{12}+\omega_1+i\Gamma_{21})}\\+\dfrac{z_{12}{}^2z_{22}}{(\omega_{THz}+i\Gamma_{22})(-\omega_{12}+\omega_2-i\Gamma_{21})}+\dfrac{-z_{12}{}^2z_{11}}{(\omega_{THz}+i\Gamma_{11})(-\omega_{12}+\omega_2-i\Gamma_{21})}\end{array}\right)$$

$$= \Delta N_e \frac{e^3}{\hbar^2 \varepsilon_0} \times \left(\left(\frac{z_{12}{}^2 z_{22}}{\omega_{THz} + i\Gamma_{22}} + \frac{-z_{12}{}^2 z_{11}}{\omega_{THz} + i\Gamma_{11}} \right) \left(\frac{\omega_{THz} + 2i\Gamma_{21}}{(-\omega_{12} + \omega_1 + i\Gamma_{21})(-\omega_{12} + \omega_2 - i\Gamma_{21})} \right) \right)$$
$$\approx \Delta N_e \frac{e^3}{\hbar^2 \varepsilon_0} \times \left(\left(\frac{\omega_{THz} + 2i\Gamma_{21}}{\omega_{THz} + i\Gamma} \right) \left(\frac{z_{12}{}^2 (z_{11} - z_{22})}{(-\omega_{12} + \omega_1 + i\Gamma_{21})(\omega_{12} - \omega_2 + i\Gamma_{21})} \right) \right) \quad (6.7)$$

Similarly, we can derive the OR terms of $\chi^{(2)}$ associated with state |1> and state |3>. The final nonlinearity, including both DR and OR terms in a three-level system can be expressed as:

$$\chi^{(2)}(\omega_1, \omega_2) \approx \Delta N_e \frac{e^3}{\hbar^2 \varepsilon_0} \times \left(\begin{array}{l} \frac{-z_{12} z_{23} z_{31}}{(\omega_{THz} - \omega_{23} + i\Gamma_{23})(\omega_1 - \omega_{13} + i\Gamma_{31})} + \frac{-z_{12} z_{23} z_{31}}{(\omega_{THz} - \omega_{23} + i\Gamma_{23})(-\omega_2 + \omega_{12} + i\Gamma_{21})} \\ + \frac{z_{13}^2 (z_{11} - z_{33})}{(\omega_{13} - \omega_2 + i\Gamma_{13})(\omega_1 - \omega_{13} + i\Gamma_{13})} \frac{\omega_{THz} + i2\Gamma_{13}}{\omega_{THz} + i\Gamma} + \frac{z_{12}^2 (z_{11} - z_{22})}{(\omega_{12} - \omega_2 + i\Gamma_{12})(\omega_1 - \omega_{12} + i\Gamma_{12})} \frac{\omega_{THz} + i2\Gamma_{12}}{\omega_{THz} + i\Gamma} \end{array} \right) \quad (6.8)$$

In Eq. (6.2-6.8), ω_1 and ω_2 are the frequencies of the mid-IR pumps, $\omega_{THz}=\omega_1-\omega_2$ is the THz difference-frequency, ΔN_e is the population inversion density, ez_{ij}, ω_{ij}, and $2\Gamma_{ij}$ are the transition dipole moments, transition frequency, and transition line width between states *i* and *j*, respectively, and $1/\Gamma$ is the average relaxation time of all the laser states. It is clear that OR process will occur as long as the centroids of the electrons in states |1> and |2> (or |3>) differ ($z_{11} - z_{22} \neq 0$ or $z_{11} - z_{33} \neq 0$).

The understanding of nonlinearity $\chi^{(2)}$ above provides us with new clues to design THz DFG-QCL. Not only should we focus on maximizing the double resonance part of the nonlinearity, but we also should focus on enlarging the OR aspect of the nonlinearity, especially in the low THz frequency range. Take a bound-to-continuum active region design with gain centered around 10 μm as an example; Figure 6.3(a) shows the conduction band structure, and it is clear that the difference in the electrons' centroids between the upper and lower laser states are quite large, approximately 20~30 nm. If we recalculate $\chi^{(2)}$ including both DR terms (the first two terms in the sum) and OR terms (the last two terms

in the sum) in Eq. 6.8, the calculated $|\chi^{(2)}|$ for this band structure is that shown in Figure 6.3(b).

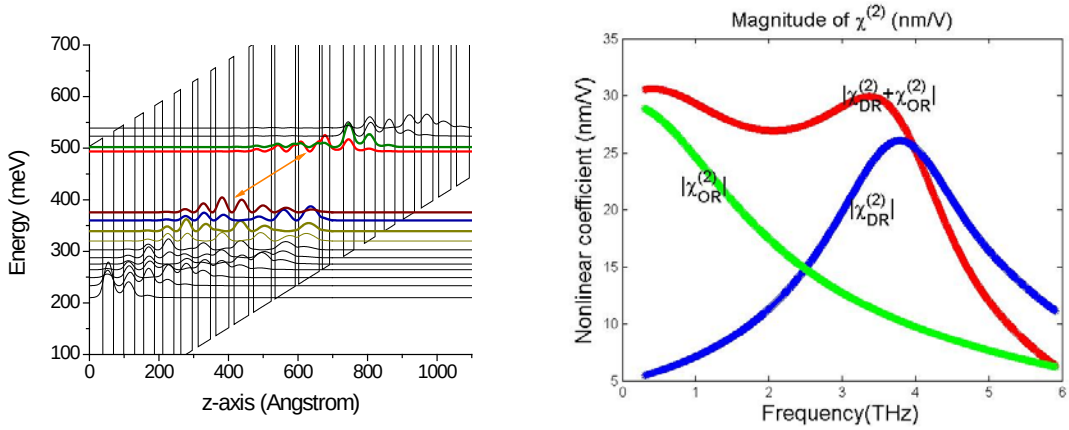

Figure 6.3: (a) One period of the conduction band structure for a bound-to-continuum active region design with gain centered around 10 μm. The layer sequence begins with the injection barrier, and is **39**/22/**8**/60/**9**/59/**10**/52/**13**/43/**14**/38/**15**/36/**16**/34/**19**/33/**23**/32/**25**/32/**29**/31, where the layer thicknesses are in angstroms, bold numbers indicate barriers, and underlined numbers indicate regions doped with Si to $n=2\times10^{17}$ cm^{-3}; (b) The magnitude of $\chi^{(2)}$ including the DR terms only (blue line), the OR terms only (green line), and both DR and OR terms (red line), respectively. Calculation assumes Γ_{23} = 4 meV and Γ= 6 meV.

6.3 Cherenkov waveguide simulation

Theoretically, we predicted a much higher $\chi^{(2)}$ in the low-frequency range (1~3 THz), but to obtain experimental results of $\chi^{(2)}$, we had to derive the $\chi^{(2)}$ value indirectly by measuring conversion efficiency. This indirect method of measuring $\chi^{(2)}$ requires accurate modeling of the waveguide effect and other effects in the final conversion efficiency.

Following the approach outlined in Ref. [71], we were able to determine an analytical solution of the Cherenkov wave in a slab waveguide model (Figure 6.4). The expression of the nonlinear polarization is:

$$P_x^{(2)}(x,z) = \varepsilon_0 \chi^{(2)} E_{1x}(x) e^{i\beta_1 z} E_{2x}{}^{*}(x) e^{-i\beta_2 z}$$
$$= \varepsilon_0 \chi^{(2)} \left(\frac{n_{1,eff}}{c} \frac{H_{1y}(x)}{\varepsilon_0 \varepsilon_1}\right)\left(\frac{n_{2,eff}}{c} \frac{H_{2y}(x)}{\varepsilon_0 \varepsilon_2}\right) e^{i(\beta_1 - \beta_2)z} \quad (6.9)$$

where $E_{1x}(x)$ and $E_{2x}(x)$ are the x-components of the E-fields of the two mid-IR pumps, and $H_{1y}(x)$ and $H_{2y}(x)$ are the y-components of the H-fields of the two mid-IR pumps. $n_{i,eff}$, ε_i, and β_i are the effective refractive index, the material index in the active region, and the wave vector for pump ω_i, respectively. The analytical expression of $H_{1y}(x)$ and $H_{2y}(x)$ can be approximated further as:

$$H_{iy}(x) \approx H_{iy}^{\max} \cos\left(\frac{\omega_i}{c}\sqrt{(n_{AR,i})^2 - (n_{eff,i})^2}\, x\right) \quad (6.10)$$

The Cherenkov wave can be considered the TM-polarized solution of the wave equation in a slab waveguide with the polarization source given in Eq. (6.9) in the active region layer. The Cherenkov mode should satisfy the following form:

$$\vec{H}(x,z) = H_{THz}(x) e^{i(\beta_1 - \beta_2)z} \vec{y} \quad (6.11)$$

and it also should satisfy the following inhomogeneous wave equation in each layer of the waveguide and the corresponding boundary conditions:

$$\left[\frac{\partial^2}{\partial x^2} + \frac{\partial^2}{\partial z^2} + \frac{\omega_{THz}{}^2}{c^2}\varepsilon_{i,THz}\right] H_{THz}(x) e^{i(\beta_1 - \beta_2)z} = i\omega_{THz} \frac{\partial P_x^{(2)}(x,z)}{\partial z} \quad (6.12)$$

The solution of the wave equation in the waveguide layer without a polarization source is a homogeneous solution in which the right side of Eq. (6.12) equals zero,

$$H_{THz}(x) = a_i \times Exp\left[\sqrt{(\beta_1 - \beta_2)^2 - \frac{\omega_{THz}{}^2}{c^2}\varepsilon_{i,THz}}\, x\right] + b_i \times Exp\left[-\sqrt{(\beta_1 - \beta_2)^2 - \frac{\omega_{THz}{}^2}{c^2}\varepsilon_{i,THz}}\, x\right] \quad (6.13)$$

In the layer with the nonlinear polarization wave, the solution is a sum of the homogeneous solution and a particular solution. The particular solution of Eq. (6.12) in this layer with nonlinear polarization wave is:

$$H_{THz}(x) = -\omega_{THz}^2 n_g \frac{\chi^{(2)} n_{eff}^2 H_{1y}^{\max}(H_{2y}^{\max})^*}{2\varepsilon_0 c^3 n_{AR}^4} \left[\frac{\cos((\kappa_1+\kappa_2)x)}{[\frac{\omega_{THz}^2}{c^2} n_{AR,THz}^2 - (\beta_1-\beta_2)^2] - (\kappa_1+\kappa_2)^2} + \frac{\cos((\kappa_1-\kappa_2)x)}{[\frac{\omega_{THz}^2}{c^2} n_{AR,THz}^2 - (\beta_1-\beta_2)^2] - (\kappa_1-\kappa_2)^2} \right] \quad (6.14)$$

Here we used $|\beta_1 - \beta_2| = \frac{n_g \omega_{THz}}{c}$. The solution in each layer must satisfy the boundary condition at the interface as well, and solving the linear equations of these boundary conditions allowed us to determine the analytical expression of the $H_{THz}(x)$. We used this method to establish conversion efficiency in Chapter 5 as well. Although it does not consider the width of the ridge waveguide, it offers a relatively accurate approximation of the THz wave in the waveguide. To consider the ridge width effect on THz radiation, a 3D numerical model using COMSOL can be employed.

Further, for all of the calculations presented in this chapter, we obtained the values of the refractive indices in our QCL layers by combining the table values of the refractive indices of undoped semiconductor compounds with the Drude model that had a relaxation time constant of $\tau=10^{-13}$ sec to account for the free-carrier contribution. The refractive indices of undoped $Al_{0.48}In_{0.52}As$ and $In_{0.53}Ga_{0.47}As$ compounds in the waveguide core were calculated using the linear interpolation between the data for the binary compounds. The effective index at each particular pump frequency was simulated using COMSOL. Figure 6.4 shows the index of the SI-InP substrate based on the results of the experimental measurements made in collaboration with Prof. Gorshunov's group [82].

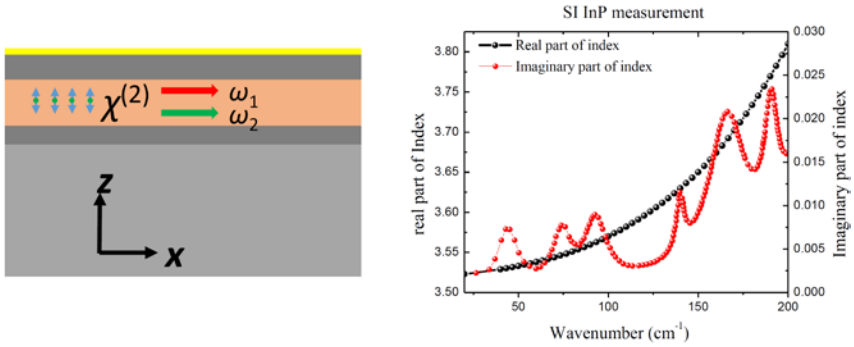

Figure 6.4: Schematic of slab waveguide model (left panel). Refractive index of SI InP substrate, including both real part and imaginary part (right panel) [82].

6.4 THz DFG-QCL based on a three-phonon-resonance design

Before understanding the OR effect of nonlinearity, we expected to increase nonlinearity at lower THz frequencies (1~3 THz) by creating an active region with very small energy separation between the two lower laser states. We found that a state of the art three-phonon-resonance design [74] could achieve our purpose, as it contains a tiny energy separation between the two lower states |2> and |3> to allow efficient electron extraction. Figure 6.5(a) shows the conduction band structure of this design. The energy separation between state |2> and state |3> was approximately 2.3 THz, as indicated by the peak position of DR $\chi^{(2)}$ in Figure 6.5(b). Below 2.3 THz, the OR term tended to sum to the total nonlinearity, and above 2.3 THz, the OR term tended to cancel out the DR term and decrease the total nonlinearity. As a result, the value of $|\chi^{(2)}|$ at 3.5 THz decreased where the Cherenkov waveguide had the maximum THz signal response, as indicated in the last

section.

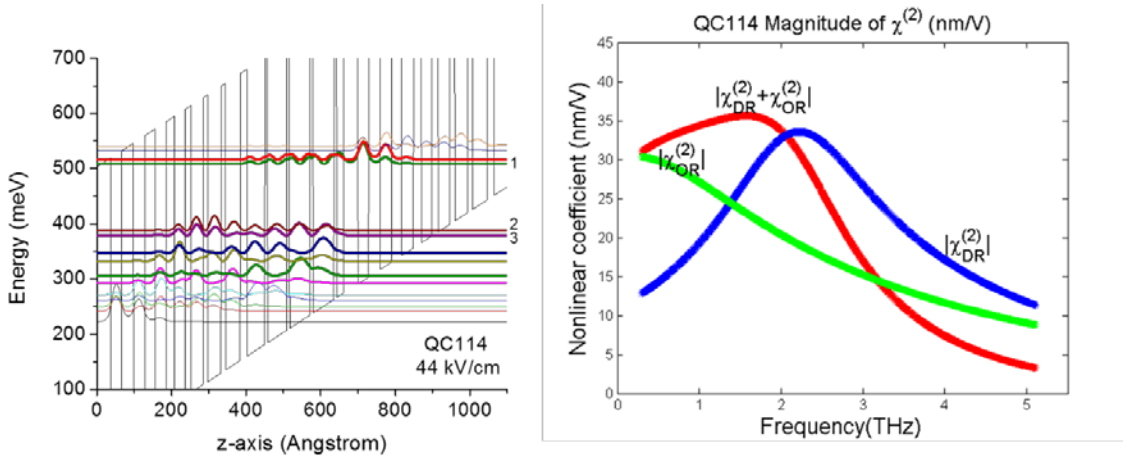

Figure 6.5: (a) One period of conduction band structure for three-phonon active region design with gain centered around 10 μm. The layer sequence begins with the injection barrier, which is **38**/19/**7**/56/**8**/55/**8**/51/**7**/48/**18**/40/**12**/35/**13**/32/**16**/29/**21**/31/**27**/31/**31**/29, where the layer thicknesses are in angstroms, bold numbers indicate barriers, and underlined numbers indicate regions doped with Si to n= 2.7×10^{17} cm^{-3}; (b) The magnitude of $\chi^{(2)}$ including the DR terms only (blue line), the OR terms only (green line), and both DR and OR terms (red line), respectively. Calculation assumes Γ_{23} = 4 meV and Γ= 6 meV.

We fabricated devices based on this design into Fabry-Perot ridges with the back facet coated with an anti-reflection (AR) coating and tested them in the dual-grating Littrow-type external cavity system. As expected, the device gain was narrow because of smaller energy separation between the two lower states. For this single-stack active region device, mid-infrared pump frequency tuning could sweep from 945 cm^{-1} to 1075 cm^{-1}, and

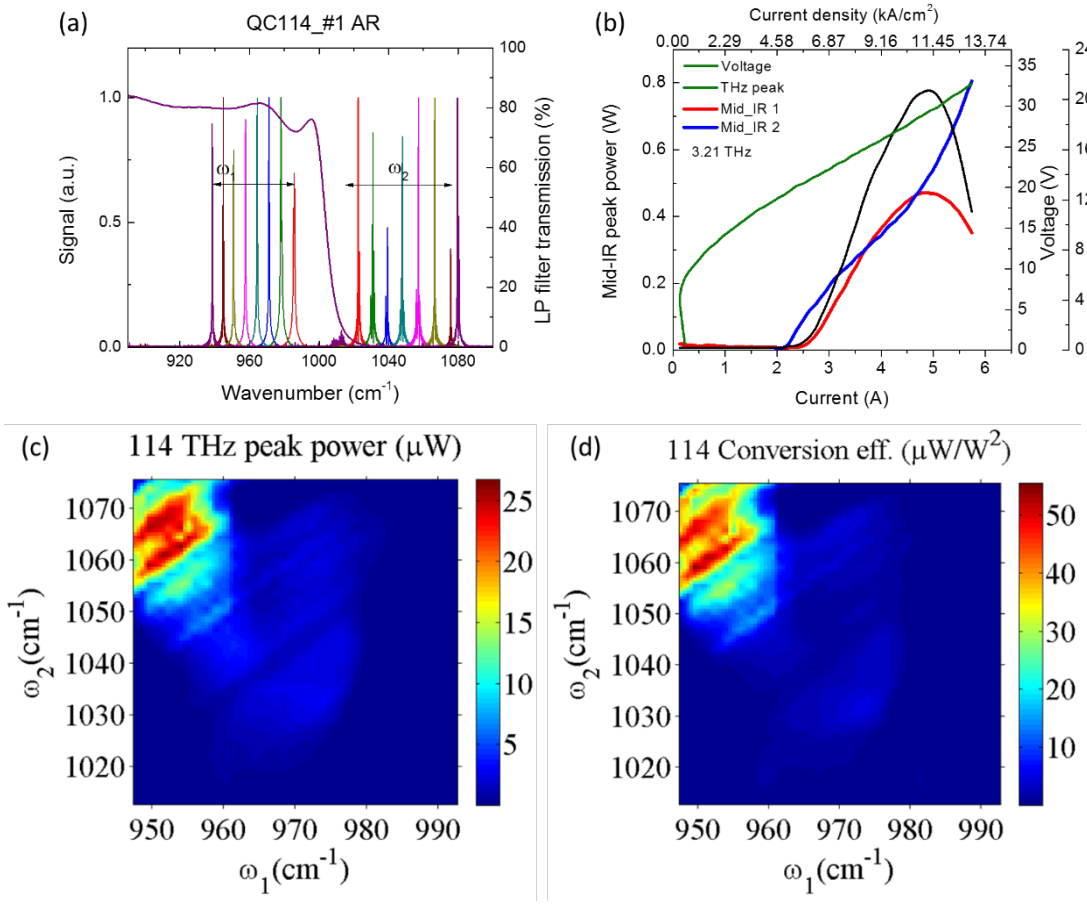

Figure 6.6: (a) Tuning spectra of two mid-infrared pump frequencies, ω_1 and ω_2, in the double-Littrow external cavity system; (b) L-I-V curves of the device at 3.21 THz with one mid-infrared pump ω_1 at 955 cm^{-1} and the other mid-infrared pump ω_2 at 1062 cm^{-1}; (c) 2D spectra scan of THz peak power as a function of ω_1 and ω_2; (d) 2D spectra of mid-IR-to-THz conversion efficiency as a function of ω_1 and ω_2.

resulted in a limited THz tuning range less than 3.8 THz. Figure 6.6(c) and (d) show the THz peak power scan and mid-IR-to-THz conversion efficiency in 2D graphs as a function of frequency ω_1 and ω_2. As we expected, the experimental results of the conversion efficiency were not very high, at 3 to 3.5 THz, although at 2 THz, the conversion efficiency largely was the same as that of the device with a bound-to-continuum active region design.

6.5 THz DFG-QCL based on a long-wavelength bound-to-continuum design

The previous three-phonon active region design does not increase THz performance successfully, even in the low THz frequency range of 1~3 THz. This is most likely because of the effect of the OR process, which increases DFG nonlinearity below 2 THz, but decreases it above 2 THz. A promising method to improve THz performance in the 1~3 THz range overall is to maintain a large DR term at 3 THz by increasing the dipole moments, ez_{ij}, involved in the three-level system, while at the same time increasing the OR term by increasing the difference between the electron centroids in the upper and lower laser states.

Thus, the idea was not to reduce the separation between the two lower states |2> and |3>, but to keep the energy separation at approximately 3~3.6 THz (13~16 meV) between states |2> and |3> while reducing the energy separation between state |1> and state |2>. In this way, the dipole moments ez_{12} and ez_{13} are enlarged, DR terms are increased, and OR terms can be increased by increasing well width. The reduction in the energy separation between state |1> and state |2> forces the device to work in the longer mid-infrared wavelength range, and high-performance room-temperature mid-IR QCLs have been demonstrated recently at wavelengths as long as 14-15 μm [75-81]. We optimized a state-of-the-art, bound-to-continuum active region design that works at 14-16 μm [75,76] for DFG-THz generation, with 80 meV energy separation between state |1> and state|2>. Figure 6.7(a) shows the band structure of this design. The magnitude of $\chi^{(2)}$ included DR terms only, OR terms only, and both DR and OR terms, as Figure 6.7(b) shows. In this design, both the DR and OR terms increased, and the DFG nonlinearity at 1~3 THz increased overall by more than two times compared to that of the bound-to-continuum active region design at around 10 μm in Ref. [24,26].

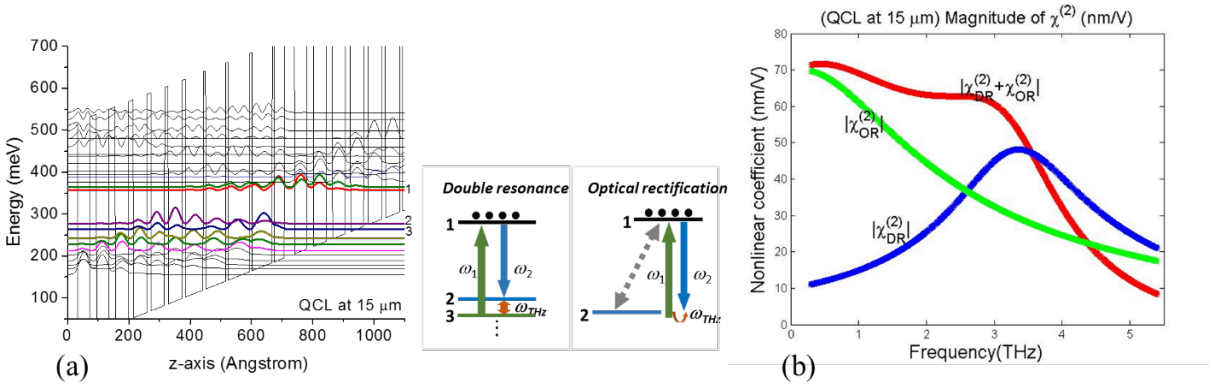

Figure 6.7: (a) One period of conduction band structure of bound-to-continuum active region design at 15 μm. The layer sequence begins with the injection barrier, which is **33**/33/**7**/66/**7**/71/**8**/65/**8**/58/**10**/46/**12**/44/**14**/44/**17**/42/**20**/41/**22**/40. The layer thicknesses are in angstroms, bold numbers indicate barriers, and underlined numbers indicate regions doped with Si to n= 2×10^{17} cm^{-3}. The middle two graphs show the transition diagram of double resonance and OR nonlinear processes; (b) Calculation of magnitude of $\chi^{(2)}$ including DR terms only, OR terms only, and both DR and OR terms, respectively, assuming Γ_{23} = 4 meV and Γ= 6 meV.

Although the nonlinearity $\chi^{(2)}$ increased as we shifted the device gain to the long-wavelength range, the waveguide loss in the long-wavelength, mid-infrared range also increased, and resulted in a higher threshold current density. We then decreased doping in the active region to reduce the waveguide loss for mid-infrared pumps. Reduced doping in the gain medium actually is better for the THz wave in the waveguide, as it reduced free carrier absorption loss for the THz wave as well, although the mid-infrared pump power also decreased. In addition, another interesting factor is the group index of the mid-infrared pumps for InGaAs/InAlAs/InP material. The group index for these pumps increased with wavelength, and resulted in a better index match with the SI-InP substrate and a shallower Cherenkov angle in the substrate for THz DFG-QCLs. This shallower Cherenkov angle essentially allowed a longer THz extraction length. Overall, $|\chi^{(2)}|^2$ increased by six times

and the effective propagation length of THz wave increased by 1.5 times compared to devices based on the bound-to-continuum gain medium design at 10 μm. Figure 6.8 shows simulations of the results for both the new and the reference design. We expected the final mid-IR-to-THz conversion efficiency overall to increase by an order of magnitude for 1~3 THz compared to the reference design.

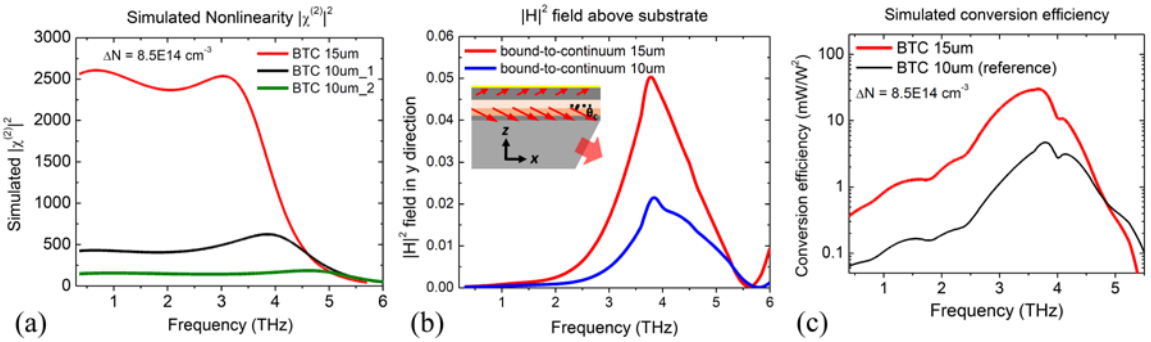

Figure 6.8: Simulation of device performance. (a) Comparison of the magnitude of $\chi^{(2)}$ between the new bound-to-continuum design at 15 μm and the reference bound-to-continuum design at 10 μm in Ref. [26]; (b) Comparison of THz field intensity on top of the substrate (assuming the unit value of $|\chi^{(2)}|$ for all THz frequencies) between the new design and the reference design in Ref. [26]. The THz field intensity is calculated based on the slab waveguide model discussed in section 6.3; (c) Comparison of the final conversion efficiency between the new design and the reference design in Ref. [26]. The population value N was deduced from the "gain = loss" condition and was approximately the same for both designs.

6.5.1 Device performance in external cavity set-up

To verify our simulation results, we fabricated devices into Fabry-Perot (FP) waveguide lasers, and tested them in the Littrow external cavity set-up described in Chapters 4 and 5 to obtain an experimental value of the conversion efficiency and determine the best pump frequency positions for THz generation. We fabricated devices

into 28-μm-wide and 1.9-mm-long laser ridges with the back facet coated with an AR coating. THz emission was collected through a 25^0 polished front substrate facet.

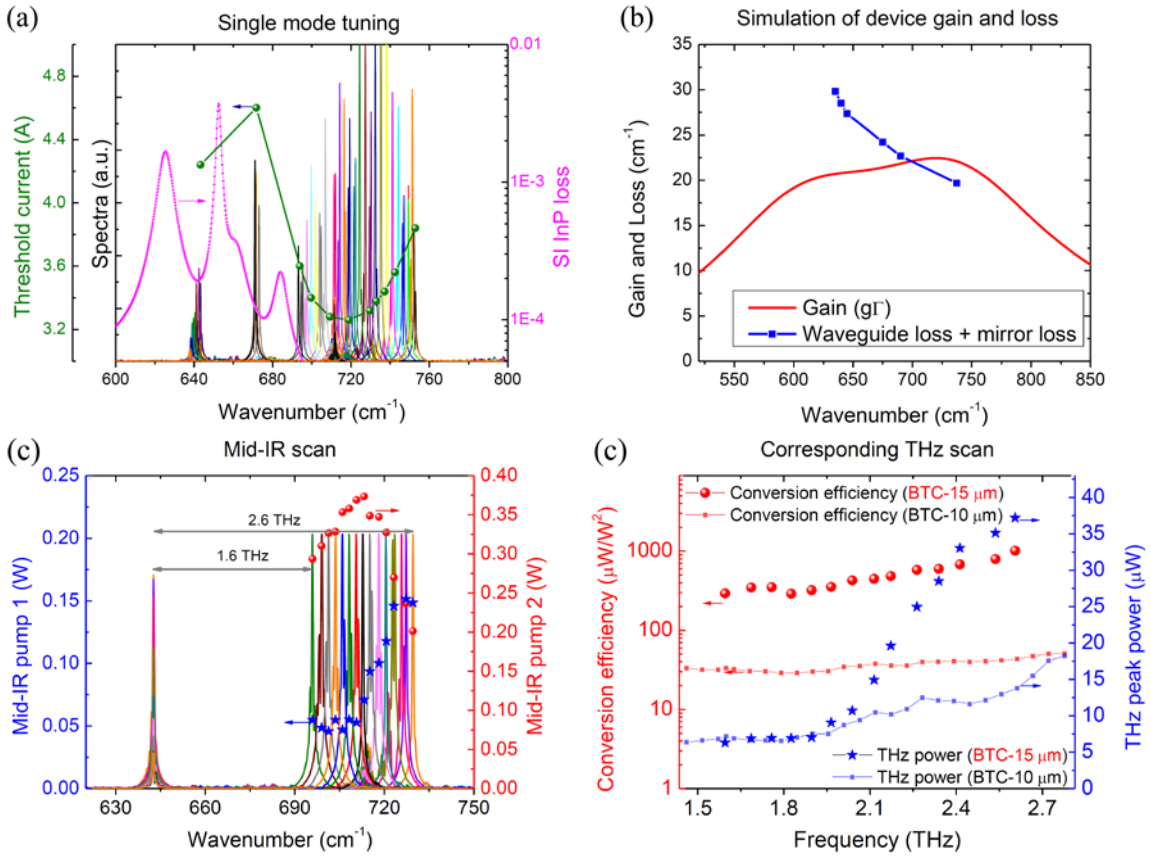

Figure 6.9: (a) Mid-IR tuning spectra of a Fabry-Perot device in the Littrow external-cavity system described in Chapter 4. Devices can be tuned from 640 to 752 cm^{-1}, with two large tuning gaps in the range. The pink line indicates InP loss as a function of wavenumber, data taken from Ref. [82]. The laser emission matches the dips in the InP absorption spectra. The green line shows the device threshold current as a function of wavelength; (b) Simulations of the gain and loss of the device for different wavelengths; (c) Mid-IR tuning spectra of a Fabry-Perot device in the double-Littrow external-cavity system described in Chapter 5. One external grating fixes one mid-IR pump ω_1 at 642 cm^{-1}, while the other grating tunes the other mid-IR pump ω_2 from 696 to 730 cm^{-1}. Blue and red dots represent the mid-IR pump power for ω_1 and ω_2 respectively; (d)

Corresponding THz tuning performance. Device with bound-to-continuum design at 15 μm (larger red dots) has a conversion efficiency one order of magnitude higher than the device with the design at 10 μm (smaller red dots).

Initially, an FP device was placed in a single-Littrow external cavity set-up (described in Chapter 4) for single wavelength tuning to check the tuning bandwidth of the device. As Figure 6.9(a) shows, the device can be tuned continuously from 640 to 752 cm^{-1}, except where there are two large tuning gaps in the tuning bandwidth. These two gaps between 644 to 671 cm^{-1} and 673 to 692 cm^{-1} are related most likely to the high carrier absorption of the InP cladding material in this wavelength range. The pink line in Figure 6.9(a) represents the absorption spectra of SI-InP [82], which indicated a good match between the absorption peak and the single-mode tuning gaps. Figure 6.9(a) also shows the threshold currents at different tuning positions. The threshold current at 640 cm^{-1} was approximately 1.3 times higher than that at around 730 cm^{-1}. This information is valuable in designing DFB gratings.

Based on this single-mode tuning performance, we were able to select mid-IR pump positions for DFG THz generation, and test the THz performance of the device using a double-Littrow external cavity system (described in Chapter 5). Because of the gaps in the tuning bandwidth, it is not easy to perform a 2D spectra analysis for this structure. Instead, we performed a 1D scan, using one external grating to feedback one mid-IR pump at 642 $cm^{-1,}$ and the other to tune the other mid-IR pump from 695 to 730 cm^{-1}, corresponding to a THz tuning range from 1.6-2.6 THz. Figure 6.9(c) shows the conversion efficiency of the device and the THz power output; these results are compared to the reference device in Ref. [26]. The conversion efficiency increased by one order of magnitude in the 1.6~2.6 THz frequency range, which matched our simulation expectation. However, the THz

output power of these devices increased only two times compared to the reference device at 2.6 THz. This is because the loss and the threshold current density in the longer mid-infrared wavelength range for InGaAs/InAlAs/InP-based QCL are higher, resulting in lower mid-IR pump power for these devices. It should be noted that longer wavelength QCLs based on other material systems can be designed to have relatively low threshold current densities, such as the InAs-based QCLs [80-81]; even room-temperature continuous-wave operation has been demonstrated at 15 μm for InAs based QCLs [80].

6.5.2 Monolithic device performance with dual-period DFB gratings

The results of Fabry-Perot device tuning in an external cavity system provide us with guidelines to fabricate monolithic devices [25,29,28]. We fabricated devices into laser ridges with dual-period DFB gratings etched on top of the ridge waveguide at a depth of approximately ~300 nm. Figure 6.10 shows a schematic of the device structure, in which DFB grating 1 supports lasing at ω_1, while DFB grating 2 supports lasing at ω_2; the back facets of the devices have an AR coating, while the substrates of the front facets are polished at 25^0. The DFB grating period, total length, and depth are critical design parameters in supporting dual-mid-infrared wavelength lasing. Careful control of these DFB grating design parameters is essential to balance the threshold current of the two mid-IR pumps, especially because this active region design includes two gaps in the gain bandwidth. The performances of three devices with THz emissions at 3.15, 3, and 1.5 THz are described in the following.

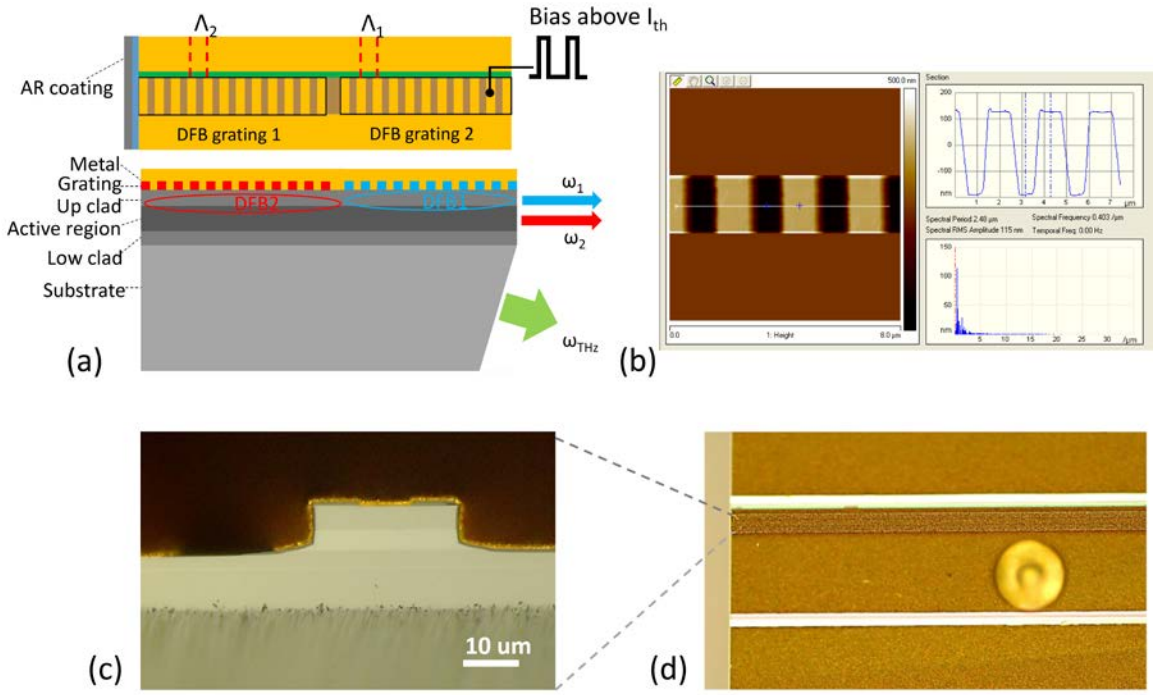

Figure 6.10: (a) Schematic of monolithic dual-period DFB grating device (top and side views); (b) AFM scan of DFB grating. The grating duty cycle is approximately 50%, while the grating etching depth is approximately 320 nm; (c) Optical image of the device facet after substrate polish; the manual polish stopped 8-μm from the current injection layer; (d) Top view of the device, where the yellow dot is the bonding ball.

For devices with THz emission at 3 THz, the mid-IR pump ω_1 must be selected at ~642 cm^{-1}, and the other mid-IR pump ω_2 selected at 742 cm^{-1}. To balance the loss of two DFB modes, the length of the DFB grating at pump ω_1 is designed to be longer than that at pump ω_2, with a ratio of 1.3:1. Figure 6.11(a) shows the L-I-V curves for mid-IR performance, and the inset of Figure 6.11(a) shows the device mid-IR lasing spectra. Figure 6.11(b) shows the THz L-I and spectra of the device, in which a maximum THz peak power of 85 μW was achieved at a current density of 11 kA/cm^2. Although the maximum mid-IR pump power of the device (~0.5 W) was much smaller than that of the reference device (1.3 W), the THz peak power still was 2.5 times higher at 3 THz. The mid-IR-to-THz

conversion efficiency is also plotted in Figure 6.11(b), as indicated by the green dots at discrete current density positions. Note that because of the lack of proper filters for the two mid-IR pumps, the pump power for ω_1 and ω_2 are derived based on power spectra at each bias point, respectively. THz peak power as a function of a two mid-IR pump power product is plotted in Figure 6.11(c), from which the mid-IR-to-THz conversion efficiency of the device can be derived; this was approximately 2.1 mW/W^2, which is approximately seven times higher than that of the reference design.

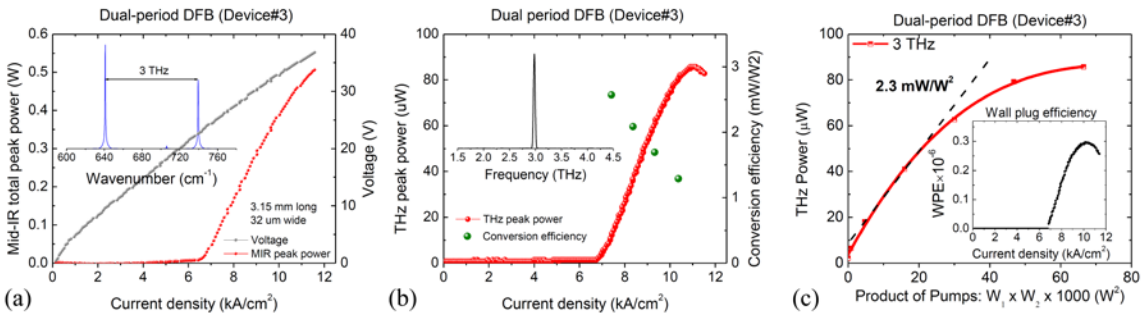

Figure 6.11: Dual-period DFB device at 3 THz. Device is 32-μm-wide, 3.15-mm-long in total (length of grating 1/length of grating 2 = 1.3). (a) Mid-infrared pump performance of the device: The red line shows the total power for both mid-IR pumps, and the gray line is the voltage-current curve of the device. The inset blue curve shows the spectra of the two mid-IR pumps; (b) The THz performance of the device: The red dots are the THz peak power as a function of current density, and green dots are the conversion efficiency at different applied biases. Inset is the THz spectra; (c) THz power as a function of the two mid-IR pump power product: The red dots are the experimental data; the red line is the fitted curve of the experimental data; Inset shows the wall plug efficiency of the device.

Figure 6.12 summarizes the performances of monolithic devices at 3.15 and 1.5 THz. Figure 6.12(b) and (c) illustrate the THz power and mid-IR power performance for the device at 1.5 THz and that at 3.15 THz, respectively. The mid-IR-to-THz conversion

efficiency of the two devices is given in Figure 6.12(a), in which THz power as a function of the two mid-IR pump power product is plotted. The device at 3.15 THz has a mid-IR-to-THz conversion efficiency of ~2.6 mW/W^2, while the device at 1.5 THz has a conversion efficiency of 0.22 mW/W^2.

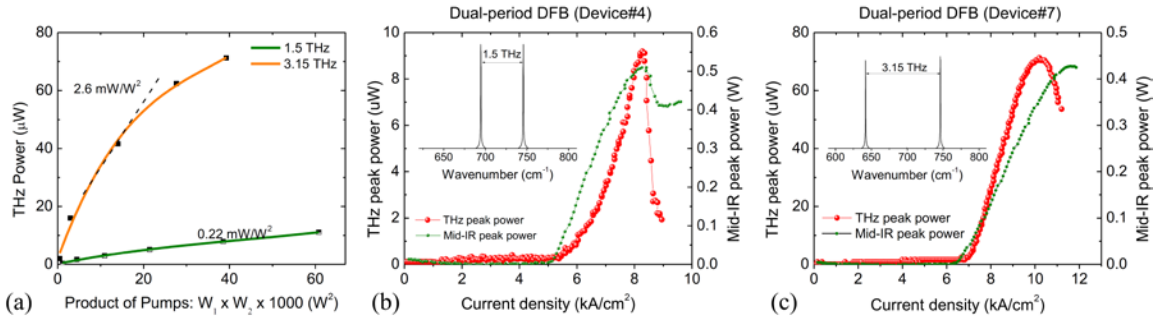

Figure 6.12: Monolithic dual-period DFB devices at 3.15 and 1.5 THz. (a) THz power as a function of pump power product for two devices. Black dots and squares are the experimental data, and the orange and green lines are the fitted curves for 3.15 and 1.5 THz, respectively; (b) THz (red dots) and mid-IR (green dots) L-I curves for the device at 1.5 THz; inset is the mid-IR spectra at 1.5 THz; (c) THz (red dots) and mid-IR (green dots) L-I curves for the device at 3.15 THz; inset is the mid-IR spectra at 3.15 THz.

6.6 Summary

In summary, this chapter provided a full description of the way in which to enhance the conversion efficiency and power output of THz DFG-QCLs, including improvement of the nonlinearity of $\chi^{(2)}$ and enhancement of the THz waveguide design. Using the wavelength selection technology developed in Chapters 4 and 5, we demonstrated a THz DFG-QCL in which the conversion efficiency was approximately one order of magnitude better, based on a bound-to-continuum active region design for 14~15 μm.

Chapter 7: Conclusion and outlook

In this thesis, I present the development of broadly tunable terahertz difference frequency generation-quantum cascade lasers (THz DFG-QCLs). Currently, THz DFG-QCLs are the only monolithic electrically-pumped semiconductor sources of 1-6 THz radiation that can operate at room temperature [30]. These devices can be produced in mass-quantities in existing telecom and quantum cascade laser foundries and have all the attractive features of semiconductor source technology, such as electrical pumping, compactness, scalability, and reliability. They are highly desired for the development of inexpensive and compact THz instrumentation for imaging, spectroscopy, heterodyne detection, and many other applications.

I demonstrated for the first time a record THz tuning range from 1.2 THz to 5.9 THz based on intra-cavity difference frequency generation between two mid-infrared pumps ω_1 and ω_2 generated in QCLs. By fixing one mid-infrared pump ω_1 with a DFB grating etched on top of the laser waveguide, and tuning the other mid-infrared pump ω_2 with an external diffraction grating outside of the laser waveguide, the difference frequency $\omega_1 - \omega_2$, corresponding to a THz frequency, could be tunable. After deposition of a good antireflection coating on laser facet, side-mode suppression ratio (SMSR) of mid-IR pumps could be ~25 dB while the SMSR for THz emission could be ~20 dB under pulsed operation condition.

We have resolved the beam steering problem of such widely tunable THz DFG-QCLs by replacing high dispersion semi-insulating InP with high resistivity silicon substrate, which is dispersionless and has a lower loss in 1 to 6 THz. Both incomplete substrate replacement method through substrate polishing and adhesive bonding and complete substrate replacement method through wet-etching of the substrate followed by adhesive bonding have been discussed.

Also, I have demonstrated a double Littrow external cavity THz DFG-QCL system, which allows separate and individual control of both mid-IR pump frequencies ω_1 and ω_2. Using a regular Fabry-Perot ridge waveguide, such a system allows performing a two-dimensional pump frequency study for the final THz output, which is useful for determining the best combination of two mid-IR pumps frequency for the best THz performance, and for measuring internal parameters critical for THz DFG-QCLs. We demonstrated that mid-IR-to-THz conversion efficiency can vary by two or more times even for the same THz frequency, depending on the selection of pump frequencies ω_1 and ω_2. We cooperate with Hamamatsu Photonics, the University of Wisconsin-Madison to perform initial characterization of different design of THz DFG-QCL using this system.

Finally, I have investigated different active region designs to improve the key performance characteristics (the mid-IR-to-THz conversion efficiency and THz power output) for THz DFG-QCLs using the wavelength selection technology developed above. A design based on bound-to-continuum active region design centered for 14~15 μm was studied. Mid-IR QCLs for long-wavelength lasing at 15 μm has much higher nonlinearity compared to mid-IR QCL with gain centered around 10 μm, moreover, group index for these long-wavelength QCLs is closer to the refractive index for ω_{THz} in SI InP substrate, resulting in shallower Cherenkov angle and higher THz DFG power. Overall, with novel active reign design and better waveguide design, these long-wavelength QCLs has demonstrated one order of magnitude higher conversion efficiency compared to QCLs with gain centered around 10 μm. Although with the sacrifice of threshold current density. The future direction may include investigating other material systems, like InAs-based QCLs [80-81], which could provide room temperature continuous-wave operation at 15 μm.

All the above broad THz spectral tunability and high conversion efficiency demonstrations have benefited to the introduction of the Cherenkov THz DFG-QCL devices in which THz radiation is emitted to a low loss substrate. Recently, the linewidth of free-running CW Cherenkov THz DFG-QCLs at 80 K was measured to be as narrow as 125 kHz (for 1 ms integration) [83], which makes these devices suitable for heterodyne detection, high-resolution spectroscopy, and gas sensing [84]. Our group is investigating THz DFG-QCL with surface grating out-couplers recently, in which high order (second or third) surface gratings for THz emission are integrated in the laser waveguide to facilitate THz output. These devices are processed into double-metal waveguides and are potential for high power, room temperature CW operation of THz DFG-QCLs.

Reference

1 F. C. D. Lucia, “Spectroscopy in the Terahertz Spectral Region. Sensing with Terahertz Radiation,” D. Mittleman. Berlin, Heidelberg, *Springer Berlin Heidelberg*: 39-115 (2003).

2 M. Tonouchi, “Cutting-edge terahertz technology,” *Nat Photon* **1**, 97-105 (2007).

3 J. W. Waters, *et al*., “The earth observing system microwave limb sounder (EOS MLS) on the aura satellite,” *IEEE Trans. Geosci. Remote Sensing* **44**, 1075–1092 (2006).

4 K. Kawase, Y. Ogawa, Y. Watanabe, and H. Inoue, “Non-destructive terahertz imaging of illicit drugs using spectral fingerprints.” *Opt. Express* **11**, 2549–2554 (2003).

5 S. Nashima, O. Morikawa, K. Takata, and M. Hangyo, “Temperature dependence of optical and electronic properties of moderately doped silicon at terahertz frequencies,” *J. Appl. Phys.* **90**, 837–842 (2001).

6 D. M. Mitttleman, J. Cunningham, M. C. Nuss and M. Geva, “Noncontact semiconductor wafer characterization with the Hall effect,” *Appl. Phys. Lett.* **71**, 16–18 (1997).

7 KoenigS, *et al.,* “Wireless sub-THz communication system with high data rate,” *Nat. Photon.*, **7**, 977-981 (2013).

8 J. Y. Suen, M.T. Fang, S.P. Denny, P. M. Lubin, “Modeling of Terabit Geostationary Terahertz Satellite Links From Globally Dry Locations,” *IEEE Trans. Terahertz Sci. Technol.*, **5**, 299-313 (2015).

9 T. W. Crowe, W. L. Bishop, D. W. Porterfield, J. L. Hesler, and R. M. Weikle, “Opening the Terahertz window with integrated diode circuits,” *IEEE Journal of Solid-State Circuits*, **40** 2104-2110 (2005).

10 E. R. Brown, “Advancements in Photomixing and Photoconductive Switching for THz Spectroscopy and Imaging,” *Terahertz Technology and Applications* **4**, 7938 (2011).

11 M. Scheller, J. M. Yarborough, J.V. Moloney, M. Fallhi, M. Koch, and S.W.Koch, “Room temperature continuous wave milliwatt terahertz source,” *Opt. Express* **18**, 17112 (2010).

12 S. Fathololoumi, E. Dupont, C.W.I. Chan, Z.R. Wasilewski, S.R. Laframboise, *et al.*, “Terahertz quantum cascade lasers operating up to ∼ 200 K with optimized oscillator strength and improved injection tunneling,” *Opt. Express* **20**, 3866-3876. (2012).

13 R. Kohler, A. Tredicucci, *et al.*, “Terahertz semiconductor-heterostructure laser,” *Nature* **417**, 156-159 (2002).

14 B. S. Williams, S. Kumar, Q. Hu and J. L. Reno, “High-power terahertz quantum-cascade lasers,” *Electron. Lett.* **42**, 89–91 (2006)

15 L. H. Li, L. Chen, J. X. Zhu, J. Freeeman, P. Dean, A. Valavanis, A.G. Davies and E. H. Linfield, “Terahertz quantum cascade lasers with >1 W output powers,” *Electron. Lett.* **50**, 309–10 (2014).

16 M. Rosch, G. Scalari, M. Beck and J. Faist, “Octave-spanning semiconductor laser,” *Nat. Photon.* **9**, 42–7 (2015).

17 B. S. Williams, *et al*. “Terahertz quantum-cascade lasers,” *Nat. Photonics* **1**, 517–25 (2007).

18 S. Kumar, “Recent progress in terahertz quantum cascade lasers,” *IEEE J. Sel. Top. Quantum Electron* **17**, 38–47 (2011).

19 M. S. Vitiello, G. Scalari, B. Williams and De Natale P, “Quantum cascade lasers: 20 years of challenges,” *Opt. Express* **23**, 5167–82 2015

20 Q. Qin, B. S. Williams, *et al*. “Tuning a terahertz wire laser,” *Nat. Photon.* **3**(12), 732-737 (2009).

21 M. A. Belkin, F. Capasso, A. Belyanin, D. L. Sivco, A. Y. Cho, D. C. Oakley, C. J. Vineis, and G. W. Turner, “Terahertz quantum-cascade-laser source based on intracavity difference-frequency generation,” *Nat. Photon.* **1** (5), 288-292 (2007).

22 M. A. Belkin, F. Capasso, F. Xie, A. Belyanin, M. Fischer, A. Wittmann, and J. Faist, “Room temperature terahertz quantum cascade laser source based on intracavity difference-frequency generation,” *Appl. Phys. Lett.* **92** (20), 201101 (2008).

23 K. Vijayraghavan, R. W. Adams, A. Vizbaras, M. Jang, C. Grasse, G. Boehm, M. C. Amann, and M. A. Belkin, “Terahertz sources based on Čerenkov difference-frequency generation in quantum cascade lasers,” *Appl. Phys. Lett.* **100** (25), 251104 (2012).

24 K. Vijayraghavan, **Y. Jiang**, M. Jang, A. Jiang, K. Choutagunta, A. Vizbaras, F. Demmerle, G. Boehm, M. C. Amann, and M. A. Belkin, “Broadly tunable terahertz generation in mid-infrared quantum cascade lasers,” *Nat. Commun.* **4** (2013).

25 S. Jung, A. Jiang, **Y. Jiang**, K. Vijayraghavan, X. Wang, M. Troccoli, and M. A. Belkin, “Broadly tunable monolithic room-temperature terahertz quantum cascade laser sources,” *Nat. Commun.* **5** (2014).

26 **Y. Jiang**, K. Vijayraghavan, S. Jung, F. Demmerle, G. Boehm, M. C. Amann, and M. A. Belkin, “External cavity terahertz quantum cascade laser sources based on intracavity frequency mixing with 1.2–5.9 THz tuning range,” *J. Opt.* **16** (9), 094002 (2014).

27 S. Jung, **Y. Jiang**, K. Vijayraghavan, A. Jiang, F. Demmerle, G. Boehm, X. Wang, M. Troccoli, M. C. Amann, and M. A. Belkin, “Recent Progress in Widely Tunable Single-Mode Room Temperature Terahertz Quantum Cascade Laser Sources,” *IEEE J. Sel. Top. Quantum Electron.* **21** (6), 1-10 (2015).

28 Q. Y. Lu, S. Slivken, N. Bandyopadhyay, Y. Bai, & M. Razeghi, “Widely tunable room temperature semiconductor terahertz source,” *Appl. Phys. Lett.* **105**, 201102 (2014).

29 A. Jiang, S. Jung, **Y. Jiang**, K. Vijayraghavan, J. H. Kim, and M. A. Belkin, “Widely tunable terahertz source based on intra-cavity frequency mixing in quantum cascade laser arrays,” *Appl. Phys. Lett.* **106** (26), 261107 (2015).

30 M. A. Belkin and F. Capasso, “New frontiers in quantum cascade lasers: high performance room temperature terahertz sources,” *Phys. Scripta* **90** (11), 118002 (2015).

31 **Y. Jiang**, K. Vijayraghavan, S. Jung, A. Jiang, J. H. Kim, F. Demmerle, G. Boehm, M. C. Amann, and M. A. Belkin, “Spectroscopic Study of Terahertz Generation in Mid-Infrared Quantum Cascade Lasers,” *Sci. Rep.* **6**, 21169 (2016).

32 S. Jung, J. H. Kim, **Y. Jiang**, K. Vijayraghavan, and M. A. Belkin, “Terahertz difference-frequency quantum cascade laser sources on silicon,” *Optica* **4**(1), 38-43 (2017).

33 Q. Y. Lu, N. Bandyopadhyay, S. Slivken, Y. Bai, and M. Razeghi, “Continuous operation of a monolithic semiconductor terahertz source at room temperature,” *Appl. Phys. Lett.* **104**(22), 221105 (2014).

34 M. Razeghi, Q. Y. Lu, N. Bandyopadhyay, W. Zhou, D. Heydari, Y. Bai, and S. Slivken, “Quantum cascade lasers: from tool to product,” *Opt. Express* **23**(7), 8462-8475 (2015).

35 Q.Y. Lu, N. Bandyopadhyay, S. Slivken, Y. Bai and M. Razeghi, “Widely tuned room temperature terahertz quantum cascade laser sources based on difference-frequency generation,” *Appl. Phys. Lett.* **101**, 251121 (2012).

36 K. Fujita, M. Hitaka, A. Ito, T. Edamura, M. Yamanishi, S. Jung and M.A. Belkin, “Terahertz generation in mid-infrared quantum cascade lasers with a dual-upper-state active region,” *Appl. Phys. Lett.* **106**, 251104 (2015).

37 R. F. Kazarinov and R. A. Suris, “Possibility of the amplification of electromagnetic waves in a semiconductor with a superlattice,” *Sov. Phys. Semicond.* **5**, 707 (1971).

38 J. Faist, F. Capasso, D. L. Sivco, C. Sirtori, A. L. Hutchinson, and A. Y. Cho, "Quantum Cascade Laser," *Science* **264** (5158), 553-556 (1994).

39 Y. Yao, A. J. Hoffman, and C. F. Gmachl, "Mid-infrared quantum cascade lasers," *Nat. Photon.* **6** (7), 432-439 (2012).

40 J. Faist, *Quantum Cascade Lasers* (Oxford: Oxford University Press, 2013).

41 R. F. Curl, F. Capasso, C. Gmachl, A. A. Kosterev, B. McManus, R. Lewicki, M. Pusharsky, G. Wysocki and F. K. Tittel, “Quantum cascade lasers in chemical physics,” *Chem. Phys. Lett.* **487,** 1-18 (2010).

42 F. Capasso, *et al.*, "Quantum cascade lasers: ultrahigh-speed operation, optical wireless communication, narrow linewidth, and far-infrared emission," *IEEE J. Quant. Electron.*, **38,** 511-532 (2002).

43 R. Paiella, *et al.*, "Generation and detection of high-speed pulses of mid-infrared radiation with intersubband semiconductor lasers and detectors," *IEEE Photonics Technol. Lett.*, **12**, 780-782 (2000).

44 F. Capasso, C. Sirtori, and A. Y. Cho, "Coupled quantum well semiconductors with giant electric field tunable nonlinear optical properties in the infrared," *IEEE J. Quantum Electron.* **30** (5), 1313-1326 (1994).

45 Friedli, P. *et al.*, "Four-wave mixing in a quantum cascade laser amplifier," *Appl. Phys. Lett.* **102**, 222104 (2013).

46 C. Sirtori, F. Capasso, J. Faist, L. N. Pfeiffer, and K. W. West, "Far-infrared generation by doubly resonant difference frequency mixing in a coupled quantum well two-dimensional electron gas system," *Appl. Phys. Lett.* **65** (4), 445-447 (1994).

47 H. Kogelnik and C. V. Shank, "Coupled-Wave Theory of Distributed Feedback Lasers," *J. Appl. Phys.* **43** (5), 2327-2335 (1972).

48 M. Carras, and A. De Rossi "Photonic modes of metallodielectric periodic waveguides in the midinfrared spectral range," *Phys. Rev. B* **74** (23), 235120 (2006).

49 M. Carras, M. Garcia, *et al.*, "Top grating index-coupled distributed feedback quantum cascade lasers," *Appl. Phys. Lett.* **93** (1), 011109 (2008).

50 B. G. Lee, M. A. Belkin, R. Audet, J. MacArthur, L. Diehl, C. Pflügl, F. Capasso, D. C. Oakley, D. Chapman, A. Napoleone, D. Bour, S. Corzine, G. Höfler, and J. Faist, "Widely tunable single-mode quantum cascade laser source for mid-infrared spectroscopy," *Appl. Phys. Lett.* **91** (23), 231101 (2007).

51 Q. Y. Lu, Y. Bai, N. Bandyopadhyay, S. Slivken, and M. Razeghi, "2.4 W room temperature continuous wave operation of distributed feedback quantum cascade lasers," *Appl. Phys. Lett.* **98** (18), 181106 (2011).

52 R. Maulini, A. Mohan, M. Giovannini, J. Faist, and E. Gini, "External cavity quantum-cascade laser tunable from 8.2 to 10.4μm using a gain element with a heterogeneous cascade," *Appl. Phys. Lett.* **88** (20), 201113 (2006).

53 G. Wysocki, R. F. Curl, *et al.*, "Widely tunable mode-hop free external cavity quantum cascade laser for high resolution spectroscopic applications," *Appl. Phys. B* **81**(6), 769-777 (2005).

54 Hugi, R. Terazzi, Y. Bonetti, A. Wittmann, M. Fischer, M. Beck, J. Faist, and E. Gini, "External cavity quantum cascade laser tunable from 7.6 to 11.4 μm," *Appl. Phys. Lett.* **95** (6), 061103 (2009).

55 R. Maulini, I. Dunayevskiy, A. Lyakh, A. Tsekoun, C. K. N. Patel, L. Diehl, C. Pflugl, and F. Capasso, "Widely tunable high-power external cavity quantum cascade laser operating in continuous-wave at room temperature," *Electron. Lett.* **45** (2), 107-108 (2009).

56 M. Chi, O. B. Jensen, and P. M. Petersen, "High-power dual-wavelength external-cavity diode laser based on tapered amplifier with tunable terahertz frequency difference," *Opt. Lett.* **36** (14), 2626-2628 (2011).

57 Blaser, S., D. A. Yarekha, *et al.*, "Room-temperature, continuous-wave, single-mode quantum-cascade lasers at $\lambda \simeq 5.4\mu m$," *Appl. Phys. Lett.* **86**(4), 041109 (2005).

58 Faist, J., M. Beck, *et al.*, "Quantum-cascade lasers based on a bound-to-continuum transition," *Appl. Phys. Lett.* **78**(2), 147-149 (2001).

59 Yao, Y., X. Wang, *et al.*, "High performance 'continuum-to-continuum' quantum cascade lasers with a broad gain bandwidth of over 400 cm^{-1}," *Appl. Phys. Lett.* **97**(8), 081115 (2010).

60 Fujita, K., T. Edamura, *et al.*, "High-performance, homogeneous broad-gain quantum cascade lasers based on dual-upper-state design," *Appl. Phys. Lett.* **96**(24), 241107 (2010).

61 R. Maulini, PhD thesis (University of Neuchâtel, 2006).

62 Gordon, C. Y. Wang, L. Diehl, F. X. Kärtner, A. Belyanin, *et al*., "Multimode regimes in quantum cascade lasers: From coherent instabilities to spatial hole burning," *Phy. Rev. A* **77** (5), 053804 (2008).

63 R. W. Boyd, *Nonlinear Optics* (Academic Press, New York, 2003).

64 V. Berger and C. Sirtori, "Nonlinear phase matching in THz semiconductor waveguides," *Semicond. Sci, Technol.* **19** (8), 964 (2004).

65 C. Gmachl, A. Soibel, R. Colombelli, D. L. Sivco, F. Capasso, and A. Y. Cho, "Minimal group refractive index dispersion and gain evolution in ultra-broad-band quantum cascade lasers," *IEEE Photonics Technol. Lett.* **14** (12), 1671-1673 (2002).

66 Hugi, G. Villares, S. Blaser, H. C. Liu, and J. Faist, "Mid-infrared frequency comb based on a quantum cascade laser," *Nature* **492** (7428), 229-233 (2012).

67 E. D. Palik, *Handbook of Optical Constants of Solids* (Academic, New York, 1998).

68 G. H. Duan, *et al.*, "Hybrid III--V on Silicon Lasers for Photonic Integrated Circuits on Silicon," *IEEE J. Sel. Top. Quantum Electron.* **20**, 158-170 (2014).

69 J. Christian, M. Alpar, L. Paolo, and A. Markus-Christian, "Monte Carlo study of terahertz difference frequency generation in quantum cascade lasers," *Opt. Express* **21**, 6180-6185 (2013).

70 J. Christian, O. Hesham, and L. Paolo, "Monte Carlo analysis of the terahertz difference frequency generation susceptibility in quantum cascade laser structures," *Opt. Express* **23**, 1670-1678 (2015).

71 N. Hashizume, *et al.*, "Theoretical analysis of Cerenkov-type optical second-harmonic generation in slab waveguides," *IEEE J. Quant. Electron.* **28**, 1798 (1992).

72 Dupont, E., Z. R. Wasilewski, *et al.*, "Terahertz Emission in Asymmetric Quantum Wells by Frequency Mixing of Midinfrared Waves," *IEEE J. Quant. Electron.* **42**(11), 1157-1174 (2006).

73 B. A. Burnett and B. S. Williams, "Origins of terahertz difference frequency susceptibility in midinfrared quantum cascade lasers," *Phys. Rev. Appl.* **5**, 034013 (2016).

74 Wang, Q. J., C. Pflügl, *et al.*, "High performance QCLs based on three-phonon-resonance design," *Appl. Phys. Lett.* **94** (1), 011103 (2009).

75 Faist, K., D. Hofstetter, *et al.*, "Bound-to-continuum and two-phonon resonance, quantum-cascade lasers for high duty cycle, high-temperature operation," *IEEE J. Quant. Electron.* **38**(6), 533-546 (2002).

76 Rochat, M., D. Hofstetter, *et al.*, "Long-wavelength (λ≈16 μm), room-temperature, single-frequency quantum-cascade lasers based on a bound-to-continuum transition," *Appl. Phys. Lett.* **79**(26), 4271-4273 (2001).

77 Fuchs, P., J. Semmel, *et al.*, "Distributed feedback quantum cascade lasers at 13.8 μm on indium phosphide," *Appl. Phys. Lett.* **98**(21), 211118 (2011).

78 X. Huang, W. O. Charles, and C. Gmachl, "Temperature-insensitive long-wavelength (λ≈14 μm) quantum cascade lasers with low threshold", *Opt. Express* **19,** 8297-8302 (2011).

79 K. Fujita, M. Yamanishi, T. Edamura, A. Sugiyama, and S. Furuta, "Extremely high T0-values (~ 450 K) of long-wavelength (~ 15 μm), low-threshold-current-density quantum-cascade lasers based on the indirect pump scheme," *Appl. Phys. Lett.* **97**, 201109 (2010).

80 A. N. Baranov, *et al.*, "Room temperature continuous wave operation of InAs-based quantum cascade lasers at 15 μm," *Opt. Express* **24**, 18799-18806 (2016)

81 Chastanet, D., A. Bousseksou, *et al.*, "High temperature, single mode, long infrared (λ = 17.8 μm) InAs-based quantum cascade lasers," *Appl. Phys. Lett.* **105**(11), 111118 (2014).

82 L. N. Alyabyeva1, E. S. Zhukova1, M.A. Belkin, B. P. Gorshunov, "Dielectric properties of semi-insulating Fe-doped InP in the terahertz spectral region," under review (2016).

83 L. Consolino, S. Jung, S. Bartalini, K. Fujita, M. Hitaka, A. Ito, P. De Natale, M.A. Belkin, and M. Vitiello, “Linewidth and tuning characterization of terahertz quantum cascade lasers sources based on intra-cavity difference-frequency generation,” under review (2016).

84 A Sampaolo, P Patimisco, M Giglio, M.S. Vitiello, H.E. Beere, D.A. Ritchie, G. Scamarcio , F.K. Tittel, and V. Spagnolo, “Improved tuning fork for terahertz quartz-enhanced photoacoustic spectroscopy,” *Sensors* **16**, 439 (2016).